

Structural and Electrochemical Properties of Oxo-Functionalized Graphene

Inaugural-Dissertation

to obtain the academic degree

Doctor rerum naturalium (Dr. rer. nat.)

submitted to the Department of Biology, Chemistry, Pharmacy

of Freie Universität Berlin

by

Yiqing Wang

January 2022

The work presented here was conducted from 04/2019 until 01/2022 at the Department of Biology, Chemistry, Pharmacy of the Freie Universität Berlin under the supervision of Prof. Dr. Siegfried Eigler.

1st Reviewer: Prof. Dr. Siegfried Eigler (Freie Universität Berlin)

2nd Reviewer: Prof. Dr. Kannan Balasubramanian (Humboldt-Universität zu Berlin)

Date of defense: 31.03.2022

Acknowledgments

Here, I want to thank my supervisor Prof. Dr. Siegfried Eigler for allowing me to do specific work in his group. He provided me with a very open platform and also gave me much freedom. He also gave me very efficient guidance and assistance in the writing and revision of manuscripts.

Thanks to the colleagues in AG Eigler for their great help in work and life. Getting along with them and learning about different ways of thinking have greatly benefited me. Thanks to our collaborators Prof. Dr. Andrey Turchanin at Friedrich-Schiller-Universität Jena and Dr. Patryk Kusch in Institute of Physics at Freie Universität Berlin. Thanks to Prof. Dr. Kirill Bolotin in the Institute of Physics at the Free University of Berlin. The preparation of heterojunction and AFM tests was in his cleanroom. Thanks to Prof. Dr. Stephanie Reich in the Institute of Physics at the Free University of Berlin for using Raman in her group.

I want to thank the China Scholarship Council for funding me.

Finally, I would like to thank my family for their endless care, understanding, and support. I haven't been home for a long time because of the pandemic. I'm sorry I missed a lot of things. I am looking forward to an early reunion.

Statement of the author

I declare on the affidavit that I have written the dissertation independently and have used no sources other than those I have indicated and that there are no facts that make me unworthy of the conduct of a doctoral degree under the provisions of the law governing academic degrees. Further, I declare my consent that the electronic version of my dissertation, while maintaining my copyrights and data protection, may be subjected to a separate review regarding the independent preparation of the dissertation. I have not submitted the dissertation anywhere else to obtain an academic degree and have not already passed this or a similar doctoral exam without success.

Berlin, 10.01.2022

Table of contents

1. Summary	1
2. Zusammenfassung	4
3. Introduction	7
3.1 History of graphene oxide	7
3.2 Synthetic methods of graphene oxide.....	9
3.3 Structure of graphene oxide	11
3.4 Electrochemical properties of graphene oxide.....	13
3.5 Photoluminescence of MoS ₂	15
4. Methods.....	17
4.1 Langmuir-Blodgett technique.....	17
4.2 Raman spectroscopy	18
4.3 X-ray photoelectron spectroscopy	20
4.4 Atomic force microscopy	22
4.5 Transfer technique of 2D materials	22
4.6 Cyclic voltammetry	24
4.7 Rotating ring-disk electrode test	27
5. Main contributions.....	28
5.1 Synthesis of wet-chemically prepared porous-graphene single layers (Contain oxygen-containing groups) on Si/SiO ₂ substrate increasing the photoluminescence of MoS ₂ in heterostructures.	28
5.2 Regiochemically oxo-functionalized graphene, guided by defect sites, as catalyst for oxygen reduction to hydrogen peroxide.	52
5.3 Influence of the coffee-ring effect and size of flakes of GO films on the electrochemical reduction.	65
6. Minor contributions.....	73
6.1 Wet-chemical synthesis of solution-processible porous graphene via defect-driven etching.	73
Reference	92
List of publications.....	99
List of Abbreviations.....	100

1. Summary

In 1855, Brodie described the formation of graphite oxide for the first time. Graphene oxide (GO) has experienced more than 150 years of development, and a variety of preparation methods have emerged. In this thesis, oxo-functionalized graphene (oxoG) was used as a model to investigate the structural and electrochemical properties of oxoG and related materials. OxoG is a derivative of GO with a defined density of defects and well-controlled surface chemistry. There are three main works in this thesis, as shown in Figure 1.

Overall, the controllable structure of oxoG is further explored in the thesis. In the first part, the controllable fabrication of the pores at the single-layer level is carried out. The pores and the electron-withdrawing groups at the rims of pores enhance the photoluminescence of MoS₂. The second part is about vacancy defects (small pores) and their oxygen functionalization. In addition, in terms of electrochemistry, the second part discusses that the defects of electrochemical oxygen functionalization are active sites for oxygen reduction catalysts to produce H₂O₂. The third part is about flake size of oxoG, morphology of oxoG film, and loading effect on the electrochemical reduction of oxoG film.

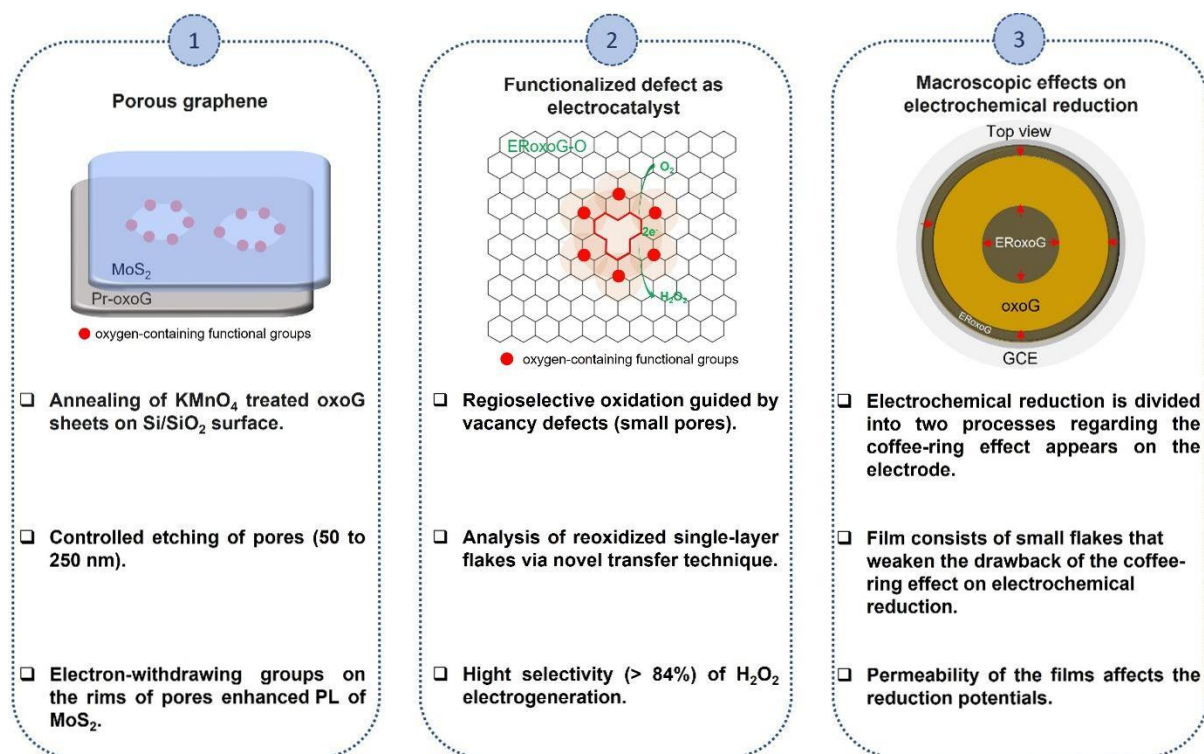


Figure 1. Summary of the thesis. The first two parts mainly focus on the pore preparation in oxoG (large pores, and tiny pores similar to vacancy defects) and the properties of oxygen functional groups. The third part focuses on the influence of sheet size and morphology on electrochemical reduction.

1) Etching pores in single layers of oxoG. Porous graphene with electron-withdrawing groups at the rims of pores to enhance the photoluminescence of MoS₂.

GO of lower quality can be produced in large quantities, but the existing lattice defects caused during synthesis hinder the controlled growth of pores. However, uniform pores are required in applications such as membranes, energy storage, or nanoelectronic applications. Here, we grew pores with controllable diameters in single layers of oxoG, which bear a lower intrinsic density of lattice defects than other comparable GOs directly on Si/SiO₂ wafers by heating potassium permanganate treated films of oxoG at 400 °C. The size of the pores increases with the extension of the etching time, and pore diameters in the range of 50-250 nm are obtained. The sheets remain stable on the micrometer scale and do not fold. The X-ray photoelectron spectroscopy analysis shows that the edges of the pores are functionalized with oxygen functional groups. Heterostructures of porous graphene with intrinsically n-doped MoS₂ show a 10-fold increase in photoluminescence.

As a two-dimensional material, pore-graphene with functional groups at the rims of pores can be modified at the edge of the pore, so it has great potential for applications in the field of sensing.

2) Regioselective oxo-functionalized graphene, guided by defect sites (small pores) as a catalyst for hydrogen peroxide (H₂O₂) production.

In the first work, oxygen-containing groups at the rims of the pores with electron-withdrawing properties were identified. To develop electronic devices and energy conversion materials, a better understanding of oxygen-functionalized graphene's structural and electrochemical properties is necessary. We use oxoG as the initial material. Electrochemical methods are used to reduce and subsequently reoxidize oxoG. It is found that vacancy defects herein play a guiding role in introducing oxygen-containing groups close to these defect sites. Statistical Raman spectroscopy is applied to investigate single layers. The selectivity (> 84%) of the sample on H₂O₂ generation increases significantly by increasing the number of oxygen functional groups close to vacancy defects. Moreover, reliable Raman data requires monolayers, a new method for the transfer of single-layer materials from films using polydimethylsiloxane (PDMS) is developed. This work provides ideas for the design of active sites in oxygen-doped carbon-based electrocatalysts. More accurate and comparable information can be obtained by single layers exfoliated from the bulk material for Raman analysis.

In this work, we use two types of GOs, oxoG with a larger flake size and oxoG* with a smaller flake size. We find that the electrochemical reduction of the film made of small flakes (oxoG*) can obtain reduced oxoG* in significantly higher quality than the typically used chemical reduction by hot vapour of hydrogen iodine. In contrast, the film composed of the large flakes

(oxoG) obtains reduced oxoG in lower quality than the chemical reduction. The size of the flake may have a vital effect on the reduction of GO. Therefore, the next discussion is about the macroscopic effects of the electrochemical of the oxoG film.

3) Electrochemical reduction of oxoG films composed of different flake sizes.

Since the discovery of graphene, the electrochemical reduction of GO to obtain graphene-like compounds has been widely reported. So far, it has been not clear how the loading, the size of the GO flakes, or the coffee ring effect that occurs during the drying process would affect the reduction process. It is revealed that the effective transfer of protons and electrons in the electrochemical reduction of GO is decisive.

Here, we deposit oxoG from an aqueous solution on a glassy carbon electrode. Under low loading amount, the electrochemical reduction process is affected by the coffee ring effect and, at the same time, by the size of the flakes. The most likely explanation for this phenomenon is that the contact of the electrolyte (pH=7.4) promotes the reduction of oxoG, thereby effectively transferring protons. The electrolyte easily penetrates the oxoG membrane with flakes of small size or lower loading amount. Furthermore, the electrolyte permeates the layers, which causes the reduction peak to shift to a more negative potential, improves the reduction efficiency, and eliminates the drawbacks of the coffee ring effect. The reduction process of oxoG with different loadings is monitored by using a camera. This work has a significant effect on the electrochemical functionalization of two-dimensional materials and the design of two-dimensional composite materials as efficient electrocatalysts.

2. Zusammenfassung

Im Jahr 1855 beschrieb Brodie zum ersten Mal die Bildung von Graphitoxid. Graphenoxid (GO) hat mehr als 150 Jahre der Entwicklungen erlebt, und eine Vielzahl von Darstellungsmethoden entstanden. In dieser Arbeit wurde oxo-funktionalisiertes Graphen (oxoG) als Modell verwendet, um die strukturellen und elektrochemischen Eigenschaften von oxoG und verwandten Materialien zu untersuchen. OxoG ist ein Derivat von GO mit einer definierten Dichte von Defekten und einer gut kontrollierten Oberflächenchemie. Es gibt drei Hauptbeiträge in dieser Arbeit, wie in Abbildung 1 dargestellt.

Insgesamt wird in dieser Arbeit die kontrollierbare Struktur von oxoG weiter erforscht. Im ersten Teil wird die kontrollierbare Herstellung der Poren auf Einzelschichtebene durchgeführt. Die Poren und die elektronenanziehenden Gruppen an den Rändern der Poren verstärken die Photolumineszenz von MoS₂. Der zweite Teil befasst sich mit Leerstandsdefekten (kleine Poren) und deren Sauerstofffunktionalisierung. In Bezug auf die Elektrochemie wird im zweiten Teil erörtert, dass die Defekte der elektrochemischen Sauerstofffunktionalisierung aktive Stellen für Sauerstoffreduktionskatalysatoren zur Erzeugung von H₂O₂ sind. Der dritte Teil befasst sich mit der Flockengröße von oxoG, der Morphologie des oxoG-Films und dem Einfluss der Beladung auf die elektrochemische Reduktion des oxoG-Films.

1) Ätzen von Poren in Monolagen von OxoG. Poröses-Graphen mit elektronenziehenden Gruppen an den Porenrändern zur Verbesserung der Photolumineszenz von MoS₂.

GO von niedriger Qualität kann in großen Mengen hergestellt werden, aber die bei der Synthese eingeführten Gitterdefekte behindern das kontrollierte Wachstum der Poren. Für Anwendungen wie Membranen, Energiespeicherung oder nanoelektronische Anwendungen sind jedoch einheitliche Poren erforderlich. Durch Erhitzen von OxoG auf 400 °C, das zuvor mit Kaliumpermanganat behandelt wurde, werden Poren mit kontrollierbaren Durchmessern in einzelne Schichten aus OxoG auf Si/SiO₂-Wafers eingebracht. Hierbei ausschlaggebend ist die geringere Defektdichte im Kohlenstoffgitter von oxoG im Vergleich zu normalem GO. Die Größe der Poren nimmt mit zunehmender Ätzdauer zu, und man erhält Porendurchmesser im Bereich von 50-250 nm. Die Flocken bleiben im Mikrometermaßstab stabil und falten sich nicht. Die Analyse der Röntgenphotoelektronenspektroskopie zeigt, dass die Ränder der Poren mit funktionellen Sauerstoffgruppen funktionalisiert sind. Heterostrukturen aus porösem Graphen mit intrinsisch n-dotiertem MoS₂ zeigen eine 10-fache Steigerung der Photolumineszenz.

Als zweidimensionales Material kann poröses Graphen mit funktionellen Gruppen an den Porenrändern modifiziert werden, so dass es ein großes Potenzial für Anwendungen im Bereich der Sensorik hat.

2) Regioselektives oxo-funktionalisiertes Graphen, an Defektstellen (kleine Poren) als Katalysator für die Wasserstoffperoxid-Produktion.

In der ersten Arbeit identifizierten wir funktionelle Gruppen an den Rändern von Poren mit elektronenziehenden Eigenschaften. Für die Entwicklung von elektronischen Bauteilen und Energieumwandlungsmaterial ist ein besseres Verständnis der strukturellen und elektrochemischen Eigenschaften von sauerstofffunktionalisiertem Graphen erforderlich. Wir verwenden oxoG als Ausgangsmaterial. Mit elektrochemischen Methoden wird oxoG reduziert und anschließend wieder reoxidiert. Es zeigt sich, dass Leerstellen im Kohlenstoffgitter eine ausschlaggebende Rolle bei der Einführung sauerstoffhaltiger Gruppen in der Nähe von solchen Defektstellen spielen. Die statistische Raman-Spektroskopie wird zur Untersuchung einzelner Schichten eingesetzt. Die Selektivität (> 84%) der hergestellten Probe zur H₂O₂-Erzeugung steigt signifikant, wenn die Anzahl der sauerstoffhaltigen funktionellen Gruppen in der Nähe von solchen Fehlstellen erhöht wird. Da für zuverlässige Raman-Daten Monoschichten erforderlich sind, wird eine neue Methode für den Transfer von Einzelschichtmaterialien aus Filmen mit Polydimethylsiloxan (PDMS) entwickelt. Diese Arbeit liefert Ideen für die Gestaltung von aktiven Stellen in sauerstoffdotierten Elektrokatalysatoren auf Kohlenstoffbasis. Genauere und vergleichbare Informationen können durch Raman-Analyse der einzelnen Schichten gewonnen werden, welche aus dem Grundmaterial herausgelöst werden.

In dieser Arbeit verwenden wir zwei Arten von GOs, oxoG mit größerer Flockengröße und oxoG* mit kleinerer Flockengröße. Wir stellen fest, dass die elektrochemische Reduktion des Films, der aus kleinen Flocken besteht (oxoG*), reduziertes oxoG* in höherer Qualität liefert als die typische chemische Reduktion mit heißem Dampf von Iodwasserstoff. Im Gegensatz dazu wird bei der Schicht aus großen Flocken (oxoG) reduziertes OxoG in geringerer Qualität als bei der chemischen Reduktion erhalten. Die Größe der Flocken kann einen entscheidenden Einfluss auf die Reduktion von GO haben. Daher werden im Folgenden die makroskopischen Auswirkungen der elektrochemischen Reduktion des oxoG-Films diskutiert.

3) Elektrochemische Reduktion von OxoG-Filmen, die aus verschiedenen Flockengrößen bestehen.

Seit der Entdeckung von Graphen wurde viel über die elektrochemische Reduktion von GO zur Gewinnung Graphen-basierter Verbindungen berichtet. Bisher war nicht klar, wie sich die Beladung, die Größe der GO-Flocken oder der Kaffeeing-Effekt, der während des

Trocknungsprozesses auftritt, auf den Reduktionsprozess auswirken würde. Es hat sich gezeigt, dass der effektive Transfer von Protonen und Elektronen bei der elektrochemischen Reduktion von GO entscheidend ist.

Hier haben wir eine wässrige oxoG-Lösung auf einer Glaskohlenstoffelektrode abgeschieden. Bei geringer Beladungsmenge wird der elektrochemische Reduktionsprozess durch den Kaffeeing-Effekt und gleichzeitig durch die Größe der Flocken beeinflusst. Die wahrscheinlichste Erklärung für dieses Phänomen ist, dass der Kontakt mit dem Elektrolyten (pH=7,4) die Reduktion von oxoG fördert und dadurch Protonen effektiv übertragen werden. Der Elektrolyt dringt leicht in die OxoG-Membran ein, wenn die Flocken eine geringe Größe oder eine niedrige Beladungsmenge aufweisen. Außerdem verfestigt der Elektrolyt die Schichten, wodurch sich der Reduktionspeak zu einem negativeren Potenzial verschiebt, die Reduktionsleistung verbessert und die Nachteile des Kaffeeing-Effekts beseitigt werden. Der Reduktionsprozess von oxoG mit unterschiedlichen Beladungen wird mit einer Kamera überwacht. Diese Arbeit hat einen bedeutenden Einfluss auf die elektrochemische Funktionalisierung von zweidimensionalen Materialien und das Design von zweidimensionalen Kompositmaterialien als effiziente Elektrokatalysatoren.

Insgesamt wird die kontrollierbare Struktur von oxoG in dieser Arbeit weiter erforscht. Im ersten Teil wird die kontrollierbare Herstellung der Poren auf Einzelschichtebene durchgeführt. Die Poren und die elektronenanziehenden Gruppen an den Rändern der Poren verbessern die Photolumineszenz von MoS₂. Im zweiten Teil geht es um Leerstellen (kleine Poren) und deren Sauerstofffunktionalisierung, und im dritten Teil um die kontrollierbare Schichtgröße. Was die Elektrochemie betrifft, so wird im zweiten Teil erörtert, dass die Defekte der elektrochemischen Sauerstofffunktionalisierung aktive Stellen für Sauerstoffreduktionskatalysatoren zur Erzeugung von H₂O₂ sind. Der dritte Teil befasst sich mit der Morphologie, der Größe der Flocken und der Auswirkung der Beladung auf die elektrochemische Reduktion des oxoG-Films.

3. Introduction

3.1 History of graphene oxide

André Geim and Konstantin Novoselov Isolated and conducted fundamental experiments with the two-dimensional material graphene in 2004 and won the 2010 Nobel Prize in Physics.^{1,2} Since then, graphene oxide (GO) – a highly oxygenated derivative of graphene - was seen as a promising precursor to obtain large bulk quantities of graphene-based materials in a short time, as upscaling of the wet-chemical synthesis via graphite oxidation, exfoliation and subsequent reduction can be done easily, while the so-called adhesive tape exfoliation of graphite leads only to some graphene flakes on solid substrates only.^{1,2} More details about GO will be outlined in the later section 3.3. Entering “graphene oxide” in Google Scholar results in about 952,000 relevant results in the span of 2004 to 2021.

But not only André Geim and Konstantin Novoselov achieve the highest honors for research on graphite or graphene, respectively, but also Akira Yoshino along with Stanley Whittingham and John Goodenough with their Noble Price in Chemistry in 2019. He used petroleum coke, a carbon material that can be intercalated by lithium ions, as the anode material and prepared lightweight, hardwearing and rechargeable batteries. The interesting point here is that the observed and investigated intercalation process is a crucial step also in graphene oxide formation.

180 years ago (Figure 2). As early as 1840, Schafhäütl described graphite intercalation compounds for the first time in a publication on iron-carbon steel. This earliest description did not get much attention from early researchers.³ Brodie described the formation of graphite oxide for the first time in a short article in 1855.⁴ Four years later, another preparation method, now known as "Brodie's method", came up and the newly obtained compound was described in detail.⁵ In 1865, Gottschalk confirmed Brodie's results and proposed the term "graphite acid".⁶ Staudenmaier discussed in detail the disadvantages of the existing preparation method in 1898 and tried to find a simpler and less dangerous method, which was named after him and is still used up to now. The details of the method will appear in the synthetic method (section 3.2).⁷ Charpy was the first who use permanganate as an oxidant to prepare graphite oxide in 1909.⁸ In 1919, Kohlschütter and Haenni believed that the close structural correlation between graphite and graphite oxide was a "topological" relationship. The above research mainly relies on classical chemical analysis and description of reactants.⁹

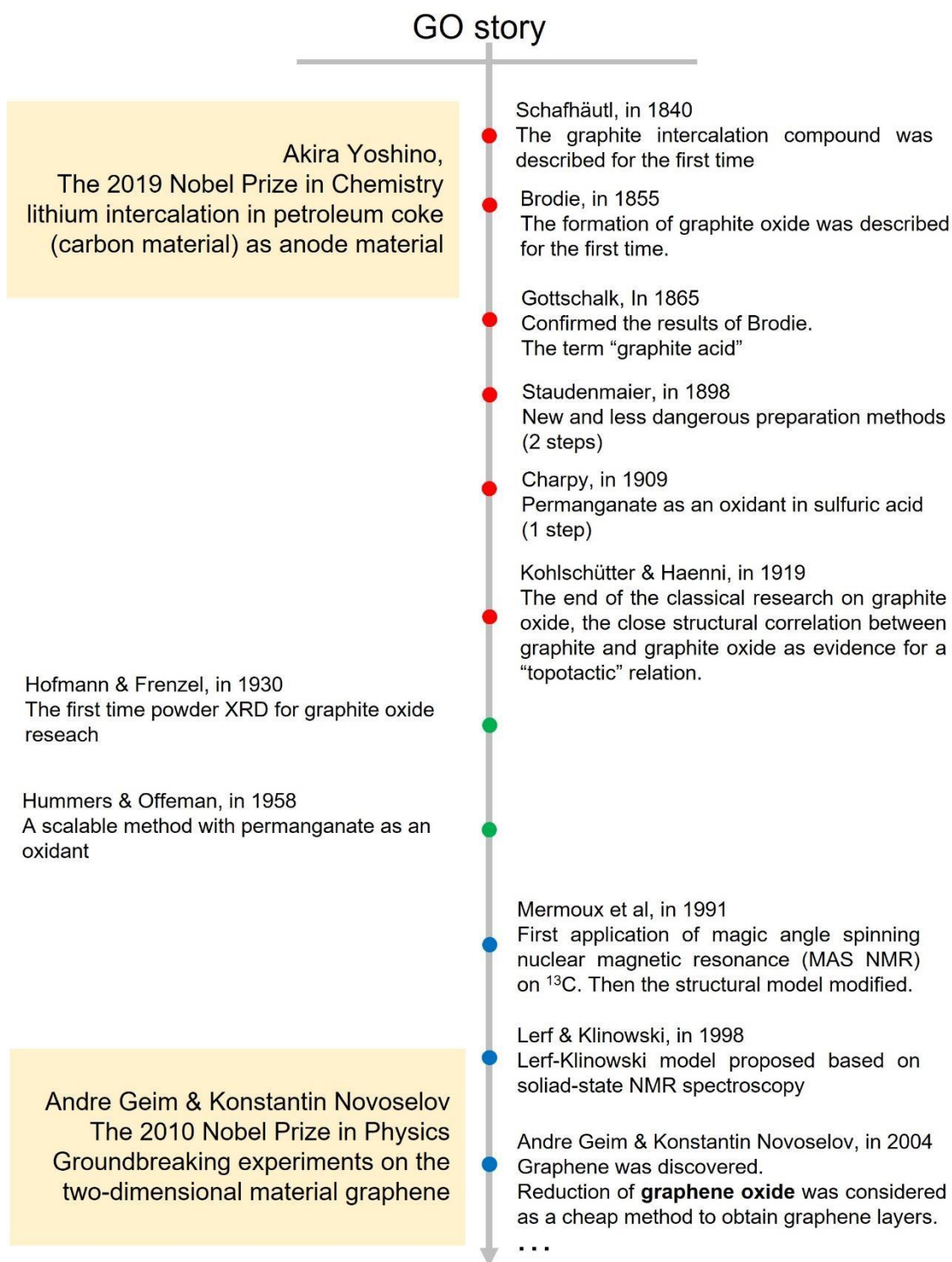


Figure 2. History of graphene oxide. The red, green, and blue dots represent three different periods.

The application of X-ray diffraction (XRD) to graphite oxide analysis has further promoted research into a new stage.¹⁰ In 1930, Hofmann and Frenzel used XRD to analyze graphite oxide for the first time.¹¹ Then, he and his co-workers gave the structure model of graphite

oxide (Epoxy groups on graphite oxide).¹² In 1958, Hummers and Offeman proposed a scalable method with permanganate as an oxidant in sulfuric acid.¹³ A new structural model was proposed by Scholz and Boehm in 1969 (All hydroxyl groups replace epoxy groups. The carbon plane is composed of regularly folded cyclohexane and connected quinolone).¹⁴ The research on the model has been modified many times along with the emergence of new analysis methods.

Mermoux et al. first applied high-resolution nuclear magnetic resonance (¹³C NMR) to analyze in 1991,^{15, 16} further promoted scientific researchers' understandings of graphite oxide (ether and hydroxyl groups connected to sp² carbon are in ethylenic bonds). Subsequently, the graphite oxide model went through a process of constant questioning and verification. In 1998, Lerf and Klinowski proposed a new model based on solid-state nuclear magnetism spectroscopy, in which hydroxyl and epoxy functional groups are distributed on the basal plane of graphene and carboxylic acid groups and hydroxyl functional groups are distributed on the edges.¹⁷ After the discovery of graphene, the physical and chemical properties of GO and reduced GO and the application of related materials have become very hot topics.^{18, 19} But from the perspective of graphite oxide or GO development, GO is a unique material different from graphene. There are still many issues for exploration for its structure, properties, and practical application in life. For example, enlargement of GO defects or repair of defects, controllable functionalization of oxygen functional groups, and structure-activity relationship of graphene oxide as a key material for catalysis, energy storage, membranes.

3.2 Synthetic methods of graphene oxide

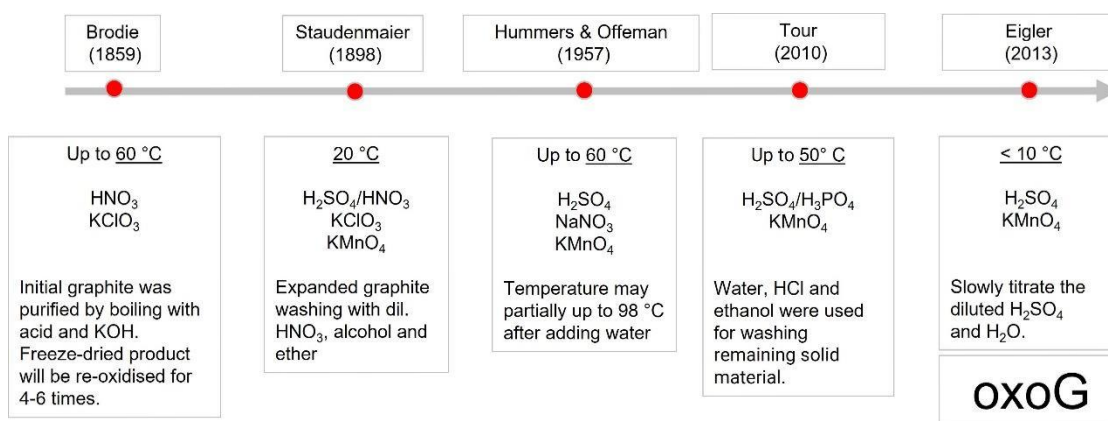


Figure 3. Synthetic methods of graphite oxide or GO. The figure mainly introduces the introduced time of different methods, the highest temperature, and the oxidant used.

Figure 3 illustrates the most important preparation methods developed in the last decades. Brodie's method is considered to be the earliest method to prepare to GO.⁵ It can be seen that all, namely Brodie's,⁵ Staudemaier's,⁷ Hummers' and Offemann's,²⁰ and Tour's²¹ methods comprise mixing graphite with a large excess of an oxidizing agent in sulfuric acid or nitric acid, followed by aqueous workup leading finally to graphite oxide.

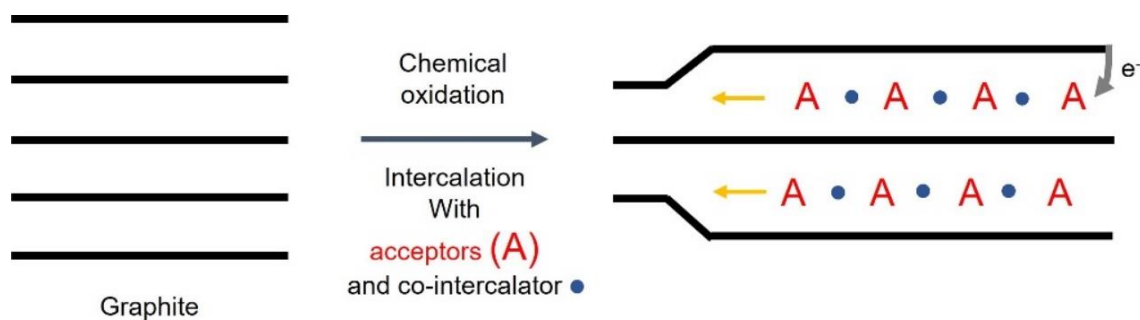


Figure 4. Illustration of the graphite oxidation. The intercalation of electron acceptors forms graphite intercalation compounds.

The first step in the preparation of graphite oxide formation is the formation of so-called graphite intercalation compounds (GIC, Figure 4). The interlayer distance of 0.335 nm in graphite (left) increases due to electron withdrawal from each graphene layer's positive charge by an oxidation agent, e.g. ammonium persulfate and concerted intercalation of a sulfuric acid/hydrogen sulfate guest layer neutralizing the positive charge. Pouring GIC into the water finally leads to graphite oxide. The oxidants used by most of the researchers are KClO_3 ⁵ and KMnO_4 ,^{7, 8, 13} etc. So far, the Hummers and Offemann method is the most popular: they use

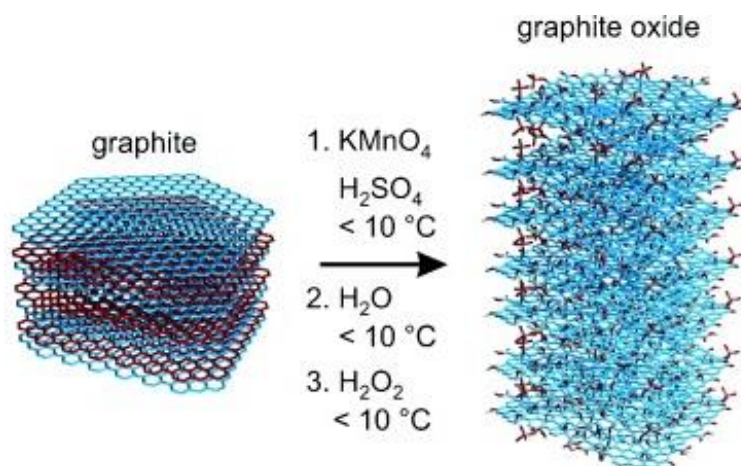


Figure 5. Synthesis of oxoG. Figure 5 was reproduced from the literature²⁴ with the permission of Wiley. The temperature is lower than 10 °C in the whole preparation process. The corresponding reagents are slowly added in steps 1, 2, and 3.

KMnO₄ as a strong oxidant in sulfuric acid, but this method has an obvious shortcoming, which will introduce sulfur species onto graphene oxide.¹³ Nevertheless, organosulfate can be hydrolyzed at 98 °C, as described by Hummers and Offeman.¹³ However, such a high temperature is likely to change the characteristics of GO and may introduce lattice defects.²²

To avoid over oxidation and exposure to high temperatures to form lattice defects, Eiger et al. slowly titrate dilute sulfuric acid and water to prevent temperatures higher than 10 °C during the reaction process to prepare oxoG, as shown in Figure 3.²³⁻²⁸ The preparation process is shown in Figure 5. It should be mentioned that before obtaining single layers of oxoG, only centrifugation is used instead of ultrasonication to get larger single-layer flakes. The length is about 20 μm.

3.3 Structure of graphene oxide

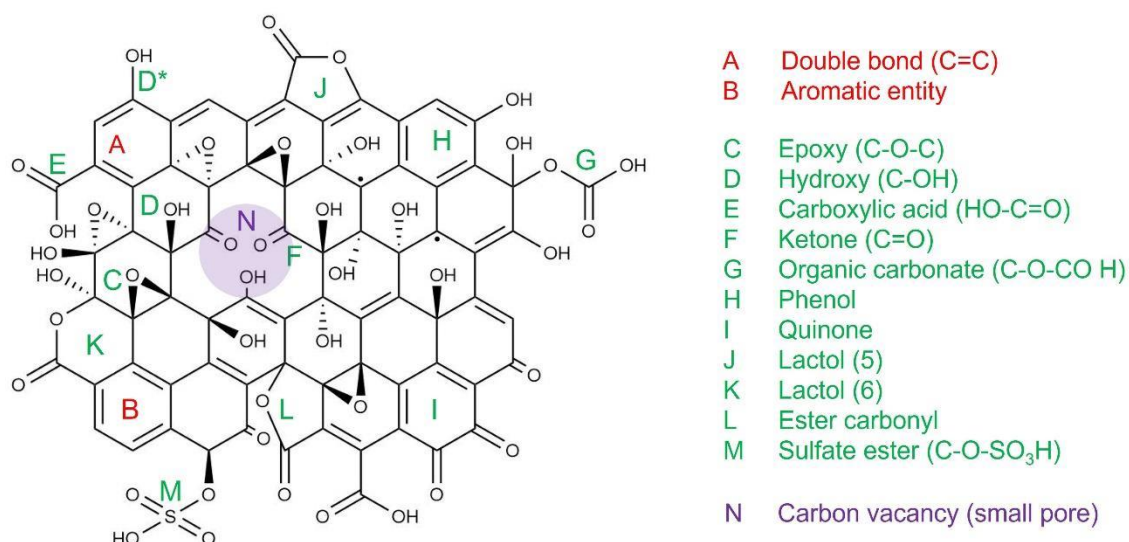


Figure 6. Structure of GO nanosheet.²⁹ The letters in the model correspond to the structure names listed.

GO is not a single molecule but more like a very complex material with a one-atom-thick fundamental carbon lattice. Its structure includes double bond (A), aromatic entity (B), a variety of oxygen-containing groups (C-L), vacancy defects (N), sulfate ester (M), etc.^{29, 30} Figure 6 refers to a review published in 2020 and shows the structure of a hypothetical GO nanosheet including possible structural motifs.²⁹ The model was proposed based on existing models (such as the Lerf-Klinowski model) and recently convincing experimental evidence.^{17, 18, 22, 31-43} Excessive oxidation at elevated temperatures during the preparation of graphite oxide will form permanent vacancy defects or small pores. Also, GO exposed to high temperatures can

undergo disproportionation of the hexagonal carbon framework. Thereby, the GO lattice decomposed partially and releases gaseous carbon monoxide or carbon dioxide leaving vacancies and pores behind, while some double bonds become partially regenerated.^{27, 44} As shown in Figure 6, carboxyl (E) and carbonyl groups (F) can only be found on the edges of graphene oxide and defects (small pores) because C-C bond cleavage is required in their formation.^{22, 45} Dimiev et al. used a dynamic structural model to explain the C-C bond cleavage. The C-C bond breaks and the carbonyl group is formed under mild alkaline conditions, as shown in Figure 7.⁴⁶

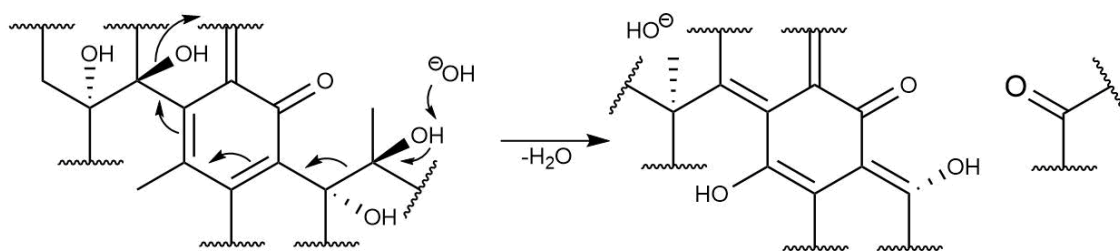


Figure 7. Dynamic structure model (DSM) of GO. This reaction illustrates the cleavage of C-C bonds caused under mild alkaline conditions and the formation of carbonyl groups.⁴⁶

High-resolution transmission electron microscopy (HRTEM) shows small pores in the GO sheet, and the size of the pores is generally less than 5 nm².¹⁸ Due to the limitation of extended lattice defects, these pores are difficult to expand in a controlled manner, which is also an important reason for designing the first work. By HRTEM and X-ray photoelectron spectroscopy (XPS) it is found that carbonyl groups are formed on the edge of the pore in the GO sheet.¹⁸

Raman spectroscopy can quantify defects in GO and reduced GO (refer to section 4.2 for details). The density of vacancy defects and the average distance (L_D) between two defects can be accurately calculated by Raman spectroscopy.^{25, 27, 47-51} Therefore, Raman spectroscopy can detect changes of functional groups or else lattice defects in GO or reduced GO and hence, help to understand possible effects of such defects in later experiments. As shown in Figure 8A, graphene without lattice vacancy defects is not reactive with aryl radicals whereas aryl radicals can functionalize defective graphene at positions in proximity to vacancy defects. Here, the degree of final functionalization depends on the initial density of defects or activated area, respectively. After the reaction, the triangular defect constellation's L_D and I_D/I_G ratios (ratio of the intensity of D peak and G peak in Raman spectra) illustrate the change in the L_D and I_D/I_G ratios.

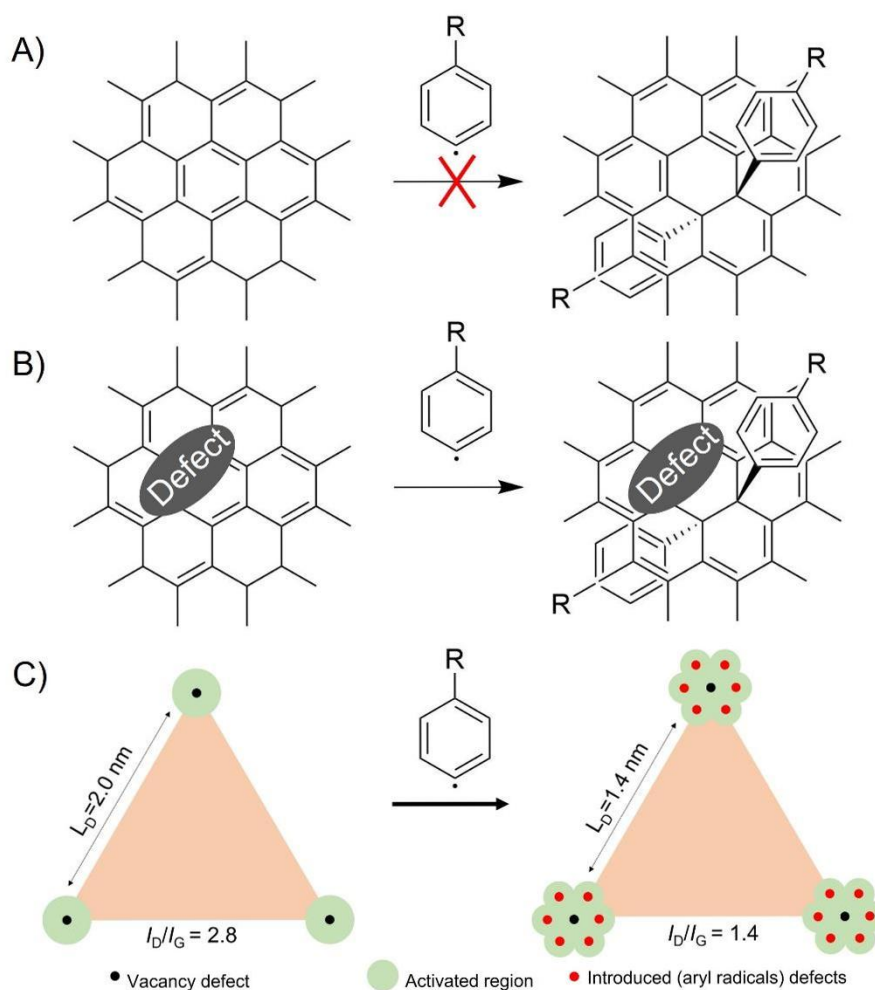


Figure 8. A) Aryl radicals cannot functionalize graphene without defect sites. B) The functionalization of graphene close to defect sites. C) The triangular defect constellation's L_D and I_D/I_G ratios illustrate the changes in the L_D and I_D/I_G ratios after functionalization.²⁵

3.4 Electrochemical properties of graphene oxide

There are many kinds of oxygen-containing groups, such as hydroxyl, carboxyl, carbonyl, on GO, which have electrochemical properties. Electrochemical reduction of GO is affected by the pH of electrolyte, as shown in Figure 9A, curves *a-d* are obtained by sweeping in various pH values. From *a* to *d*, the pH values are 4.12, 7.22, 10.26, 12.11, respectively. The reduction peak potential of GO shifts negatively as the pH value increases in Figure 9A.⁵² Electrochemical reduction involves the transfer of protons, promoting protonation at low pH values, thereby increasing the reduction rate. In Figure 9B, the contact part of the electrode and graphene oxide film and periphery transfer from original yellowish-brown to black. (Figure 9B, left). The electrode surface morphology remains unchanged after reduction (Figure 9B, right).⁵² Figure 9C shows four methods to produce graphite oxide.

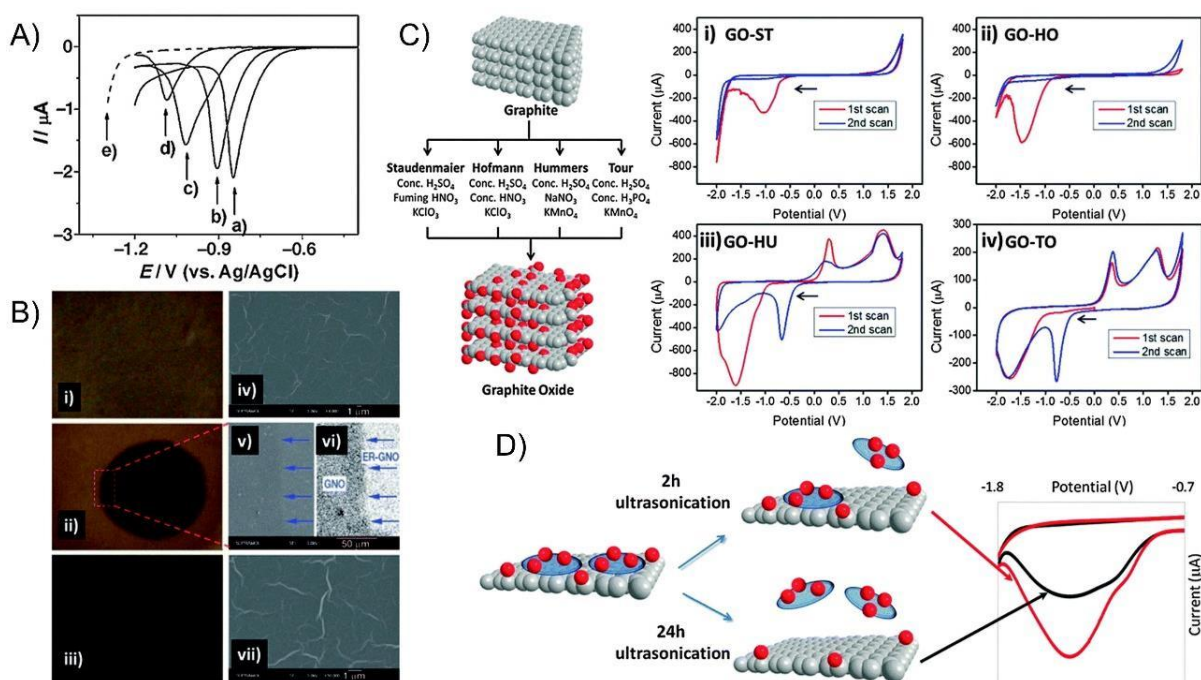


Figure 9. The unique electrochemical properties of GO. (A) Linear sweep voltammograms (a-e) of glassy carbon electrode contacting a GO film at various pH values. (e) Linear sweep voltammogram of glassy carbon electrode suspended in sodium phosphate buffer solution (pH=4.12). (B) Photos (i-iii) and scanning electron microscopy images (iv-vii) of graphene oxide films without electrochemical reduction (top), in reduction (middle), and reduction completed (bottom). Image (vi) is an enlarged view of the image (v). The arrow indicates the boundary between the restored area and the unreduced area. (C) Four methods of preparing graphite oxide. Figures (i) and (ii) are the cyclic voltammograms of GO prepared by Staudenmaier's and Hofmann's methods, respectively. Figures (iii) and (iv) are cyclic voltammograms of GO prepared by Hummers and Tour methods. Scanning starts at 0 V. The electrolyte is PBS (pH=7.2), Ag/AgCl electrode is the reference electrode. The sweep rate: 100 mV s^{-1} . (D) The oxidative debris (OD) is adsorbed on the larger GO flakes. The degree of desorption of 2 hours and 24 hours of ultrasonic desorption and its effect on the reduction peak. Figure 9 was reproduced from the literature.⁵³

All kinds of GO show reduction peaks but vary in the peak position. The reason here has not been clear so far. Besides, the reduction of GO obtained by Staudenmaier's (GO-ST) and Hofmann's (GO-HO) method is irreversible after the first reduction peak appears. While both samples of GO prepared by the ways of Hummer (GO-HU) and Tour (GO-TO) have redox properties. They hypothesize that the quinone-hydroquinone pair might be the source of redox properties of GO-HU and GO-TO. However, according to their XPS analysis, the oxygen content changes significantly after electrochemical reduction and re-oxidation (first decrease and then increase).^{53, 54} This seems to contradict the hypothesis that the quinone-hydroquinone pair might be the source of redox properties. Electrochemical reduction and

oxidation cause significant changes in the content of oxygen functional groups, but the precise structural changes are not clear. Oxidized fragments (OD) may mainly contribute to the observed electrochemical activity (Figure 9D). Extending the ultrasonication time can remove OD, which may be adsorbed on large sheets. After removing the OD (12 hours of ultrasonic treatment), the intensity of the reduction peak of the precipitated GO flakes decreased.⁵⁵

Note that the electrochemical reduction of GO generally requires the formation of a thin film on the electrode.^{53, 55-66} In the past ten years, there have been more and more researches on the permeability of GO membranes.⁶⁷⁻⁷¹ Therefore, in the aqueous electrolyte, does the permeability of the films affect the electrochemical reaction process, and how to predict the permeability of the films based on the electrochemical reduction phenomenon of the GO film? Both are issues worth exploring.

In addition, researchers have been trying to use GO as a potential material for sensors and catalysts, as well as in the field of energy storage.^{41, 53, 72-78} For example, GO is an electrocatalyst for oxygen reduction reaction to produce hydrogen peroxide.⁷⁹ Nevertheless, GO has a complex structure, so it is difficult to interpret its critical role in electrochemical reactions. Therefore, it is necessary to set GO derivatives with defined structures as a model to explain the electrochemical reaction mechanism.

3.5 Photoluminescence of MoS₂

A single layer of molybdenum disulfide (MoS₂) is a sandwich-type atomic layer composed of covalent Mo-S bonds, as shown in Figure 10. Single-layer MoS₂ exhibits photoluminescence (PL) due to its atomic-level thin layered structure and direct bandgap (1.8 eV).⁸⁰⁻⁸² Neutral excitons (A⁰) and other exciton complexes are the sources of PL emission of single-layer MoS₂.^{83, 84} The type of exciton is determined by the Coulomb interaction between holes and electrons. As a consequence, controlling the carrier concentration helps to modulate the PL efficiency. The inherent defects in the MoS₂ monolayer will cause unsaturated electrons and make them act as electron donors.^{85, 86} The existence of these defects will reduce the PL efficiency. There are many ways to enhance the PL of the MoS₂ monolayers, such as adding p-type organic dopants.⁸⁷ Studies have shown that the substrate affects both the Raman spectroscopy and PL performance of MoS₂ monolayers.⁸⁸ Transfer MoS₂ monolayers to different 2D materials (such as graphene) to form heterostructures. The heterostructure can regulate PL emission.^{89, 90}

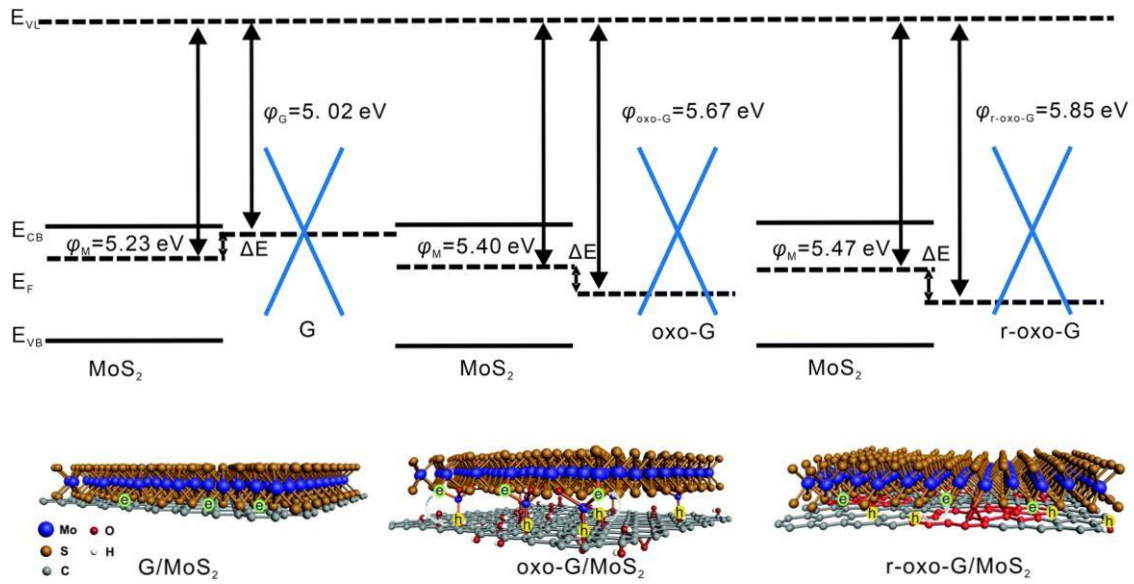


Figure 10. Energy-level diagram of single-layer MoS₂ on single-layer graphene, single-layer oxo-G, and single-layer reduced oxo-G (top). The interface polymerization mechanism of three heterojunctions (bottom). Figure 10 was reproduced from the literature⁹⁰ with the permission of RSC.

For example, Single-layer oxo-G, single-layer reduced oxo-G (r-oxo-G), and single-layer are used as substrates to form heterostructures with single-layer MoS₂, as shown in Figure 10. Residual oxygen functional groups, vacancy defects, and edge defects in the single-layer r-oxo-G disturb the sp² structure. So the work function value (the difference between the Fermi level and the vacuum level) of single-layer r-oxo-G (5.85 eV) is the biggest among that of single-layer oxo-G (5.67 eV) and single-layer graphene (5.02 eV). The work function value of the single-layer MoS₂ on the single-layer r-oxo-G is the highest (5.85 eV) compared to the other two cases, which means the highest degree of p-doping. As shown in the bottom schematic diagrams of Figure 10, electron transfer occurs at the heterostructure interface. Electrons are transferred from MoS₂ to G in the heterostructure of MoS₂/G. In the heterostructure of r-oxo-G/MoS₂, the complex defects and electron-withdrawing groups in r-oxo-G play a role, while the hole concentration of the monolayer MoS₂ also further increases. This recombination of electron-holes enhances the PL of MoS₂.⁹⁰

4. Methods

4.1 Langmuir-Blodgett technique

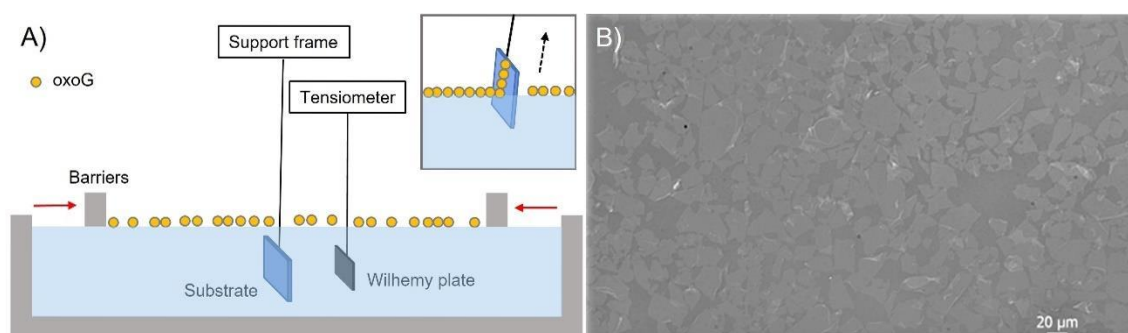


Figure 11. A) Schematic illustration of LB assembly of oxoG monolayers. B) Optical image of oxoG flakes on a Si/SiO₂ substrate.

Langmuir-Blodgett (LB) assembly is a technique for assembling a highly ordered thin film. The process occurs at the air-water interface. The method has been routinely used in the laboratory to prepare monolayers.⁹¹

Prior to the LB monolayer film formation, the monolayer flakes of GO solution are mixed with an organic solvent (methanol). Here, Methanol is beneficial for several reasons: a) it decreases the density of the used GO dispersion so that it can be better dropped onto the surface. b) it can enhance dispersibility for some GO derivatives. Subsequently, the mixed solution is added dropwise into the trough filled with double-distilled water. As shown in Figure 11A, as the methanol evaporates, the oxoG is trapped on the water surface, forming a monolayer. Then the moving barrier is used (red arrow) to adjust the intermolecular distance. Finally, the oxoG film can be transferred to a vertically extracted solid substrate (silicon wafer with 300 nm SiO₂ surface) to form a large-area single-layer coating (Figure 11A inset and Figure 11B). Polymer monolayers⁹² and nanomaterials⁹³ can be prepared similarly. A Wilhelmy plate monitors the surface tension of water. So, a few layers can be obtained by tuning the surface tension. Besides, the monolayer coating on the substrate can be transferred, reduced, or functionalized for later micro/nanodevice manufacturing. Therefore, the preparation of large-area, wrinkle-free single-layer oxoG is of great significance for the research of sensors and other electronic devices.

4.2 Raman spectroscopy

The inelastic Raman scattering process is a photon absorption-emission process, and it is the most vital tool to characterize graphene. As shown in Figure 12A, the Raman scattering process occurs through virtual states. In the Raman spectrometer, the Rayleigh scattering wavelength is removed by a filter. to obtain the Raman scattering wavelength. Photons emitted from the laser interact with the probed 2D material leading to phonons in the materials with a certain energy, usually given as a value of relative energy value shifted to the excitation wavelength. Stokes scattering is the emission of photons with lower energy than the excitation wavelength, and anti-Stokes scattering is the emission of photons with higher energy than the excitation wavelength.

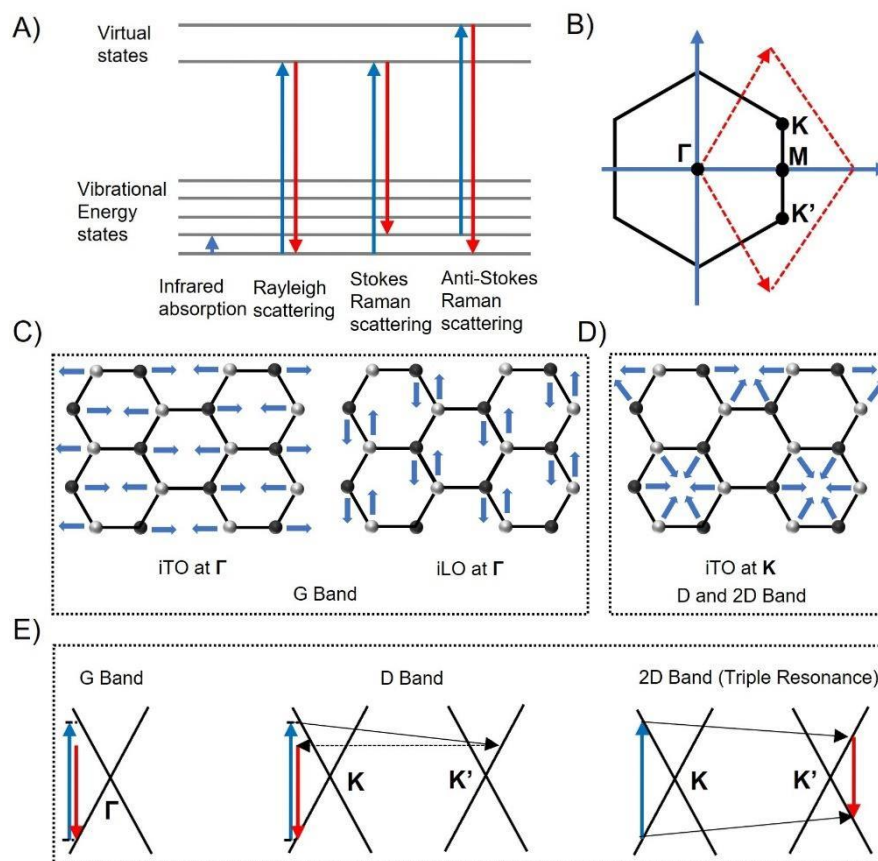


Figure 12. A) Energy-level diagrams of different states in Raman spectroscopy.⁹⁴ B) The Brillouin zone of graphene. The red prism is the first phonon Brillouin zone. C) Schematic diagram of phonon vibration in graphene. G-band mode of iTO and iLO phonons at Γ point. C) The D and 2D bands mode is that the iTO phonon vibrates at point K. The i means in-plane. E) Illustrations of the excitation and emission in G band (left), D band (middle), and 2D band (right).⁹⁵

Raman spectroscopy is often applied in analyzing the disorder in the sp^2 network of the graphene. As shown in Figure 13C, the G mode occurs at 1580 cm^{-1} representing the in-plane stretching vibration of the sp^2 hybridization of C atom. The D mode ($\sim 1345\text{ cm}^{-1}$) of the Raman spectrum represents the degree of disorder. The 2D mode occurs at about 2700 cm^{-1} which can be used to determine the number of graphene layers.⁹⁶ Figure 12B shows the Brillouin zone of graphene and the points Γ , K, and K'. The two stretching vibration modes of the C-C bonds are related to the G band. The transverse optical mode (TO) and longitudinal optical (LO) mode at Γ are shown in Fig. 12C. Incident or scattered photons vertically excite electron-hole pairs and emit photons after the electron-hole pair radiation recombines, thereby forming the G band (Figure 12E, left). The D-band and 2D-band involve a double resonance (DR) process near the K point. This process is activated by the interval scattering of electrons excited by the combination of two TO phonons (Figure 12D). In the D band, electrons are inelastically scattered by TO phonons to point K' and then elastically backscattered to point K by intrinsic defects or introduced defects (Figure 12E, middle). The 2D band also contains a triple resonance process near the K point (Figure 12E, right). This band can be used to determine the number of graphene layers.

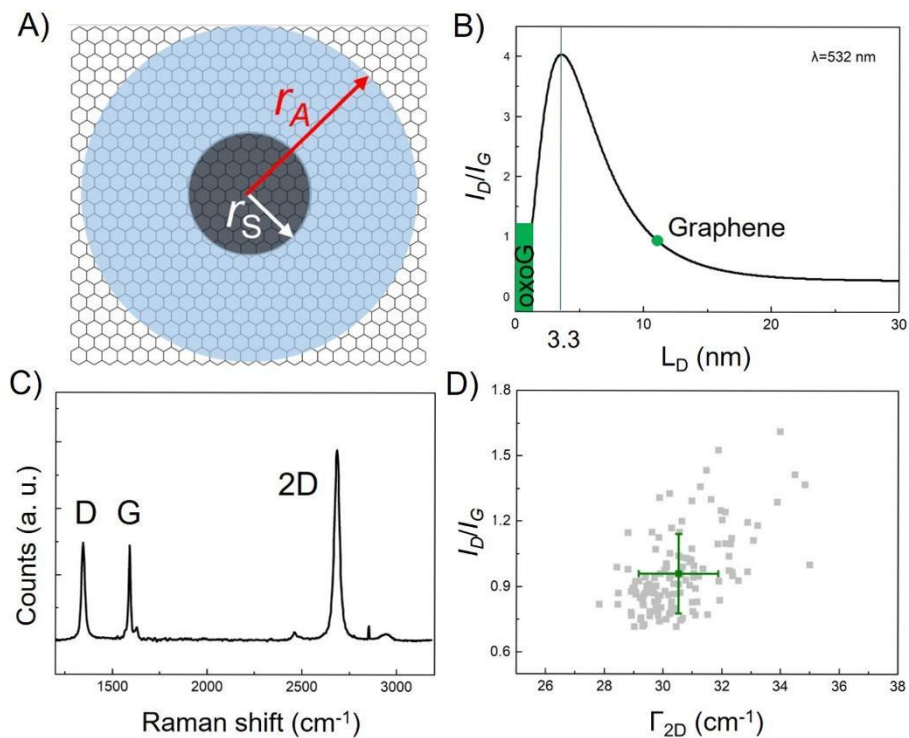


Figure 13. A) r_A and r_S are the radius of the activated region and structurally disordered region. The black area is S-region. The blue area is A-region. B) Relation between I_D/I_G and L_D fitted by Cançado and Lucchese's mode.^{48, 51} C) Average Raman Spectra of graphene with defects. D) Statistical Raman spectroscopy of graphene with defects. Relation between I_D/I_G and L_D of graphene with defects shows in Figure B green dot.

The relationship between I_D/I_G ratio and L_D (Figure 13B) is, as shown below, based on the model proposed by Cançado and Lucchese et al.^{48, 49, 51}

$$\frac{I_D}{I_G} = C_A \frac{r_A^2 - r_S^2}{r_A^2 - 2r_S^2} \left[e^{-\pi r_S^2 / L_D^2} - e^{-\pi(r_A^2 - r_S^2)r_S^2 / L_D^2} \right] \quad (1)$$

Here, r_A and r_S represent the length of the active region and the structural disorder region, respectively. The black area is structurally disordered in Figure 13A, and the blue area is the active area. The lattice in the active region remains unchanged. However, the defects that are close to each other cause the D band to decrease because additional defects silence other defects.

As shown in Figure 13B the curve is divided into a low-defect density regime ($L_D \geq 3.3$ nm) and a high-defect density regime ($L_D \leq 3.3$ nm).^{48, 49, 51} Starting with ideal graphene, the introduction of defects would lead to a reduction of the sp^2 network, whereby I_D increased first relative to I_G until a maximum is reached, and then decreases again. As D, G and 2D mode generally broaden with increasing density of defects same I_D/I_G ratios in two regions can be easily distinguished by e.g. including the full-width-at-half-maximum of 2D peak (Γ) into the interpretation, as shown in Figure 13D.

4.3 X-ray photoelectron spectroscopy

X-ray photoelectron spectroscopy (XPS) is used for the chemical analysis of the surface of materials. The types and approximate content of elements can be obtained by this technique. Obtained signals can be deconvoluted to get fine information about the binding situation. Using reduced GO as an example, XPS can detect the varieties of elements. According to binding energy, the ratio of different oxygen-containing groups is obtained through peak fitting processing (Figure 14B). However, XPS has some disadvantages. For example, it is costly, needs to be tested under high-vacuum conditions, and is even time-consuming. In addition, fitting procedure is also easily falsified. Figure 14C shows the working process of XPS. In a vacuum environment. X-rays irradiate the samples' surface, and as-formed photoelectrons are forced through the electronic lens and then reach the electronic analyzer. Finally, the number of electrons is counted in the detector. The electrons are collected from the top 3-7 nm of the sample.

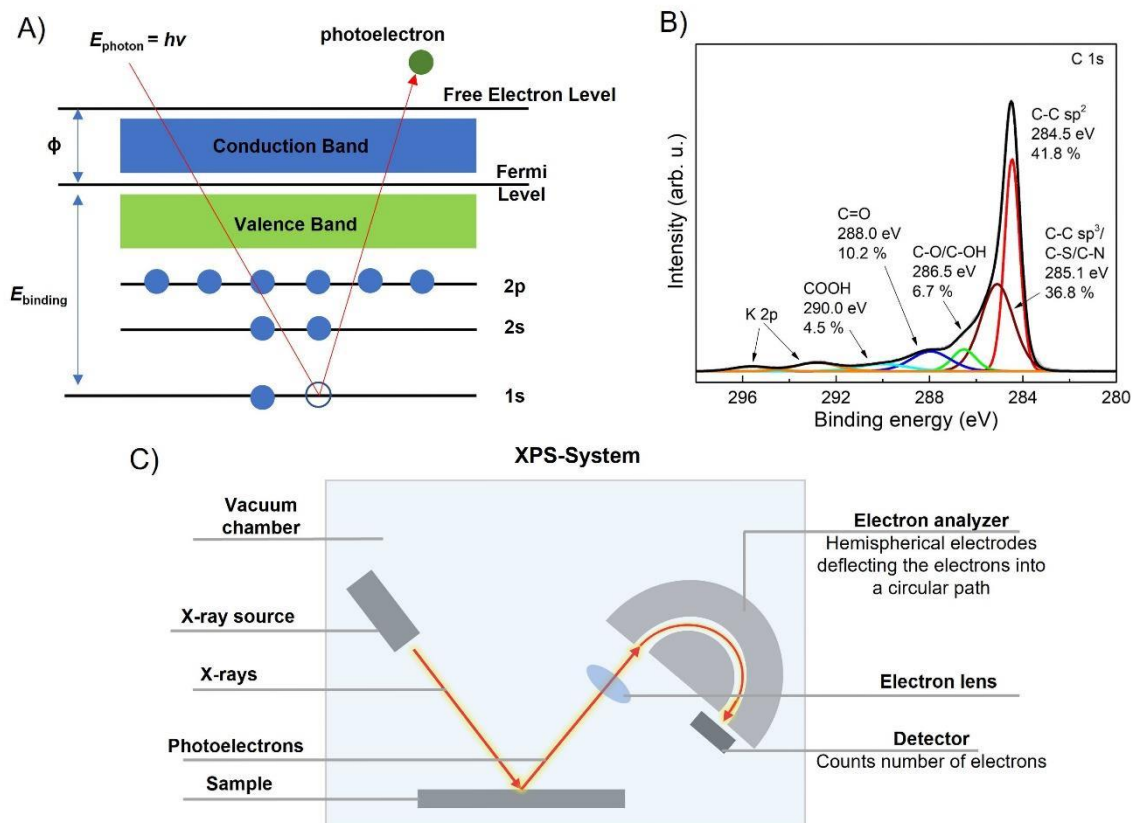


Figure 14. A) Emission of a photoelectron. B) high-resolution C 1s XPS spectra of heat-treated GO. C) The Components of XPS instrument include vacuum chamber, X-ray source, sample platform, electron lens, electron analyzer, and detector, etc.

The principle of this method is based on the law of conservation of energy shown as follows.

$$E_{\text{binding}} = E_{\text{photon}} - (E_{\text{kinetic}} + \phi) \quad (2)$$

Here, the binding energy (E_{binding}) represents the energy of a nucleus to trap an electron; E_{photon} represents the X-ray photons' energy. The kinetic energy (E_{kinetic}) represents the energy of the electrons emitted from the sample. The work function (ϕ) and E_{photon} are known, and the detector can measure E_{kinetic} . Therefore, E_{binding} can be calculated according to the energy conservation equation. The process of emission of photoelectron is shown in Figure 14A.

4.4 Atomic force microscopy

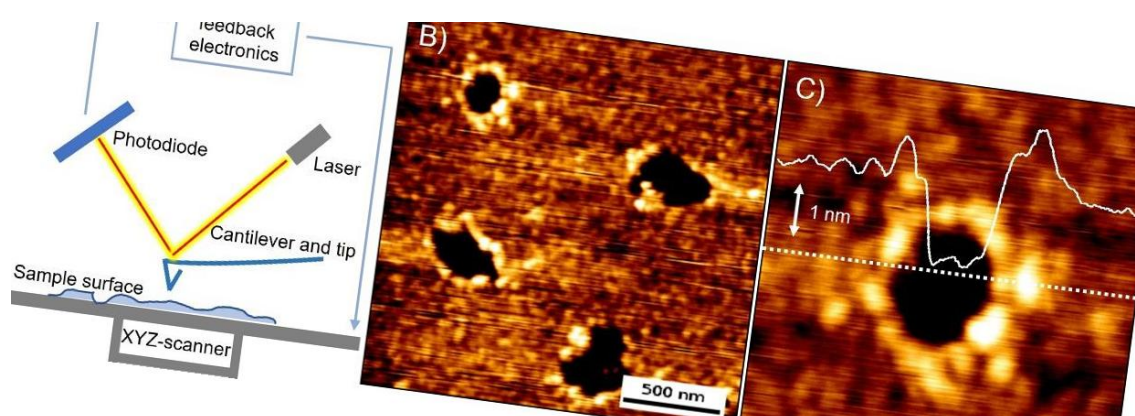


Figure 15. A) The Components of AFM instrument. B, C) AFM images of single-layer GO with pores. The inset of Figure C shows the height of the single-layer GO with pore.

Atomic force microscopy (AFM) can be used to explore the surface properties of materials. As illustrated in Figure 15, one end of the cantilever is fixed while the tip is on the other end scans an area in the XY direction. Depending on the chosen distance between tip and substrate there is either a weak attractive or repulsive force between both bringing the cantilever a slight deflection. The sample surface image can be almost simultaneously obtained by detecting the degree of deflection and applying feedback to control the repulsive force to be constant (Figure 15). AFM has three main imaging modes, including intermittent, contact and non-contact modes. Among them, the intermittent mode (tapping mode) is that the probe maintains a fixed frequency vibration on the Z-axis through a feedback loop, which is a dynamic mode. The effect of van der Waals forces, dipole-dipole interaction and the electrostatic force causes the oscillation frequency to change. It is suitable for detecting materials such as graphene and GO.⁹⁷ This mode can achieve high-resolution imaging of the sample surface and get the height of materials. For example, morphology single-layer GO with pores is shown in Figure 15B. Due to the presence of oxygen functional groups and some folds, the height of single-layer GO with pore is over 1.2 nm in Figure 15C.

4.5 Transfer technique of 2D materials

The two-dimensional material transfer and stacking process can be divided into three steps: first, the top material is prepared; second, the top material is transferred to the bottom 2D material or stacked in a specific position; third, the Carrier removal.⁹⁸ The transfer process includes dry transfer and wet transfer.⁹⁸⁻¹⁰¹ Compared with the wet transfer, the dry transfer process can obtain a cleaner and higher quality heterostructure.⁹⁸ In our work, the bottom

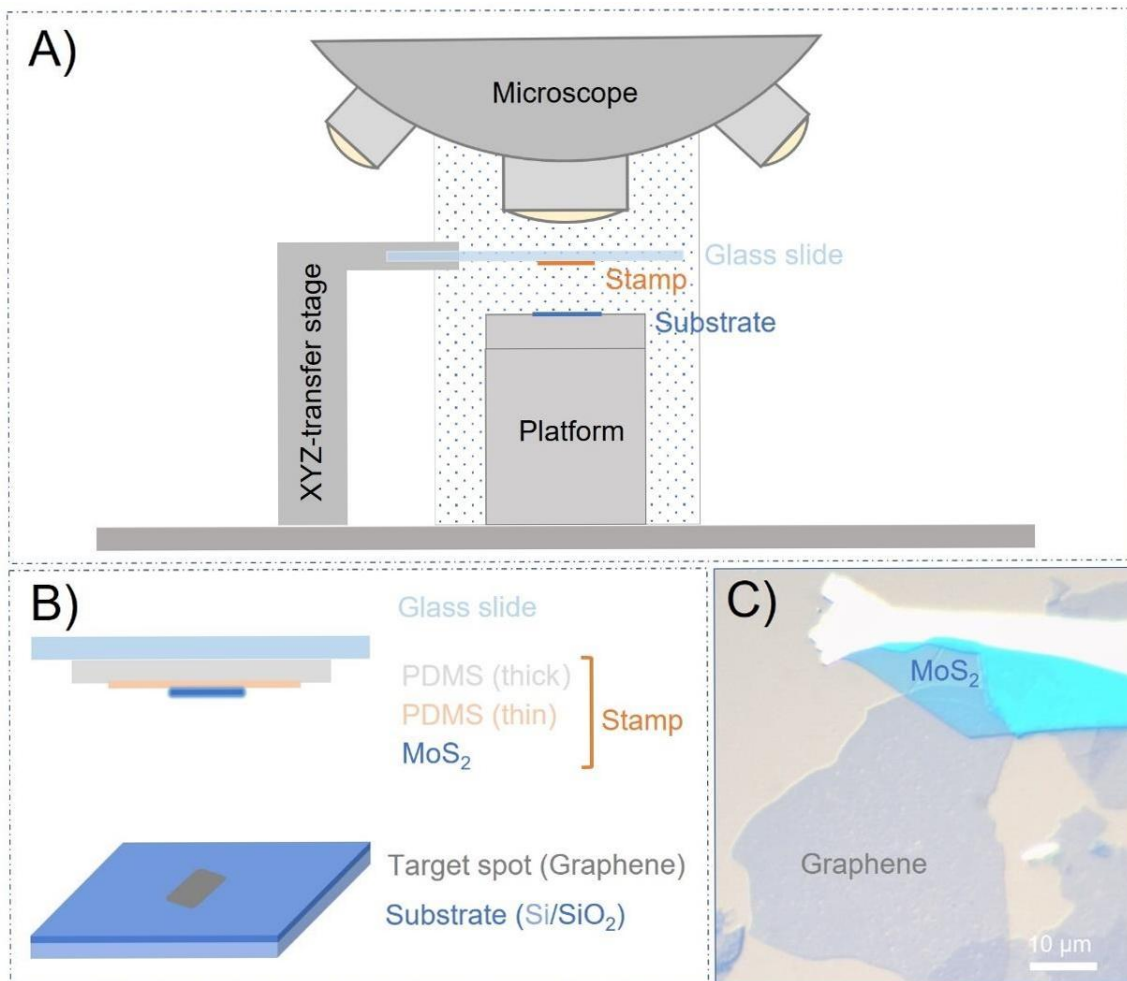


Figure 16. A) Part of the transfer system. B) Schematic illustration of the preparation of the MoS₂/graphene heterostructure. C) optics image of the MoS₂/graphene (with pores) heterostructure.

material is a single layer of oxoG with holes. Dry transfer technology can be used to directly stack the stripped single layer of top material on the monolayer of oxoG with holes. The main part of the transfer system contains an optical microscope, a high-precision transfer stage, and a platform (Figure 16A). A glass slide is fixed on the transfer stage, and generally, a thick layer of PDMS adheres to the glass slide. For example, the preparation of MoS₂/graphene heterostructure is shown in Figure 16B. The single-layer MoS₂ remains on the thin PDMS, which is adhered to the thick PDMS before the transfer, and the substrate with the target spot (monolayer graphene) is fixed on the platform. During the transfer process, the transfer stage is adjusted in the three directions of X, Y, and Z to promote the alignment and compaction of the two 2D materials. Figure 16C shows the optical image of MoS₂/graphene heterostructure, the outline of graphene is still clearly visible through MoS₂.

4.6 Cyclic voltammetry

Cyclic Voltammetry (CV) is an electrochemical analysis method. This technique can be used to analyze the electrochemical characteristics of the substances diffused on the electrode surface and the overall properties of the materials loaded on the surface of the electrode.^{102, 103} CV measurement relies on a typical three-electrode cell system. As shown in Figure 17A, a working electrode (WE) can be a glassy carbon electrode. Ag/AgCl electrode is one of the most used reference electrodes (RE) in electrochemical analysis. Platinum wire can be used as a counter electrode (CE). Three electrodes form two loops, one is used to measure the potential, the other is used to measure the current, the loop is composed of the working electrode and the reference electrode is used to test the potential of the electrode, because the potential of the reference electrode is known. For example, the reference electrode reaction is: $\text{AgCl} + e^- = \text{Ag} + \text{Cl}^-$, and its potential is also affected by the concentration of Cl^- . The electrode potential when KCl is saturated is 0.199 V. The reference electrode has good reversibility and high exchange current density. The electrode potential can quickly return to its original state when a small current flows; it has good potential stability and reproducibility. When measuring the working electrode's potential, the composition of the solution in the reference electrode and the solution of the system under study are often different. Use a salt bridge to connect the reference electrode with the measured solution to reduce or eliminate the liquid junction potential. In order to reduce the uncompensated solution resistance, Luggin capillaries are often used.

The potentiostat can apply a voltage between the electrodes. The waveform of the applied potential is triangular (Figure 17E). The potential scan starts from the initial potential where no reaction occurs, scans to a potential, and then sweeps in the opposite direction to the initial potential. Provided that O (Such as ferricyanide) is an electroactive material (Oxidized substances), substances), O is electrochemically reversible and can be reduced afterward.

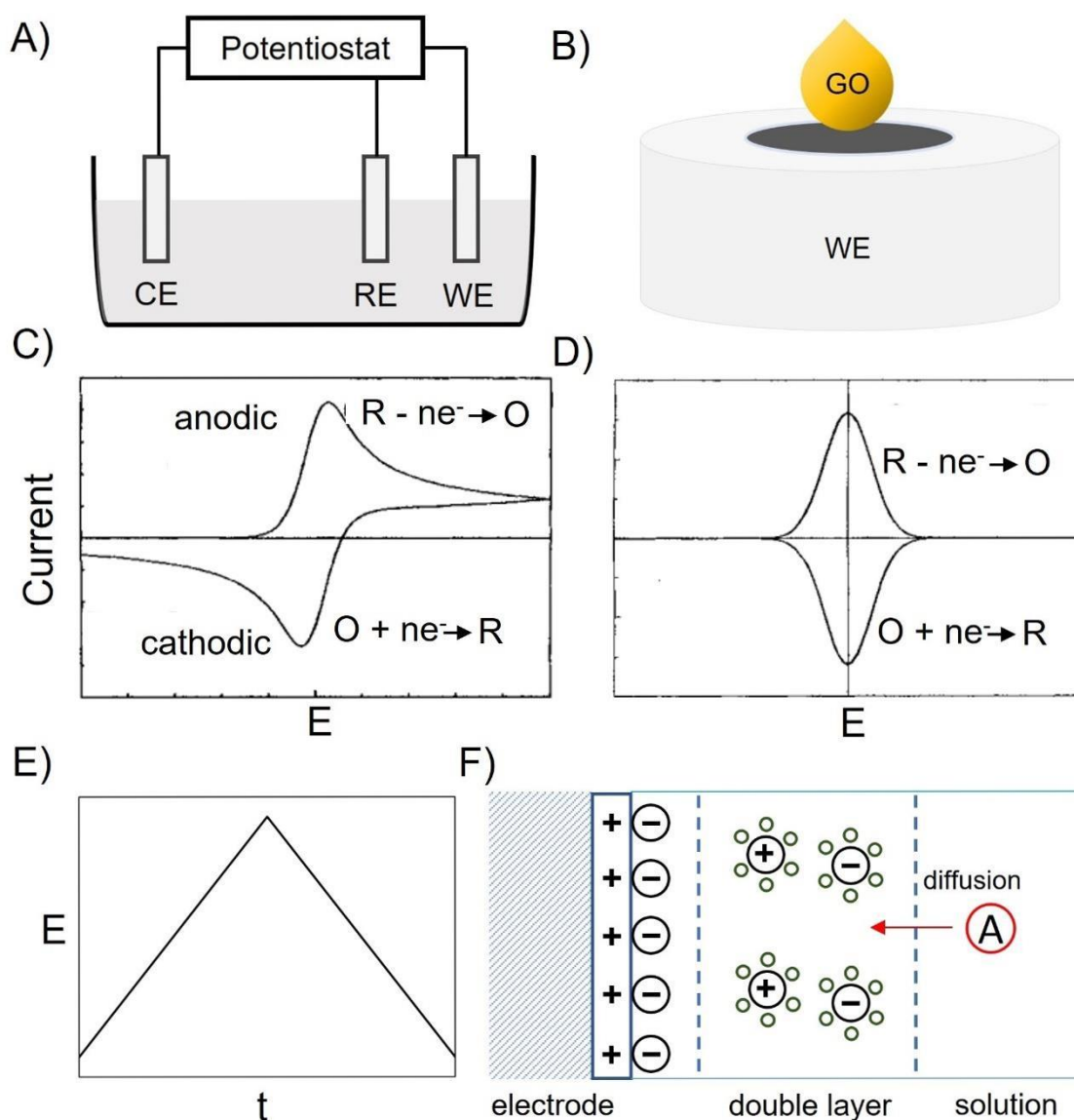


Figure 17. A) Composition of three-electrode cell. B) GO solution is dropped on GCE to form a thin film. C) 'Bird-neck' shape of CV, and D) an ideal redox reaction in an ultra-thin film. E) The time-varying triangular applied potential program wave. F) Electric double-layer model of the positively charged electrode surface. Figure 17C and D were reproduced from the literature.¹⁰²

As shown in the following reaction, n is the count of transferred electrons.



Where R is reduced substances. This reaction is a diffusion-control process, and the current is affected by the diffusion of O to the electrode surface. In Figure 17F, there is an electric double layer on the electrode surface. The active substance (A), here referring to O, diffuses through the electric double layer to the electrode surface. Cyclic voltammetry can be used to determine the reaction is reversible or not. As shown in Figure 17C, there is a voltammogram that shows a typical graph for a reversible reaction containing the oxidation and reduction

peaks. In a reversible reaction, the two peak currents (i_p) rate is approximately equal to 1. The peak current of the reversible voltammogram at 25 °C is given by Eq. 4, where v is the scan rate, A is the electrode area, C_0 is the concentration of O and D is the diffusion coefficient.

$$i_p = (2.69 \times 10^5) v^{\frac{1}{2}} D^{\frac{1}{2}} C_0 A \quad (4)$$

Preparing a film on the WE is necessary to study its properties by cyclic voltammetry (as shown in Figure 17B, drop-cast GO on the glassy carbon electrode). Assuming that such a film contains O, an ideal cyclic voltammogram (Figure 17D) appears when the scan rate is very low, indicating that all O species react during the scan. In this case, the peak current has a linear relationship with the scan rate (Eq. 5), where Γ_s is the number of moles of O per cm⁻² of electrode area, and R represents the gas constant. T represents the temperature. F is Faraday constant. In Equation 6, where Q is the passed charge, it can be obtained by integration.

$$i_p = \frac{F^2 A \Gamma_s v}{4RT} \quad (5)$$

$$\Gamma_s = \frac{Q}{FA} \quad (6)$$

In practice, researchers rarely get an ideal curve shown in Figure 17D. The potential of peaks is affected by the film in different conditions, such as the interaction between the electroactive substances in the film. An ideal state will appear when the time taken to scan the peak is longer than the time constant d^2/D_{ct} (d is the film thickness and D_{ct} is the charge transport diffusion coefficient) for charge diffusion through the film. When the sweep speed is very high, only a part of the active material in the film will be reacted. A diffusion layer of O is generated close to the electrode surface. When the diffusion layer is much thinner than the thickness of the film, the electron transfer rate is fast, corresponding to the case in Figure 17C. At this time, D in Equation 7 becomes D_{ct} . C_0 is the concentration of O in the film. Note that the ideal cyclic voltammogram we discussed is only suitable for fast and reversible reactions. Otherwise, slow electron transfer will cause a larger difference of peak potential between the oxidation peak and the reduction peak. If O and R participate in other chemical reactions, it becomes an irreversible reaction.^{102, 103}

4.7 Rotating ring-disk electrode test

The glassy carbon electrode used as a chemically modified electrode requires a very clean surface, no stains, and good activity. However, when the glassy carbon electrode is not used for a long time, an oxide film will form on the surface. The glassy carbon electrode is polished on the suede with alumina powder of different particle sizes. In the polishing process, Hold the glassy carbon electrode vertically and an "8" shape is drawn. Before polishing, gently wipe the surface of the electrode with moist lens paper to remove dirt and ensure that the surface of the electrode is smooth.

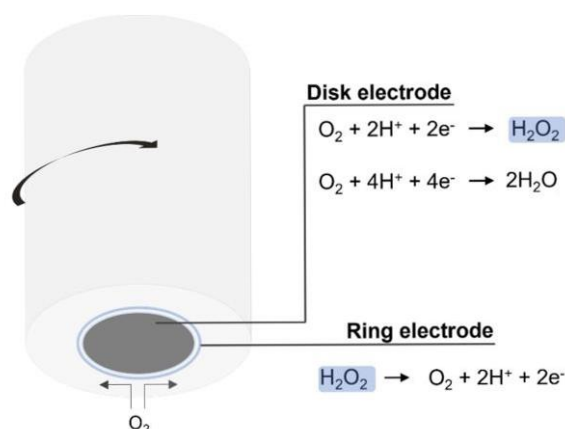


Figure 18. The Schematic illustrates the principle of the selective test for oxygen reduction to H_2O_2 .

Calculate the number of electron transfer (n) and the hydrogen peroxide yield through equations 7 and 8.^{79, 104, 105} Here, I_R is ring current. I_D is disk current. N is collection efficiency (0.37).

$$n = \frac{4I_D}{I_D + I_R/N} \quad (7)$$

$$\text{H}_2\text{O}_2 \% = 200 \times \frac{I_R}{N \times I_D + I_R} \quad (8)$$

The electrocatalytic oxygen reduction reaction includes two-electron and four-electron pathways. The product of the four-electron pathway is water, and the product of the two-electron transfer pathway is hydrogen peroxide, as described in Figure 18. The local hydrophilicity of the catalyst at active sites is vital for producing H_2O_2 . The hydrophobic surface limits the accessibility of the electrolyte at the reaction interface.^{105, 106}

5. Main contributions

5.1 Synthesis of wet-chemically prepared porous-graphene single layers (Contain oxygen-containing groups) on Si/SiO₂ substrate increasing the photoluminescence of MoS₂ in heterostructures.

The single-layer graphene deposited on the substrate can be chemically functionalized.¹⁰⁷ This functionalized graphene is a potential material for the preparation of sensors.¹⁰⁸ The functionalization process of the deposited single-layer graphene can occur on the surface and edge of the sheet. The size of the sensing device generally reaches the μm level, so functionalization only at the edge cannot effectively improve the sensing performance. Therefore, holes can be fabricated in graphene to increase the proportion of edges. There have been some reported methods for making holes at the single-layer level, such as focused ion beam etching of holes.^{109, 110} The focused ion beam interacts with the substrate and damages the dielectric layer.^{109, 111} Graphene oxide is used as a precursor to obtaining GO with holes, but the diameter of the holes is a few nanometres. Too many lattice defect sites exist in the graphene oxide. These defects serve as the starting point of the etching, but the decomposition of the flakes makes the macropores unavailable.^{112, 113}

Here, I use the method of heat-treating (400 °C) a single layer of oxoG to prepare uniform circular holes. Pores with a diameter of 100-200 nm can be obtained with the assistance of Mn-species. In the process of fabricating the macropores, the decomposition of graphene oxide is avoided. An optical microscope and AFM are used to obtain images of graphene with pores. I use ImageJ to count the pore size. Single-layer graphene with holes has good stability, no wrinkles and can be used as a bottom material to prepare heterostructures with MoS₂. This structure enhances the photoluminescence (PL) of MoS₂ by 10 folds.

Authors	Y. Wang, C. Neumann, M. Hußmann, Q. Cao, Y. Hu, O. Garrity, P. Kusch, A. Turchanin and S. Eigler
Journal	Adv. Mater. Int., 2021, 8, 17, 2100783
DOI	10.1002/admi.202100783
	https://creativecommons.org/licenses/by/4.0/
	The concept of this manuscript was elaborated by Y. Wang and Prof. Dr. S. Eigler.
Detailed scientific contribution	<p>OxoG and oxoG with pores were fabricated and characterized with optical microscopy and atomic force microscopy by Y. Wang. X-ray photoelectron spectroscopy was measured by C. Neumann. Photoluminescence and Raman measurement were done by M. Hußmann, Q. Cao, Y. Wang and Y. Hu. Heterostructures were prepared by Q. Cao and Y. Wang. PL intensity maps were done by O. Garrity and P. Kusch.</p> <p>The manuscript was written by Y. Wang and Prof. Dr. S. Eigler. The revision of the manuscript was assisted by Prof. Dr. S. Eigler, Dr. C. Neumann, and Prof. Dr. A. Turchanin.</p>
Estimated own contribution	~60 %

Synthesis of Wet-Chemically Prepared Porous-Graphene Single Layers on Si/SiO₂ Substrate Increasing the Photoluminescence of MoS₂ in Heterostructures

Yiqing Wang, Christof Neumann, Marleen Hußmann, Qing Cao, Yalei Hu, Oisín Garrity, Patryk Kusch, Andrey Turchanin, and Siegfried Eigler*

Wet-chemical generation of pores in graphene is a challenging synthetic task. Although graphene oxide is available in large quantities and chemically diverse, extended lattice defects already present from synthesis hamper the controlled growth of pores. However, membrane, energy, or nanoelectronic applications essentially require uniform pores in applications. Here, oxo-functionalized graphene (oxoG), a type of graphene oxide with a controlled density of vacancy defects, is used as starting material. Pores in graphene are generated from potassium permanganate treated oxoG and heating from room temperature to 400 °C. With etching time, the size of pores increases and pore-diameters of, for example, 100–200 nm in majority become accessible. The experiments are conducted on the single-layer level on Si/SiO₂ wafers. Flakes remain stable on the μm scale and do not fold. The process leads to rims of pores, which are functionalized by carbonyl groups in addition to hydroxyl and carboxyl groups. In addition, it is found that heterostructures with intrinsically n-doped MoS₂ can be fabricated and photoluminescence (PL) measurements reveal a 10-fold increased PL. Thus, graphene with pores is a novel highly temperature-stable electron-accepting 2D material to be integrated into van der Waals heterostructures.

1. Introduction

Graphene with defects, such as pores in the lattice of graphene^[1–3] finds emerging applications for water separation, gas separation and purification, or sensing.^[4–10] The chemical functionalization of graphene can either be accomplished with graphene dispersed in solvents,^[11] or with graphene deposited on surfaces.^[12] Applications based on bulk functionalization target, for example, composite formation, exploiting the mechanical properties of graphene, or electronic properties for energy applications and energy conversion or storage.^[13–19] In particular sensing applications are targeted using graphene, which is deposited on surfaces. Thereby, functionalization of deposited graphene can in principle occur on the surface or at the rim of flakes. However, since investigated sensing devices typically have μm dimensions, functionalization at rims of flakes is supposed to have only little influence on the device performance. With drilling

pores into the graphene lattice, the proportion of rims can be increased. In principle, pores can be etched using focused ion beam and the approach allows for regular patterning, shape, and size control.^[16,20–22] Thereby, the successful patterning is a technological challenge. Since the focused ion beam also interacts with the substrate the dielectric layer, such as SiO₂ may become damaged. Thus, although that approach is appealing, it bears some drawbacks, since high-end technology is required.^[16,23]

The growth of pores in graphene on the single-layer level is described by numerous methods in the literature in particular etching methods.^[24] Nanometer-sized pores were created in graphene by oxygen plasma or other plasmas.^[25,26] Moreover, pores on the nanoscale were created in few-layered graphene using oxygen, ozone, or liquid phase etching using HNO₃ solution as etching reagents.^[26–28] In addition, it is reported that a single Ni atom can be used to cut graphene to a nanomesh with a pore size of about 10–50 nm.^[29] Sub-nanometer diameter pores in single-layer graphene membranes were also fabricated, accordingly, defects were introduced into the graphene lattice through ion bombardment and oxidative etching enlarged defects into pores with sizes of 0.40 ± 0.24 nm.^[30,31] Moreover, also graphene oxide

Y. Wang, M. Hußmann, Q. Cao, Y. Hu, Prof. S. Eigler
Institute of Chemistry and Biochemistry
Freie Universität Berlin
Takustraße 3, 14195 Berlin, Germany
E-mail: siegfried.eigler@fu-berlin.de
Dr. C. Neumann, Prof. A. Turchanin
Institute of Physical Chemistry
Center for Energy and Environmental Chemistry (CEEC) Jena
Friedrich Schiller University Jena
Lessingstraße 10, 07743 Jena, Germany
O. Garrity, Dr. P. Kusch
Department of Physics
Freie Universität Berlin
Arnimallee 14, 14195 Berlin, Germany

 The ORCID identification number(s) for the author(s) of this article can be found under <https://doi.org/10.1002/admi.202100783>.

© 2021 The Authors. Advanced Materials Interfaces published by Wiley-VCH GmbH. This is an open access article under the terms of the Creative Commons Attribution License, which permits use, distribution and reproduction in any medium, provided the original work is properly cited.

DOI: 10.1002/admi.202100783

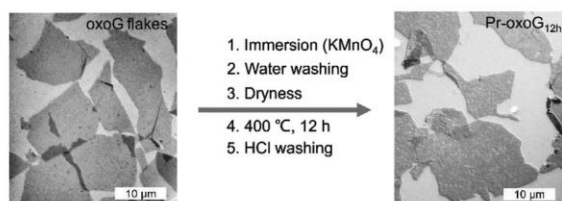


Figure 1. Scheme describing the fabrication of pores starting from oxoG. Flakes of oxoG are deposited on a Si/SiO₂ substrate. Pr-oxoG_{12h} is fabricated from oxoG, immersed in KMnO₄ solution, followed by washing, drying, and annealing in argon atmosphere at 400 °C for 12 h. The white scale bar relates to 10 μm in optical microscopy images.

was used as precursor for etching pores, however, no uniform size was reported and the size of pores is limited to few nm, assumedly due to too many lattice defect sites already present in common graphene oxide, which act as origins for etching. Thus, the formation of larger pores is not possible, since flakes start to disintegrate.^[28,32–35] Accordingly, graphene oxide with extended lattice defects conceptionally can't be considered as a precursor for generating graphene with pores of reasonable lateral dimensions, of tens to hundreds of nm (Table S1, Supporting Information). Here we describe the formation of pores of circular shape by a Mn-species assisted etching procedure at 400 °C in argon atmosphere. The approach starts from oxo-functionalized graphene (oxoG) with a low density of initial vacancy defects (0.8%, as determined by Raman spectroscopy), which is a subclass of the graphene oxide family. By controlling the reaction conditions, it is possible to gain a certain control over the formation of pores with diameters between 100–200 nm in majority. Those pore-graphene materials are highly temperature stable since they are synthesized at 400 °C. Moreover, integration into heterostructures is possible. We report that the amplitude of the photoluminescence (PL) signal of MoS₂ enhances 10-times.

2. Results and Discussion

The formation of pores in monolayers of oxoG was elaborated in a five-step procedure (Figure 1). Accordingly, oxoG flakes are deposited on Si/300 nm SiO₂ wafer by Langmuir–Blodgett technique.^[36–38] The lateral dimensions of monolayer oxoG flakes are roughly 20 μm (Figure 1 left and Figure S2A–C, Supporting Information). Figure S1A,B, Supporting Information, show the results of the statistical Raman analysis of flakes of reduced oxoG revealing an I_D/I_G ratio of the defect induced D band and the G band of 2.7 ± 0.14 and a full-width at half-maximum (Γ) of the 2D band $\Gamma_{2D} = 93 \pm 9 \text{ cm}^{-1}$. Thus, the average distance of defects L_D is about 2 nm, following the relation introduced by Lucchese and Caçado.^[39,40] The distance of defects can be related to a density of defects of about 0.8%.

Then the wafer was immersed into a solution of potassium permanganate (KMnO₄) overnight (for details see experimental part). Metal ions are bound to the surface of the single-layers of oxoG on Si/SiO₂ substrates. A study based on the roughness analysis performed by atomic force microscopy (AFM) was conducted focusing on one specific flake of oxoG before and after KMnO₄ immersion (step 1 in Figure 1) and finally after washing the surface with water (step 2 in Figure 1, see also Figure S2,

Supporting Information). Line height scans indicate that the root mean square roughness of the surface increases from about 0.14 nm to about 0.39 and 0.32 nm, respectively. As we showed before, organosulfate groups with hydronium counter ions explain the thickness of flakes of oxoG.^[41] Here, we propose that hydronium ions are exchanged by Mn-species. Although we realized that step 2, washing the wafer with water to remove possible excess or loosely bound Mn-species is essential for the controlled growth of pores, the AFM height profile remains similar (Figure S2F, Supporting Information) with a roughness of 0.32 nm. After drying the sample at room temperature, the annealing process was carried out in a tube furnace in argon at 400 °C for 12 h. Afterward, the annealed material on the wafer was washed with 1 M hydrochloric acid (HCl) to remove metal or metal oxide particles.^[33] The annealing process induces the disproportionation reaction of oxoG, and we identified in an earlier study that pores can grow by the release of CO₂, while intact graphene patches with diameters of around 3 nm in diameter are generated, as a consequence of mobile oxo-groups on the lattice of graphene.^[42] However, by the here described procedure, graphene with pores (Pr-oxoG_{12h}; index indicated the annealing time) is generated with much larger pores.

By varying the annealing time, graphene materials with pores of different sizes are generated. The formed pores can be visualized by AFM and optical microscopy, respectively. Here, through comparative experiments, we can confirm that manganese plays a very important role in the formation process of pores. For single layers, we suggest that there are small nanoparticles at the edges of pores. Because of the little amount, the content is below the detection limit of, for example, X-ray photoelectron spectroscopy (XPS) or Raman (Mn–O vibrations, Figure S6A, Supporting Information). We further assume that the metal particles move along the edge of the pore to continuously catalyze the pore formation leading to increased diameters of pores. Accordingly, based on this assumption it can be explained why round pores are formed, and thus, the size of the pores can be controlled by etching-time. Figure S3A, Supporting Information, shows an AFM image of single-layer oxoG with no visible pores in the zoomed area depicted in Figure S3B, Supporting Information. As we visualized before by transmission electron microscopy at atomic resolution, oxoG bears only one or few atom vacancies.^[42,43] Figure S3C,D, Supporting Information, show AFM images of Pr-oxoG_{6h}. The presence of small pores is visible in Figure S3D, Supporting Information. To make the comparison reliable, we analyzed the same flake and same area of the flake before and after annealing. Therefore, we conclude that there are small pores of $45 \pm 24 \text{ nm}$ formed in Pr-oxoG_{6h}, as can be observed from Figure S3D and Table S2, Supporting Information.^[30]

Extending the annealing time from 6 to 12 h results in the formation of larger pores (Pr-oxoG_{12h}). Pores in Pr-oxoG_{12h} on Si/SiO₂ substrates are visible under the optical microscope (Figure 2A). As shown in the AFM image of Figure 2B, (the stacked square is visible in the center with higher resolution) there are many pores distributed over the entire flake. An AFM image with a further enlarged area of the flake of Pr-oxoG_{12h} is depicted in Figure 2C. The circular shape of pores with an apparently uniform size of $147 \pm 73 \text{ nm}$ is clearly visible (Table S2, Supporting Information). The height of Pr-oxoG_{12h} is about 1.4 nm, as measured by the AFM tip hitting the underneath surface

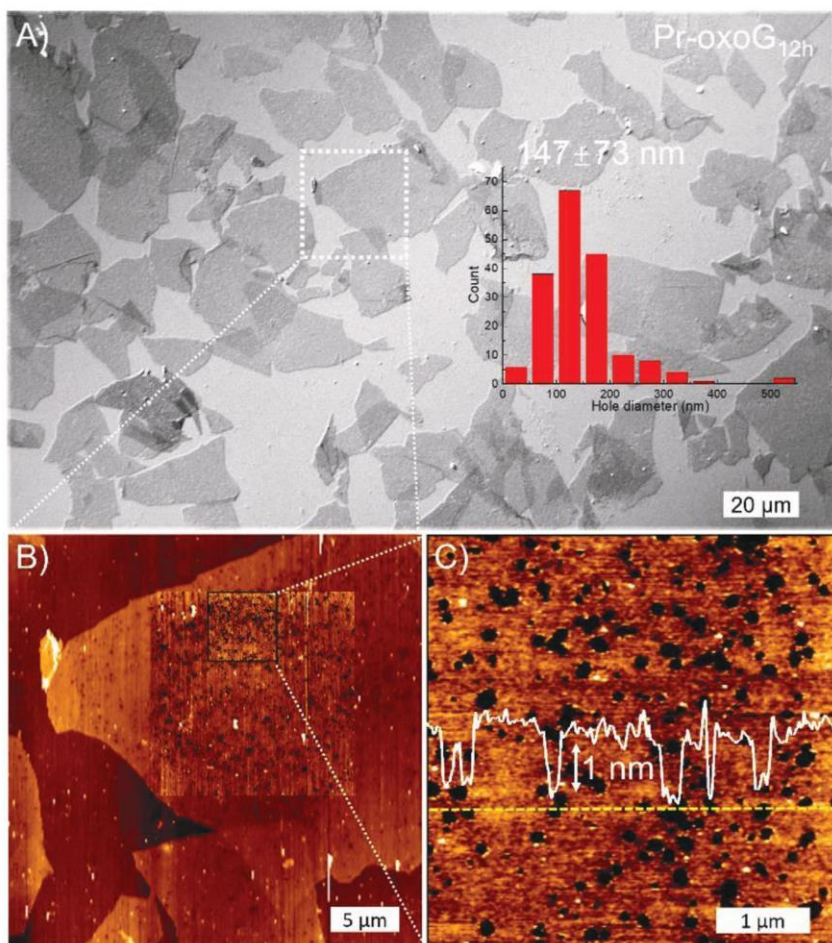


Figure 2. A) Optical microscopy image (differential interference contrast, DIC) of flakes of Pr-oxoG_{12h} on Si/SiO₂ substrates. Inset: histogram shows the size distribution of pores shown in B and C, smaller than 50 nm are not counted. B) AFM topography image of Pr-oxoG_{12h} with overlay of detailed scanned area; C) zoomed AFM topography image of (B) showing pores. White line: height profile, arrow indicates 1 nm.

through the pores. The results of the quantitative analysis of the lateral dimensions of pores in graphene are illustrated in the histogram shown in the inset of Figure 2A. The analysis reveals that the pores diameters are roughly 150 ± 70 nm.

Skipping the final step of HCl washing results in an increased height when measuring through a hole from the SiO₂ surface to the surface of graphene (Figure 3). We assume that a uniform hydration layer may be present between the substrate and graphene. We note that Mn-species, such as nanoparticles, supposed to be located at the rims of pores are not detected by AFM.^[29,33] An analysis of the pore size before and after HCl washing indicates a little increase from 129 ± 75 to 147 ± 72 nm in Figure 3D. Those data are also listed in Table S2, Supporting Information. Next, a reference experiment was performed to eliminate the possibility that similar pores are formed using oxoG without the influence of Mn-species. Thus, flakes of oxoG were annealed for 12 h. As shown in Figure S4, Supporting Information, by optical microscopy and AFM, no

obvious large pores are observed. Therefore, we conclude that annealing alone is not leading to the formation of large pores, starting from oxoG.

To further investigate the effect of annealing time on the pore diameter, we further extended the processing time to 16 h. As shown in Figure S5, Supporting Information, large and merged pores are visible for Pr-oxoG_{16h}, both in the optical microscopy image of Figure S5A, Supporting Information, and AFM images of Figure S5B,C, Supporting Information. As shown in Figure S5B, Supporting Information, there are many pores in the flakes (enlargement in Figure S5C, Supporting Information) and the mean diameter is 168 ± 94 nm. To gain more insights into the mechanism of pore formation process was conducted on few-layers of oxo-G. The AFM images in Figure S6, Supporting Information, reveal some dots in the center of the pore. The thickness of the dots is basically the same as the material height. We suggest that those dots are either trapped etched carbon dots or manganese nanoparticles.

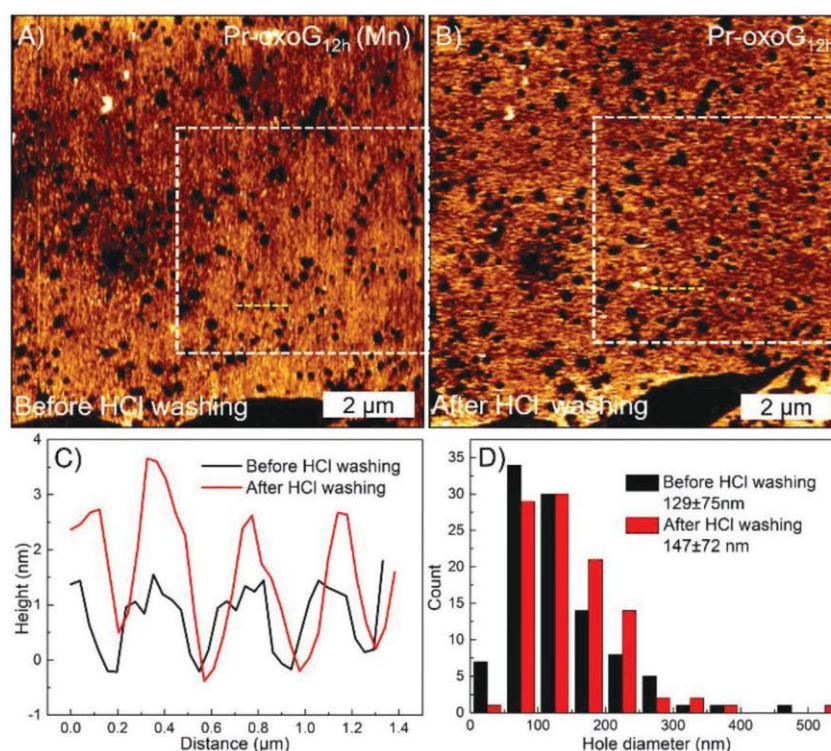


Figure 3. AFM topography images in (A); before (Pr-oxoG_{12h} (Mn)), and B) after (Pr-oxoG_{12h}) HCl washing. C) Height profiles of AFM images along yellow dashed lines. The black and red lines represent the pores height profiles of Pr-oxoG_{12h} (Mn) and Pr-oxoG_{12h}, respectively. D) Distribution of pores in the white box. The black and red bars represent the pores quantity profiles of Pr-oxoG_{12h} (Mn) and Pr-oxoG_{12h}.

Although, evidence is found supporting the hypothesis of the catalytic role of Mn-species such as Mn-atoms or nanoparticles, the final proof is a matter of further research.

A comparison between the different mean diameters and mean pore areas after different annealing time are shown in Figure S7, Supporting Information (data listed in the Table S2, Supporting Information). As the pyrolysis time increases, the average diameter and area of the pores increase according. In the process of growing pores, as shown in Figure 1, we pointed out that skipping washing step 2 with water results in a highly uncontrolled etching process. Compared with Figure 2A, the same annealing time of 12 h was chosen and the AFM image in Figure S8, Supporting Information, shows small pores, very large and also merged pores distributed all over the flakes. We suggest that Mn-species are unevenly distributed on the surface of oxoG if the water washing step is skipped. We note that we observed also partly destroyed and crumpled/folded layers. Therefore, we conclude that washing step 2 is essential to control the generation of pores, and to get some control over the uniformity of grown pores.

Next, an XPS study was conducted to analyze changes in the chemical composition of oxoG and Pr-oxoG_{12h} (Figure 4). All XPS data are listed in Table S3. The high-resolution C 1s spectrum of oxoG in Figure 4A displays a typical saddle-like pattern, which stems from significant oxidation in oxoG.

The content of sp²-C is about 47.8% (due to oxo-groups) and the content of C–O/C–OH/C=O is up to 46.3%. It can be seen from the high-resolution Mn 2p that there is no obvious peak in Figure 4E. Thus, few-layer oxoG contains less than 0.1 at% Mn. Before HCl washing, the high-resolution Mn 2p of Pr-oxoG_{12h} (Mn) reveals also less than 0.1 at% Mn, as shown in Figure 4F. This finding further support that little quantities of Mn-species are catalytically active in the etching process. After annealing, the oxygen content of Pr-oxoG_{12h} is significantly reduced compared to oxoG. As expected, the content of sp²-C increased, here to 50.8%. The high-resolution O 1s spectrum of Pr-oxoG_{12h} displays the peaks of C–O, C=O, O–C=O (Figure 4D). We note that the O 1s peak in Figure 4B is only for reference, since Pr-oxoG_{12h} is not completely covering the Si/SiO₂ substrate and since large pores exist in Pr-oxoG_{12h}. Thus, the influence of the surface O-signal from SiO₂ is affecting the quantitative analysis. The oxygen content is significantly reduced in comparison to oxoG and close to zero if we consider its influence on SiO₂.^[2,44,45] We note, for analyzing the C–O species the C 1s analysis is representative. The analyses of C 1s peaks reveal the formation of C=O and C–O/C–OH groups as a consequence of annealing and the accompanied growth of pores (Figure 4B). Thus, we conclude that the rims of pores are functionalized by carbonyl groups in addition to hydroxyl and carboxyl groups.

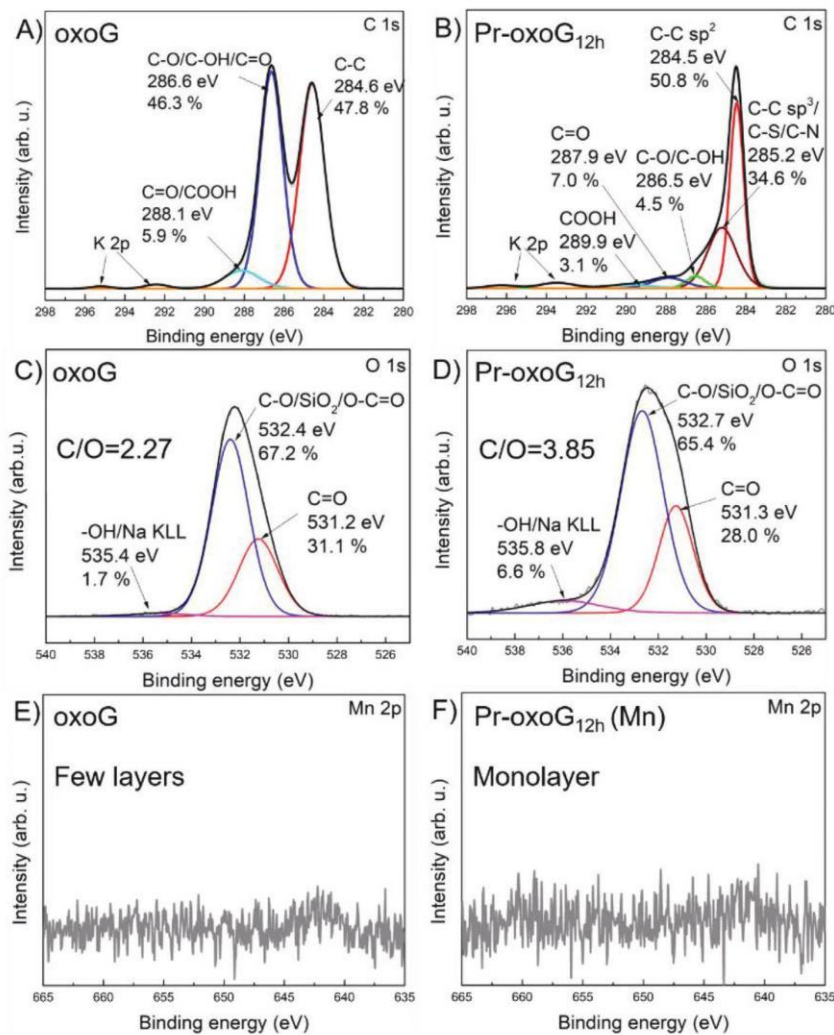


Figure 4. High-resolution C 1s (top) and O 1s (middle) spectra of (A), (C) oxo-G, and (B), (D) Pr-oxoG_{12h}. High-resolution Mn 2p spectra (bottom) of (E) oxo-G and (F) Pr-oxoG_{12h} (Mn).

Moreover, with growing pores into graphene the sp^2 -patches become smaller and consequently, the Raman spectra in Figure S9, Supporting Information, shows, as expected, a broadened D peak with $\Gamma_D = 106 \text{ cm}^{-1}$ for Pr-oxoG_{12h}, compared to $\Gamma_D = 84 \text{ cm}^{-1}$ for oxoG.

In the following, oxoG and Pr-oxoG_{12h}, respectively, are used to fabricate van-der-Waals heterostructures with a single-layer flake of MoS₂ deposited on top (illustrated in Figure 5). Raman spectra (Figure S10, Supporting Information) confirm that the transferred flake of MoS₂ is a monolayer by the measured difference between the out-of-plane A_{1g} mode and the E_{2g} mode of about 19.0 cm^{-1} , as typical for a monolayer.^[46] For the fabrication of the heterostructures, we used a previously described procedure.^[47] Figures 5B,D show optical microscopy images of the realized oxoG/MoS₂ and Pr-oxoG_{12h}/MoS₂ heterostructures,

respectively. The AFM images of the Pr-oxoG_{12h}/MoS₂ heterostructure is depicted in Figure S11A,B, Supporting Information, and proved the expected morphology.

The PL of MoS₂ on SiO₂, on oxoG, on Pr-oxoG_{6h}, and on Pr-oxoG_{12h} are studied next. Figure 5E shows the respective PL of heterostructures. Obviously, the amplitude of the PL is increased for oxoG/MoS₂ and Pr-oxoG_{12h}/MoS₂, using pure MoS₂ on Si/SiO₂ substrate as internal reference, respectively, compared to the PL of the MoS₂ monolayer. The most intense PL is detected for Pr-oxoG_{12h}/MoS₂ with a 10-times increased amplitude. In contrast, the PL of Pr-oxoG_{6h}/MoS₂ is increased 3-times (Figure S12, Supporting Information) and for oxoG/MoS₂ a fourfold increased PL. As depicted in Figure 6 there is a constant PL intensity over the complete flake, without any modulation. A related investigation demonstrated that

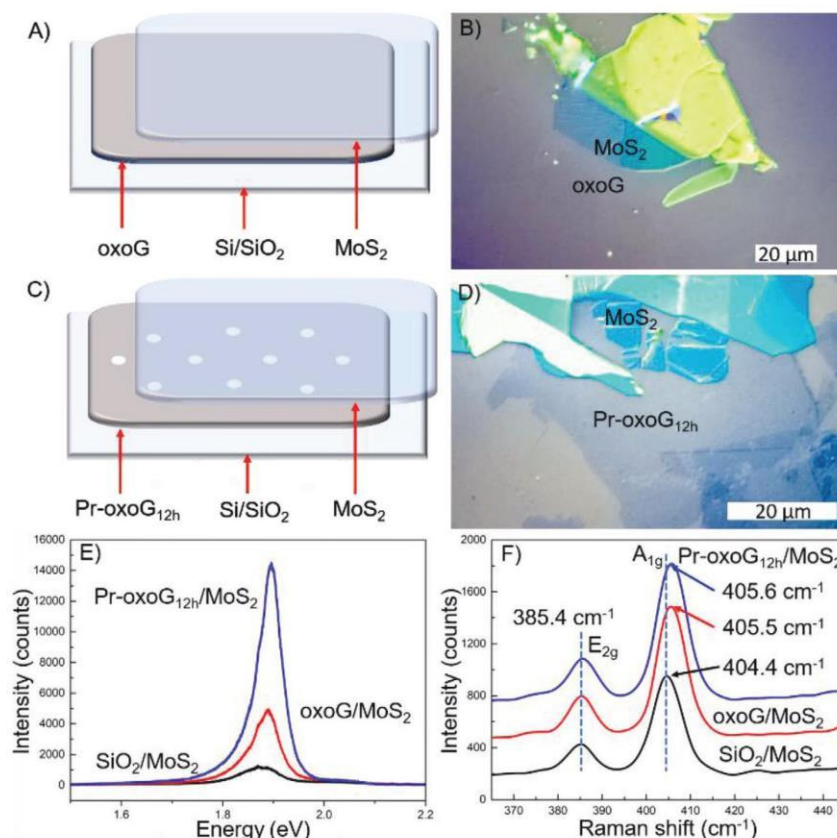


Figure 5. A) Illustration of the heterostructure of oxoG/MoS₂ and B) optical microscopy image of the realized oxoG/MoS₂ heterostructure. C) Illustration of the heterostructure of Pr-oxoG_{12h}/MoS₂ and D) optical microscopy image of the realized Pr-oxoG_{12h}/MoS₂ heterostructure. E) PL spectra of monolayer MoS₂ on SiO₂ (black), oxoG/MoS₂ (red), and Pr-oxoG_{12h}/MoS₂ (blue). F) Raman spectra of the same samples as in (E).

graphene oxide forms a p-type contact with monolayer MoS₂ and this is plausible due to electron-accepting groups detected by XPS, such as carbonyl groups.^[48] Overall, the highest PL enhancement is achieved by using Pr-oxoG_{12h}. Figure 5F shows the Raman spectra of heterostructures detecting the A_{1g} mode of MoS₂ in the heterostructures at around 404.4 cm⁻¹, which is blue-shifted to 405.5 and 405.6 cm⁻¹ for MoS₂ on oxoG and Pr-oxoG_{12h}, respectively, while the position of E_{2g} mode is not shifted. Those observations indicate the p-doping of MoS₂ in the heterostructures by oxoG and Pr-oxoG_{12h}, respectively.^[49,50] Moreover, Pr-oxoG_{12h} reflects a p-doped graphene type material, as indicated by the analysis of the shifts of the G and 2D peak, respectively (Figure S15, Supporting Information). The p-doping effect of Pr-oxoG_{12h} was further investigated by fabricating a heterostructure with a trilayer of MoS₂. Consistent with the expectations, the PL investigation (Figure S13, Supporting Information) indicates less enhancement (trilayer MoS₂ possesses an indirect band-gap), however, a fourfold increased PL is measured, compared to that of a monolayer MoS₂ with a direct band-gap on SiO₂. Thus, the highest, here 10-times increased PL is detected for assembled heterostructure of monolayer Pr-oxoG_{12h}/MoS₂.

In order to exclude the influence of remaining Mn-species on the PL, the PL enhancement of Pr-oxoG_{12h} (Mn) (without HCl washing) was studied by forming the heterostructure of Pr-oxoG_{12h} (Mn)/MoS₂. As shown in Figure S14, Supporting Information, the PL increases, however, only twice, indicating that full enhancement of PL is only achieved after HCl washing and the accompanied removal of particles. Thus, we speculate that Mn-species may form complexes with, for example, carbonyl groups at the rims of pores inhibiting the dramatic PL enhancement, although Raman spectra show the E_{2g} shift to 405.6 cm⁻¹ for Pr-oxoG_{12h} (Mn)/MoS₂. We note that the experimental observations give evidence for a p-doping effect by pore-graphene.

3. Conclusion

Here, we demonstrated the fabrication of graphene with circular pores on the 100 nm scale deposited on Si/SiO₂ surface by annealing of oxo-functionalized and potassium permanganate treated graphene flakes at 400 °C. While excess of Mn-species leads to heterogeneously formed pores and

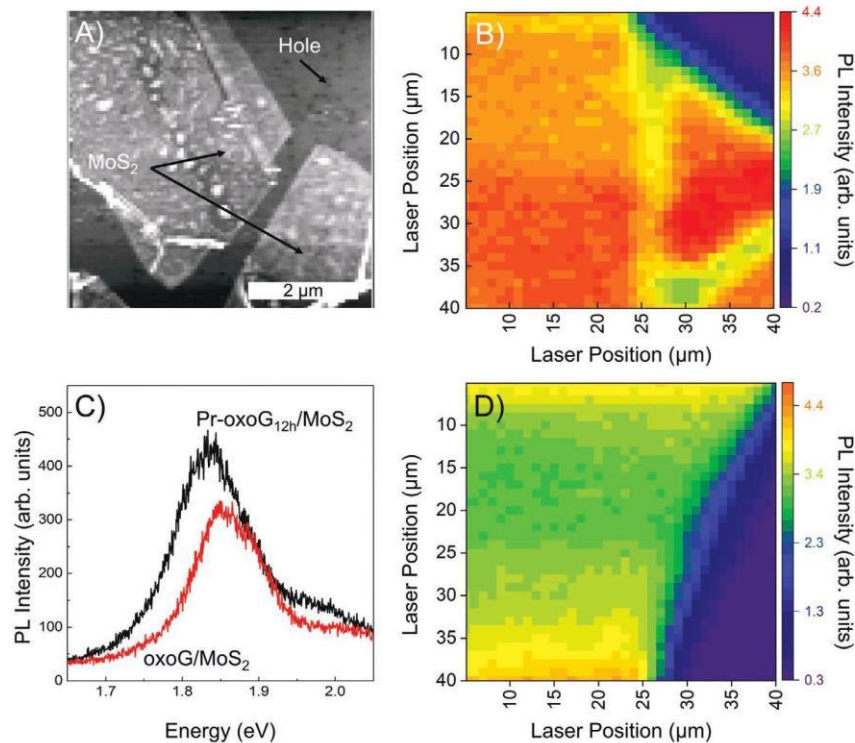


Figure 6. A) Features an AFM map of MoS₂ on top of Pr-oxoG_{12h}. Holes of sizes ranging from 50 nm to 200 nm are visible in the top right of the image and are well separated from one another. The Pr-oxoG_{12h}/MoS₂ PL intensity map (B) shows a constant PL intensity over the MoS₂ flake, exhibiting no sign of a spatial PL modulation that may arise from free-standing MoS₂. C) shows PL spectra from oxo-G/MoS₂ (red) and Pr-oxoG_{12h}/MoS₂ (black), the PL on the Pr-oxoG_{12h} sample exhibiting higher intensity than that seen in the oxo-G/MoS₂ sample. A PL Intensity map of oxo-G/MoS₂ (D) taken with the same parameters as (B) shows a similar constant PL intensity in addition to having slightly lower intensity to that of Pr-oxoG_{12h}/MoS₂.

destroyed flakes, removal of excess potassium permanganate leads to the growth of circular pores with diameters of 50 to 250 nm, depending on the annealing time. Thereby, for example, uniform pores have mean diameters of 147 ± 73 nm after annealing for 12 h. From XPS analysis we conclude that carbonyl, hydroxyl, and carboxyl groups decorate the rims of pores. Since carbonyl groups have electron-accepting properties, it is plausible that the 2D material pore-graphene, can p-dope other 2D materials, such as MoS₂. However, further research, such as correlating field-effect measurements with PL mapping is necessary to further elucidate the mechanism behind PL enhancement by 10-times. Moreover, we showed that Mn-impurities limit the increase of the PL of MoS₂ in the heterostructure with pore-graphene and thus, we propose that the interaction of Mn-species with carbonyl groups may be responsible. Moreover, we conclude that not all defects detected by Raman spectroscopy lead to the growth of pores, taking into account that the initial distance of defects is 2 nm and the final pore-size increased to several hundreds of nm. Finally, we propose that pore-graphene is a 2D material with functional groups at the rims of pores and thus an attractive novel material for sensing applications in the future.

Supporting Information

Supporting Information is available from the Wiley Online Library or from the author.

Acknowledgements

This research is supported by the China Scholarship Council (CSC). C.N. and A.T. acknowledge DFG financial support via the research infrastructure grant INST 275/257-1 FUGG (project no. 313713174), funding through ESF Research Group 2019 FGR 0080 "ESTI" and BMWi project ZF4817401VS9 "TDraCon". P.K. acknowledges DFG for financial support within project no. PP2244.

Open access funding enabled and organized by Projekt DEAL.

Conflict of Interest

The authors declare no conflict of interest.

Data Availability Statement

The data that support the findings of this study are available from the corresponding author upon reasonable request.

Keywords

graphene, graphene oxide, membranes, photoluminescence, porous graphene

Received: May 14, 2021

Revised: June 15, 2021

Published online: August 3, 2021

- [1] C. Neumann, D. Kaiser, M. J. Mohn, M. Fuser, N.-E. Weber, O. Reimer, A. Götzhäuser, T. Weimann, A. Terfort, U. Kaiser, A. Turchanin, *ACS Nano* **2019**, *13*, 7310.
- [2] Z. Wang, Q. Yao, C. Neumann, F. Borner, J. Renner, U. Kaiser, A. Turchanin, H. J. W. Zandvliet, S. Eigler, *Angew. Chem., Int. Ed.* **2020**, *59*, 13657.
- [3] F. Hao, D. Fang, Z. Xu, *Appl. Phys. Lett.* **2011**, *99*, 041901.
- [4] B. Zhan, C. Li, J. Yang, G. Jenkins, W. Huang, X. Dong, *Small* **2014**, *10*, 399.
- [5] D. Akinwande, C. J. Brennan, J. S. Bunch, P. Egberts, J. R. Felts, H. Gao, R. Huang, J.-S. Kim, T. Li, Y. Li, K. M. Liechti, N. Lu, H. S. Park, E. J. Reed, P. Wang, B. I. Yakobson, T. Zhang, Y.-W. Zhang, Y. Zhou, Y. Zhu, *Extreme Mech. Lett.* **2017**, *13*, 42.
- [6] J. Xie, Q. Chen, H. Shen, G. Li, *J. Electrochem. Soc.* **2020**, *167*, 037541.
- [7] K. G. Zhou, K. S. Vasu, C. T. Cherian, M. Neek-Amal, J. C. Zhang, H. Ghorbanfekr-Kalashami, K. Huang, O. P. Marshall, V. G. Kravets, J. Abraham, Y. Su, A. N. Grigorenko, A. Pratt, A. K. Geim, F. M. Peeters, K. S. Novoselov, R. R. Nair, *Nature* **2018**, *559*, 236.
- [8] W. Wu, Y. Shi, G. Liu, X. Fan, Y. Yu, *Desalination* **2020**, *491*, 114452.
- [9] H. Liu, H. Wang, X. Zhang, *Adv. Mater.* **2015**, *27*, 249.
- [10] Q. Xu, H. Xu, J. Chen, Y. Lv, C. Dong, T. S. Sreeprasad, *Inorg. Chem. Front.* **2015**, *2*, 417.
- [11] C. E. Halbig, R. Lasch, J. Krull, A. S. Pirzer, Z. Wang, J. N. Kirchoff, K. I. Bolotin, M. R. Heinrich, S. Eigler, *Angew. Chem., Int. Ed.* **2019**, *58*, 3599.
- [12] A. Criado, M. Melchionna, S. Marchesan, M. Prato, *Angew. Chem., Int. Ed.* **2015**, *54*, 10734.
- [13] S. Chen, J. Duan, M. Jaroniec, S. Z. Qiao, *J. Mater. Chem. A* **2013**, *1*, 9409.
- [14] A. C. Lokhande, I. A. Qattan, C. D. Lokhande, S. P. Patole, *J. Mater. Chem. A* **2020**, *8*, 918.
- [15] Y. Zhang, Q. Wan, N. Yang, *Small* **2019**, *15*, 1903780.
- [16] A. Guirguis, J. W. Maina, L. Kong, L. C. Henderson, A. Rana, L. H. Li, M. Majumder, L. F. Dumée, *Carbon* **2019**, *155*, 660.
- [17] X. Yang, C. Cheng, Y. Wang, L. Qiu, D. Li, *Science* **2013**, *341*, 534.
- [18] S. Han, D. Wu, S. Li, F. Zhang, X. Feng, *Adv. Mater.* **2014**, *26*, 849.
- [19] H. Yang, Q. He, Y. Liu, H. Li, H. Zhang, T. Zhai, *Chem. Soc. Rev.* **2020**, *49*, 2916.
- [20] C. J. Russo, J. A. Golovchenko, *Proc. Natl. Acad. Sci. USA* **2012**, *109*, 5953.
- [21] S. Standop, O. Lehtinen, C. Herbig, G. Lewes-Malandrakis, F. Craes, J. Kotakoski, T. Michely, A. V. Krasheninnikov, C. Busse, *Nano Lett.* **2013**, *13*, 1948.
- [22] A. Guirguis, J. W. Maina, X. Zhang, L. C. Henderson, L. Kong, H. Shon, L. F. Dumée, *Mater. Horiz.* **2020**, *7*, 1218.
- [23] N. I. Kato, *J. Electron Microsc.* **2004**, *53*, 451.
- [24] Y. Lin, Y. Liao, Z. Chen, J. W. Connell, *Mater. Res. Lett.* **2017**, *5*, 209.
- [25] S. P. Surwade, S. N. Smirnov, I. V. Vlassiok, R. R. Unocic, G. M. Veith, S. Dai, S. M. Mahurin, *Nat. Nanotechnol.* **2015**, *10*, 459.
- [26] T. He, Z. Wang, F. Zhong, H. Fang, P. Wang, W. Hu, *Adv. Mater. Technol.* **2019**, *4*, 1900064.
- [27] A. Kaplan, Z. Yuan, J. D. Benck, A. Govind Rajan, X. S. Chu, Q. H. Wang, M. S. Strano, *Chem. Soc. Rev.* **2017**, *46*, 4530.
- [28] X. Wang, L. Jiao, K. Sheng, C. Li, L. Dai, G. Shi, *Sci. Rep.* **2013**, *3*, 1996.
- [29] H. Zhang, W. Liu, Z. Zhang, M. Li, B. Xu, J. Guo, *Phys. Chem. Chem. Phys.* **2018**, *20*, 26814.
- [30] S. C. O'Hern, M. S. Boutilier, J. C. Idrobo, Y. Song, J. Kong, T. Laoui, M. Atieh, R. Karnik, *Nano Lett.* **2014**, *14*, 1234.
- [31] L. Huang, M. Zhang, C. Li, G. Shi, *J. Phys. Chem. Lett.* **2015**, *6*, 2806.
- [32] H.-K. Kim, S.-M. Bak, S. W. Lee, M.-S. Kim, B. Park, S. C. Lee, Y. J. Choi, S. C. Jun, J. T. Han, K.-W. Nam, K. Y. Chung, J. Wang, J. Zhou, X.-Q. Yang, K. C. Roh, K.-B. Kim, *Energy Environ. Sci.* **2016**, *9*, 1270.
- [33] D. Zhou, Y. Cui, P. W. Xiao, M. Y. Jiang, B. H. Han, *Nat. Commun.* **2014**, *5*, 4716.
- [34] Z. Fan, Q. Zhao, T. Li, J. Yan, Y. Ren, J. Feng, T. Wei, *Carbon* **2012**, *50*, 1699.
- [35] Y. Xu, C.-Y. Chen, Z. Zhao, Z. Lin, C. Lee, X. Xu, C. Wang, Y. Huang, M. I. Shaker, X. Duan, *Nano Lett.* **2015**, *15*, 4605.
- [36] S. Eigler, *Phys. Chem. Chem. Phys.* **2014**, *16*, 19832.
- [37] S. Eigler, M. Enzelberger-Heim, S. Grimm, P. Hofmann, W. Kroener, A. Geworski, C. Dotzer, M. Rockert, J. Xiao, C. Papp, O. Lytken, H. P. Steinruck, P. Müller, A. Hirsch, *Adv. Mater.* **2013**, *25*, 3583.
- [38] S. Eigler, F. Hof, M. Enzelberger-Heim, S. Grimm, P. Müller, A. Hirsch, *J. Phys. Chem. C* **2014**, *118*, 7698.
- [39] M. M. Lucchese, F. Stavale, E. H. M. Ferreira, C. Vilani, M. V. O. Moutinho, R. B. Capaz, C. A. Achete, A. Jorio, *Carbon* **2010**, *48*, 1592.
- [40] L. G. Cancado, A. Jorio, E. H. Ferreira, F. Stavale, C. A. Achete, R. B. Capaz, M. V. Moutinho, A. Lombardo, T. S. Kulmala, A. C. Ferrari, *Nano Lett.* **2011**, *11*, 3190.
- [41] S. Eigler, C. Dotzer, F. Hof, W. Bauer, A. Hirsch, *Chem. - Eur. J.* **2013**, *19*, 9490.
- [42] F. Grote, C. Gruber, F. Borner, U. Kaiser, S. Eigler, *Angew. Chem., Int. Ed.* **2017**, *56*, 9222.
- [43] P. Feicht, J. Biskupek, T. E. Gorelik, J. Renner, C. E. Halbig, M. Maranska, F. Puchtler, U. Kaiser, S. Eigler, *Chem. - Eur. J.* **2019**, *25*, 8955.
- [44] M. González, J. Baselga, J. Pozuelo, *J. Mater. Chem. C* **2016**, *4*, 8575.
- [45] K. Garg, R. Shanmugam, P. C. Ramamurthy, *Opt. Mater.* **2018**, *76*, 42.
- [46] C. Lee, H. Yan, L. E. Brus, T. F. Heinz, J. Hone, S. Ryu, *ACS Nano* **2010**, *4*, 2695.
- [47] Z. Wang, Q. Yao, Y. Hu, C. Li, M. Hußmann, B. Weintrub, J. N. Kirchoff, K. Bolotin, T. Taniguchi, K. Watanabe, S. Eigler, *RSC Adv.* **2019**, *9*, 38011.
- [48] T. Musso, P. V. Kumar, A. S. Foster, J. C. Grossman, *ACS Nano* **2014**, *8*, 11432.
- [49] X. Wei, Z. Yu, F. Hu, Y. Cheng, L. Yu, X. Wang, M. Xiao, J. Wang, X. Wang, Y. Shi, *AIP Adv.* **2014**, *4*, 123004.
- [50] W. Zhang, J.-K. Huang, C.-H. Chen, Y.-H. Chang, Y.-J. Cheng, L.-J. Li, *Adv. Mater.* **2013**, *25*, 3456.

**ADVANCED
MATERIALS
INTERFACES**

Supporting Information

for *Adv. Mater. Interfaces*, DOI: 10.1002/admi.202100783

Synthesis of Wet-Chemically Prepared Porous-
Graphene Single Layers on Si/SiO₂ Substrate Increasing
the Photoluminescence of MoS₂ in Heterostructures

*Yiqing Wang, Christof Neumann, Marleen Hußmann,
Qing Cao, Yalei Hu, Oisín Garrity, Patryk Kusch, Andrey
Turchanin, and Siegfried Eigler**

Supporting Information

Synthesis of p-doped porous-graphene single layers on Si/SiO₂ substrate increasing the photoluminescence of MoS₂ in heterostructures

Yiqing Wang, Christof Neumann Marleen Hußmann, Qing Cao, Yalei Hu, Oisín Garrity, Patryk Kusch, Andrey Turchanin, Siegfried Eigler

Experimental Section

Materials and Methods

Double-distilled water from Carl Roth GmbH. Graphite (3061) was obtained from Asbury Carbon. Si wafers with a 300 nm thick SiO₂ layer were purchased from Fraunhofer Institut für Integrierte Systeme und Bauelementetechnologie IISB in Erlangen. Chemicals were purchased from Sigma-Aldrich. A Nikon Eclipse LV150-NL with differential interference contrast was used to visualize materials. Statistical Raman spectroscopy (SRS) was recorded using a Horiba Explora spectrometer with a 532 nm laser for excitation combined with 100x magnification objective. Increment of Raman spectra measurements is 0.7 μm . PL map parameters for Figure 6: The steps between two recorded spectra was 250 nm, with a laser spot size of around 400 nm. As excitation we use a 532 nm laser and kept the laser power below 0.5 mW to avoid sample heating. As a reference, we record a PL map with the same experimental parameters for a sample without holes.

For preparation of Langmuir-Blodgett films, we used a Kibron μ Thru system with water as subphase. The surface tension of water = 72.8 mN m^{-1} was set to zero. The films were formed at a surface tension value of 3 mN m^{-1} . AFM images were recorded on an JPK Nanowizard 4 equipped with NSG10/Au probes and intermittent contact mode was chosen. Using Tap300-G AFM Probe. X-ray photoelectron spectroscopy (XPS) was performed using a multiprobe system (Scienta Omicron) with a monochromatic X-ray source (Al K α) and an electron analyzer (Argus CU) with 0.6 eV spectral energy resolution. The spectra were fitted using Voigt functions (30:70) after Shirley background subtraction. The Si 2p peak (SiO₂, 103.5 eV) was used for binding energy calibration. Putting the entire substrate with monolayer flakes in the XPS instrument.

Synthesis of Oxo-Functionalized Graphene (oxoG)

OxoG was prepared by low-temperature oxidation of graphite according to our previously developed method^[1, 2]. Accordingly, 2 g of graphite (type 3061, Asbury Carbon Mills) were mixed with 50 mL of sulfuric acid (97.5%) in a Teflon reactor under mechanical stirring at a temperature below 10 °C. After that, 4 g of KMnO₄ were slowly added within 4 h and further stirred for 16 h. Then, 40 mL of cold diluted sulfuric acid (20 wt%) and followed by 100 mL of cold double distilled water were slowly continuously added through a programmed pump within 4 h and 16 h, respectively. Then, 40 mL of H₂O₂ (5 wt%) were added into the reaction mixture to solubilize manganese species. Then, the dispersion was washed with cold double

distilled water by repeated centrifugation and redispersion in double distilled water for six times.

Formation of films of flakes of oxoG on Si/SiO₂ wafer:

Flakes of oxoG were deposited on a Si/300 nm SiO₂ wafer by Langmuir Blodgett technique. First, a light yellowish oxoG dispersion was prepared by dilution of water/methanol, 1/2 by volume (the exact concentration was found to have only little influence on the quality of the formed film of flakes). The dispersion was dropped on the water-interface of the Langmuir-Blodgett trough and the barriers were compressed until a surface tension of 3 mN/m was reached.

Reduction of flakes of oxoG on Si/SiO₂ wafer (Preparation of red-oxoG).

Wafers with deposited flakes of oxoG were placed in a 20 mL glass vial filled with glass wool and were reduced by the vapor of HI and TFA for 10 min at 80 °C. Subsequently, the wafers were extensively washed with pure water and dried.

Preparation of Pr-oxoG.

Pr-oxoG was prepared by using potassium permanganate (KMnO₄) as the etching agents. Flakes of oxoG on a Si/SiO₂ wafer were immersed in aqueous KMnO₄ solution (0.2 mmol). The oxoG flakes on Si/SiO₂ the wafer was washed with water and dried in the air. Then, the wafer was heated in argon atmosphere at a rate of 10 °C min⁻¹ to 400 °C for 6 h, 12 h and 16 h, respectively and cooled down to room temperature.

Preparation of tp-oxoG.

The oxoG flakes on Si/SiO₂ mixture were dried in the air and then heated at a rate of 10 °C min⁻¹ to 400 °C for 12 h in an atmosphere of Argon and cooled down to room temperature.

Removal of metal containing species.

Annealed wafers were immersed in aqueous HCl solution (1 M) for two days to remove the metal-containing species. Then, wafers were shaken gently in double distilled water to wash off acids. Finally, Pr-oxoG on Si/300 nm SiO₂ wafers is obtained. As reference tp-oxoG was obtained the same way, however without KMnO₄ treatment.

Pore diameter and area analysis

Pore diameters were estimated manually by using the straight line tool in ImageJ. After counting the pores, export the results of the pore diameter and area.^[3]

Table S1. Survey of perforation techniques, with indicated starting material, layer thickness, etching process, realized pore size and targeted application.

Raw material	Thickness	Perforation technique	Pore size (nm)	application	Ref.
Graphene	Few layers	Oxygen plasma, ozone	<5	permeance membranes	[4]
Graphene	Few layers	Focused ions beam (SEM)	<50	-	[5]
Graphene	Monolayer	Bottom-up synthesis	0-250	Charge Transport	[6]
GO	-	Chemical-oxidative etching (KMnO ₄), microwave irradiation.	2-4	supercapacitor	[7]
GO	-	Chemical-oxidative etching (HNO ₃)	60-90	Catalyst (Bulk)	[8]
GO	-	Chemical-oxidative etching (H ₂ O ₂)	2-70	supercapacitor	[9]
Graphene	Few layers	Liquid arc discharge, Ni atoms	10-50	-	[10]
Graphene	Monolayer	Strain-assisted treatment, Pt nanoparticles etching	<50	Charge Transport	Carrier [11]
RGO	Few layers	Annealing treatment, nanoparticles etching	Pt <50	-	[11]
GO	Bulk	Annealing treatment, etching	Fe ₂ O ₃ -	electrocatalyst	[12]
RGO	Bulk	Carbothermal reaction by using the metal oxide nanoparticles (Oxometalates)	5-10, 20-50	-	[13]
Oxo-functionalized graphene	Monolayer	Disproportionation functionalization of 4%	1-3	-	[2]
Oxo-functionalized graphene	Monolayer	Disproportionation, functionalization of 60%	5	Charge Transport	Carrier [14]

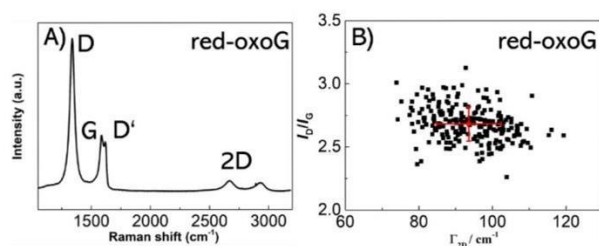


Figure S1. Statistical Raman analysis of chemically reduced oxoG (Statistical Raman microscopy measured at 532 nm laser excitation wavelength. The laser power is below 0.1 mW to avoid heating induced by laser). A) Average spectrum of reduced oxoG with $I_{D'}/I_G$ ratio of 2.7 ± 0.14 and $\Gamma_{2D} = 93 \pm 9 \text{ cm}^{-1}$. B) Scatter plot of ID/IG vs FWHM of the 2D peak.

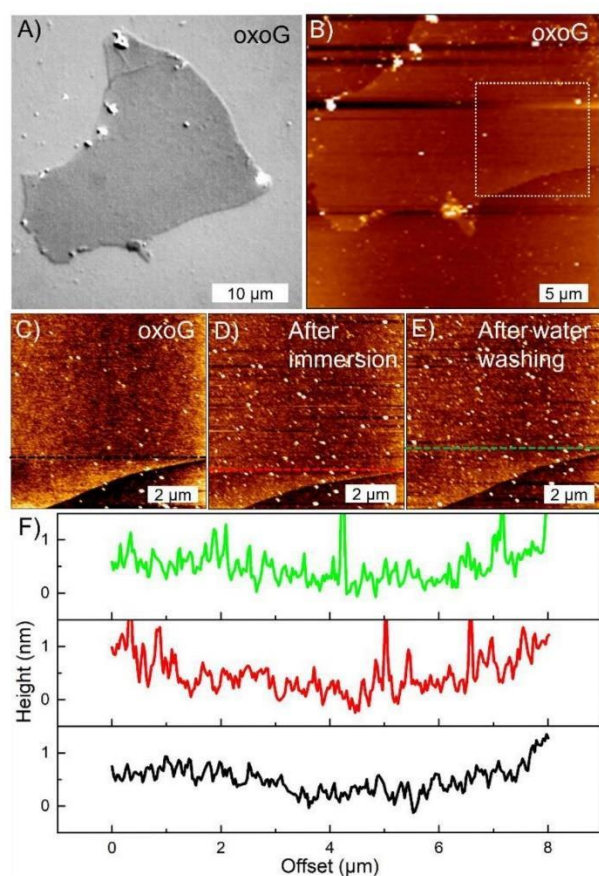


Figure S2. A) Optical microscope images of flakes of oxoG on Si/300 nm SiO₂ wafer and AFM topography images in B and C; before, D) after immersion in KMnO₄ solution and E) after washing in water. F) Height profiles of AFM images along black, red and green lines. The black, red and green line represent the height profiles of oxoG, oxoG after immersion and oxoG after washing with water, respectively.

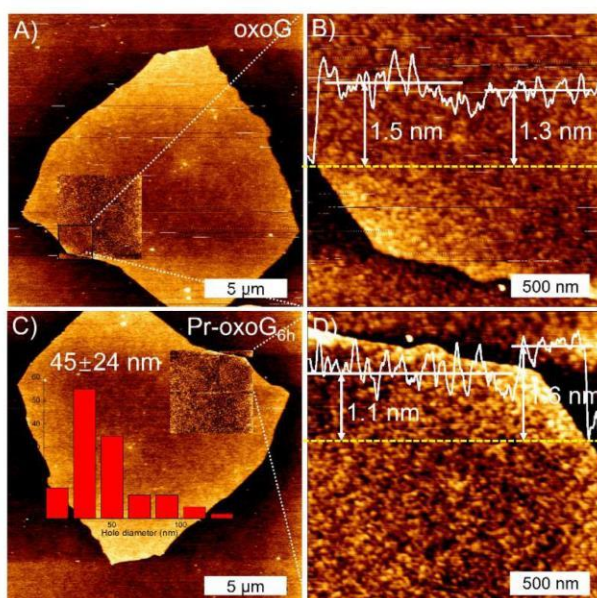


Figure S3. A and B) AFM topography images of single layer oxoG, showing no big pores. C and D) AFM images of Pr-oxoG_{6h}. The yellow lines represent the height profiles of oxoG and Pr-oxoG_{6h}, respectively.

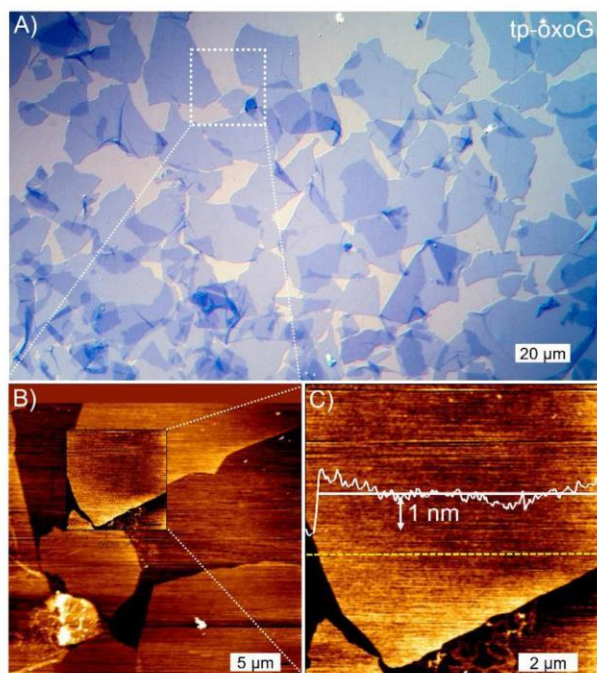


Figure S4. A) Optical microscope image of flakes of tp-oxoG on Si/300 nm SiO₂ substrate. B) AFM topography image of tp-oxoG (12 h annealing time). C) Figure S3B shows no big pores after annealing single layer oxoG for 12 h without Mn-species. The yellow line represents the height profile of tp-oxoG.

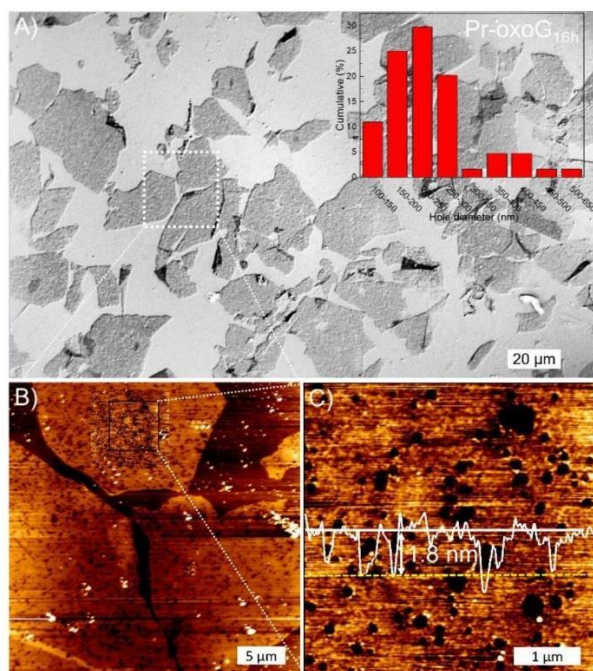


Figure S5. A) Optical microscope image of flakes of Pr-oxoG_{16h} on Si/300 nm SiO₂ substrate; B) AFM topography image of Pr-oxoG_{16h}. C) AFM image showing pores. The yellow line represents the height profile of Pr-oxoG_{16h}.

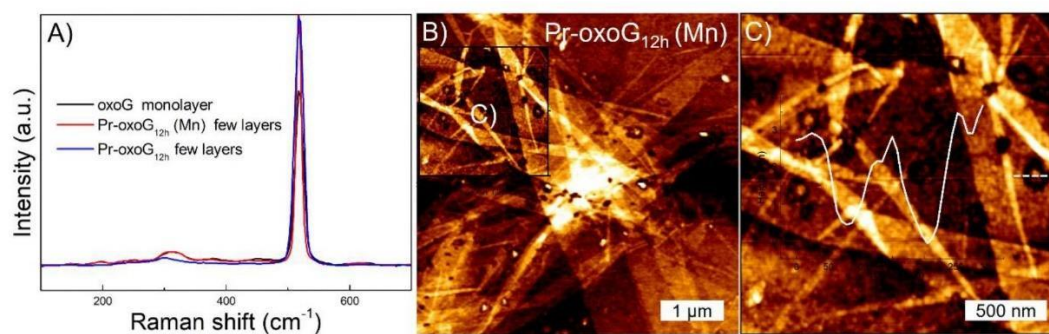
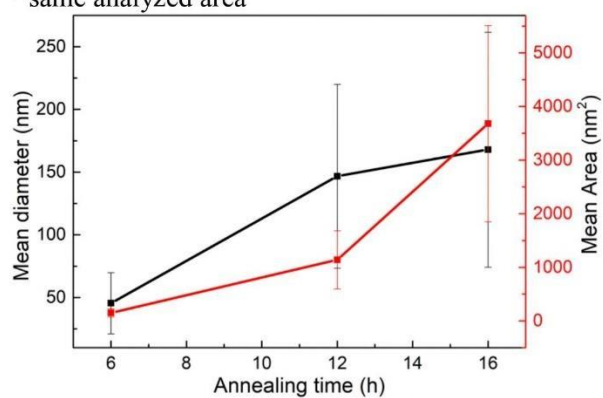


Figure S6. A) Raman spectrum of monolayer oxoG, few-layer Pr-oxoG_{12h} (Mn) and few-layer Pr-oxoG_{12h} on Si/300 nm SiO₂ substrate; B, C) AFM topography image of few-layer Pr-oxoG_{12h} (Mn). The white line represents the height profile of few-layer Pr-oxoG_{12h} (Mn).

Table S2. Number total of pores, mean (average), standard deviation, minimum, Median and maximum of diameter of pores.

	Number total	Mean (diameter)	Standard Deviation	Sum	Minimum	Median	Maximum
Pr-oxoG _{6h}	126	45.45256	24.35966	5727.022	9.298	37.749	127.104
Pr-oxoG _{12h}	181	146.74168	73.25105	26560.244	37.771	133.539	503.704
Pr-oxoG _{16h}	104	167.95725	93.74814	17635.511	40.323	153.438	620.968
Pr-oxoG _{12h} (Mn)*	101	128.59717	74.66974	12988.314	26.845	108.216	457.154
Pr-oxoG _{12h} *	101	146.98062	72.06714	14845.043	48.65	138.462	523.981
	Number total	Mean (Area)	Standard Deviation	Sum	Minimum	Median	Maximum
Pr-oxoG _{6h}	126	149.94286	75.35488	18892.8	38.42	124.863	403.405
Pr-oxoG _{12h}	181	1138.8772	542.72571	206136.774	329.218	1042.524	3786.008
Pr-oxoG _{16h}	105	3680.27461	1830.97899	386428.834	1144.409	3433.228	12588.501
Pr-oxoG _{12h} (Mn)*	101	1903.31623	1003.89167	192234.939	540.492	1621.476	6305.738
Pr-oxoG _{12h} *	101	2502.78283	1099.68609	252781.066	1183.432	2366.864	8284.024

* same analyzed area

**Figure S7.** A comparison between the different mean diameters and mean pores areas after different annealing time.

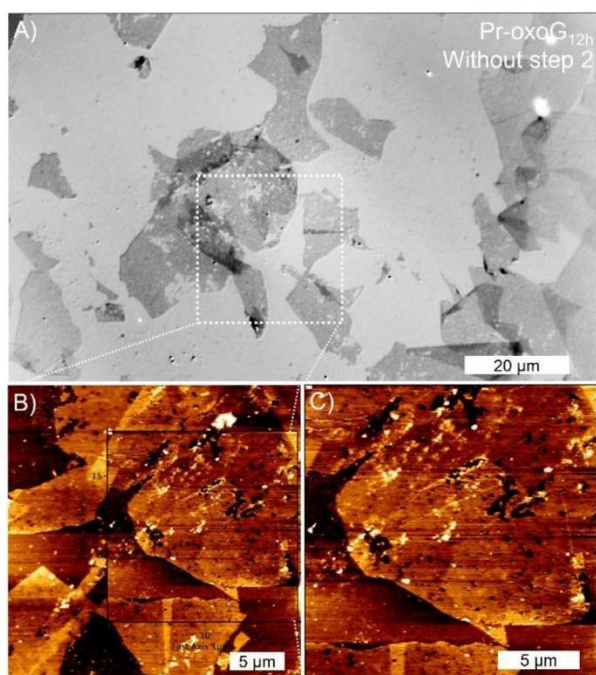


Figure S8. A) Optical microscope image of flakes of Pr-oxoG_{12h} on Si/SiO₂ substrate without water washing step 2; B) AFM topography image of flakes of Pr-oxoG_{12h} on Si/SiO₂ substrate without water washing step 2.

Table S3. Quantitative analysis of the high resolution XP C 1s and O 1s spectra presented in Figure 3A and B of the main text including peak assignment, binding energies and areas obtained from the spectra deconvolution.

sample	Peak assignment	Binding energy, eV	Area, %	
oxoG	C-C /C-H	284.6	47.8	
	C 1s	C-O/C-OH/C=O	286.6	46.3
		C=O/COOH	288.1	5.9
		C=O	531.2	31.1
	O 1s	C-O/SiO ₂ /O-C=O	532.4	67.2
		-OH/Na KLL	535.4	1.7
C-C sp ²		284.5	50.8	
Pr-oxoG _{12h}	C-C sp ³ / C-S/C-N	285.2	34.6	
	C 1s	C-O/C-OH	286.5	4.5
		C=O	287.9	7.0
		COOH	289.9	3.1
		C=O	531.3	28.0
	O 1s	C-O/SiO ₂ /O-C=O	532.7	65.4
		-OH/Na KLL	535.8	6.6

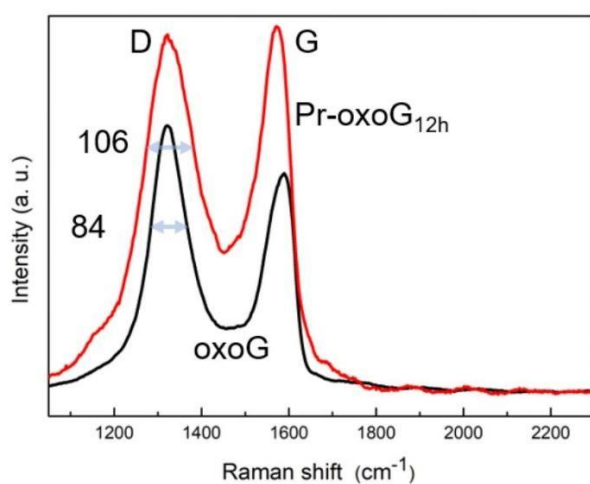


Figure S9. Raman spectrum of oxoG, and Pr-oxoG_{12h}. Numbers indicate the full-width at half-maximum of the D band.

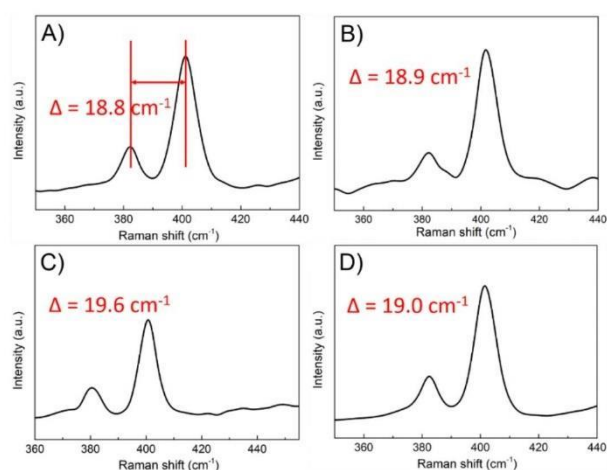


Figure S10. Raman spectrum of monolayer MoS₂ for A) MoS₂ on SiO₂, B) Pr-oxoG_{6h}/MoS₂, C) Pr-oxoG_{12h}/MoS₂ and D) Pr-oxoG_{12h}/MoS₂ (Mn) heterostructure.

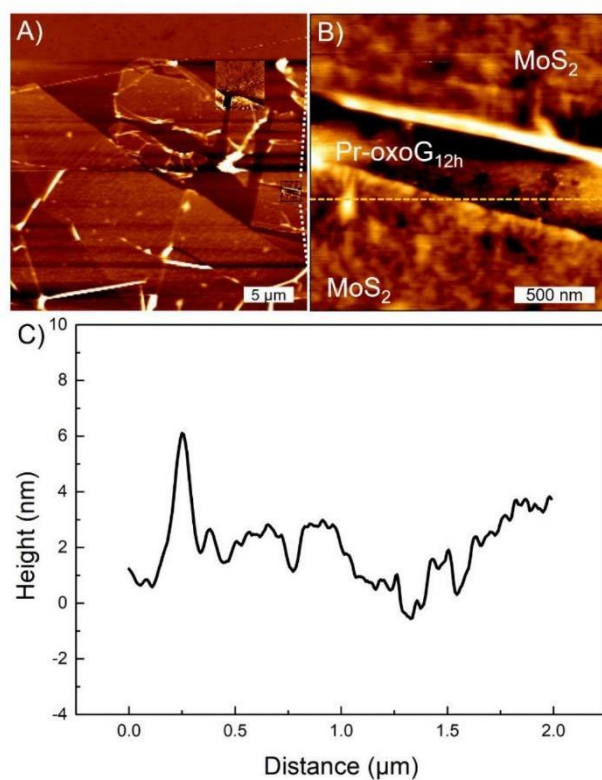


Figure S11. A and B) AFM topography images of monolayer Pr-oxoG_{12h}/MoS₂ heterostructure. C) The white line represents the height of Pr-oxoG_{12h}/MoS₂ heterostructure. MoS₂ and Pr-oxoG_{12h} almost have same thickness.

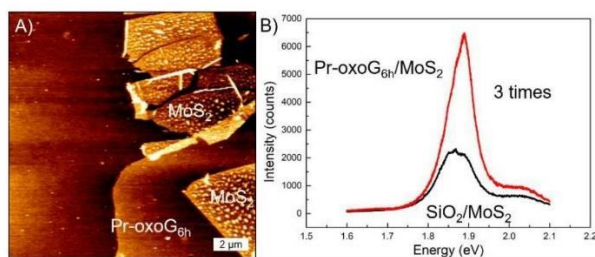


Figure S12. A) AFM topography images of monolayer Pr-oxoG_{6h}/MoS₂ heterostructure; B) PL spectra of monolayer MoS₂ on SiO₂ (black) and monolayer Pr-oxoG_{6h}/MoS₂ heterostructure (red), respectively.

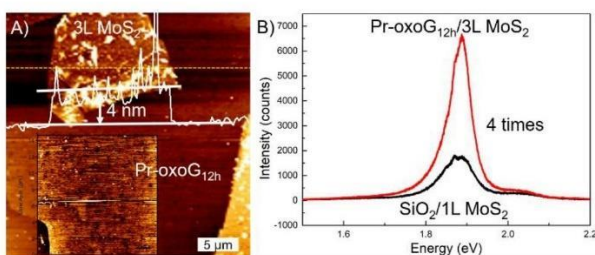


Figure S13. A) AFM topography images of trilayer Pr-oxoG_{12h}/MoS₂ heterostructure. The height of 3L MoS₂ is almost 4 nm. B) PL spectra of monolayer MoS₂ on SiO₂ and trilayer Pr-oxoG_{12h}/MoS₂ heterostructure.

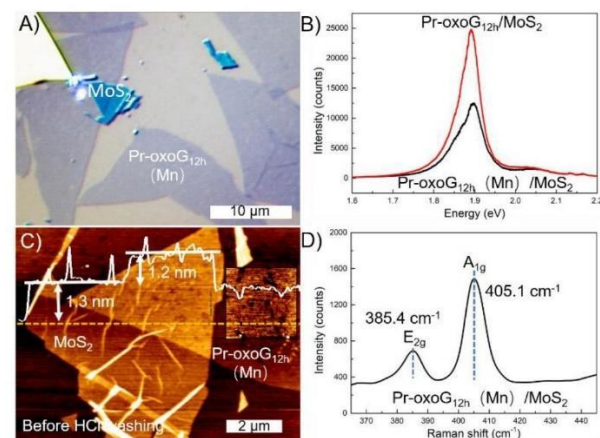


Figure S14. A) Optical microscope image of a monolayer Pr-oxoG_{12h} (Mn)/MoS₂ heterostructure; B) PL spectra of a monolayer Pr-oxoG_{12h}/MoS₂ heterostructure and a monolayer Pr-oxoG_{12h} (Mn)/MoS₂ heterostructure. C) AFM topography image of Pr-oxoG_{12h} (Mn)/MoS₂ heterostructure. The white line represents the height profile along yellow line. D) Raman spectra of Pr-oxoG_{12h} (Mn)/MoS₂.

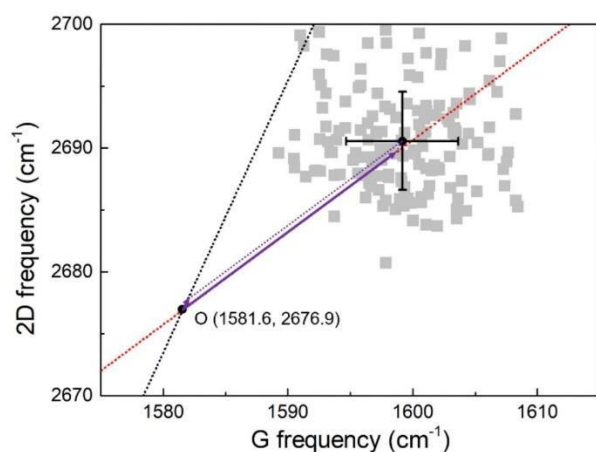


Figure S15. The grey dots were obtained from Raman mapping of Pr-oxoG_{12h}. The black dot (1581.6, 2676.9 cm⁻¹) stems from reference^[15] and the position relates to graphene, which is not affected by charge or strain doping. The red dashed line represent doped graphene with varying density of holes with a slope is 0.75. The black dashed line represents charge-neutral graphene under randomly oriented uniaxial stress with a slope of 2.20. The purple solid line is the effects corresponding to the hole doping and strain decomposed by the vector model.

References

- [1] S. Eigler, M. Enzelberger-Heim, S. Grimm, P. Hofmann, W. Kroener, A. Geworski, C. Dotzer, M. Rockert, J. Xiao, C. Papp, O. Lytken, H. P. Steinruck, P. Müller, A. Hirsch, *Adv. Mater.* **2013**, *25*, 3583.
- [2] F. Grote, C. Gruber, F. Börrnert, U. Kaiser, S. Eigler, *Angew. Chem. Int. Ed.* **2017**, *56*, 9222.
- [3] S. C. O'Hern, M. S. Boutilier, J. C. Idrobo, Y. Song, J. Kong, T. Laoui, M. Atieh, R. Karnik, *Nano Lett.* **2014**, *14*, 1234.
- [4] G. He, S. Huang, L. F. Villalobos, J. Zhao, M. Mensi, E. Oveisi, M. Rezaei, K. V. Agrawal, *Energy Environ. Sci.* **2019**, *12*, 3305.
- [5] S. Standop, O. Lehtinen, C. Herbig, G. Lewes-Malandrakis, F. Craes, J. Kotakoski, T. Michely, A. V. Krasheninnikov, C. Busse, *Nano Lett.* **2013**, *13*, 1948.
- [6] C. Neumann, D. Kaiser, M. J. Mohn, M. Fuser, N.-E. Weber, O. Reimer, A. Götzhäuser, T. Weimann, A. Terfort, U. Kaiser, A. Turchanin, *ACS Nano* **2019**, *13*, 7310.
- [7] Z. Fan, Q. Zhao, T. Li, J. Yan, Y. Ren, J. Feng, T. Wei, *Carbon* **2012**, *50*, 1699.
- [8] X. Wang, L. Jiao, K. Sheng, C. Li, L. Dai, G. Shi, *Sci. Rep.* **2013**, *3*, 1996.
- [9] Y. Xu, C.-Y. Chen, Z. Zhao, Z. Lin, C. Lee, X. Xu, C. Wang, Y. Huang, M. I. Shakir, X. Duan, *Nano Lett.* **2015**, *15*, 4605.
- [10] H. Zhang, W. Liu, Z. Zhang, M. Li, B. Xu, J. Guo, *Phys. Chem. Chem. Phys.* **2018**, *20*, 26814.
- [11] X. Liao, B. Zhang, T. Furutani, Y. Chen, H. Xiao, Y. Ni, A. Yonezu, X. Chen, *Small* **2019**, *15*, e1903213.
- [12] T. Palaniselvam, H. B. Aiyappa, S. Kurungot, *J. Mater. Chem.* **2012**, *22*, 23799.
- [13] D. Zhou, Y. Cui, P. W. Xiao, M. Y. Jiang, B. H. Han, *Nat. Commun.* **2014**, *5*, 4716.
- [14] Z. Wang, Q. Yao, C. Neumann, F. Börrnert, J. Renner, U. Kaiser, A. Turchanin, H. J. W. Zandvliet, S. Eigler, *Angew. Chem. Int. Ed.* **2020**, *59*, 13657.
- [15] J. E. Lee, G. Ahn, J. Shim, Y. S. Lee, S. Ryu, *Nat. Commun.* **2012**, *3*, 1024.

5.2 Regiochemically oxo-functionalized graphene, guided by defect sites, as catalyst for oxygen reduction to hydrogen peroxide.

So far, graphene oxide can be prepared by various methods, such as Hummers and Tour methods.²¹ The graphene oxide obtained by these common methods contains many oxygen functional groups and lattice defects.^{114, 115} Graphene oxide has about 50% sp²-C atoms and defects. Its O content reaches 40%. The presence of many oxygen functional groups reduces its electrical conductivity, and graphene oxide is not suitable for electrocatalytic materials.¹¹⁶ However, it has been reported that the oxygen functional group located on the base surface or edge of carbon can be used as an active site to improve the activity and selectivity of the electrocatalytic oxygen reduction to produce hydrogen peroxide.^{79, 117} This report contradicts the specificity of the oxygen function. Therefore, it is essential to construct the definite structure of graphene oxide and further study the relationship between properties and structure.¹¹⁸

I use oxoG, a graphene oxide derivative with a definite carbon lattice, as a model.^{23, 24} The oxygen functional groups of oxoG can be removed and introduced by electrochemical reduction (ERoxoG) and reoxidation (ERoxoG-O) respectively. Statistical Raman analyzes the samples obtained by electrochemical methods. I found that vacancy defects have a guiding effect on the introduction of oxygen functional groups, and the oxygen functional groups of the material after electrochemical reoxidation are close to the vacancy defects. In addition, I explored the electrocatalytic activity and selectivity of the prepared series of materials. The result shows that ERoxoG-O has the highest selectivity for the production of H₂O₂. The regioselectivity of oxygen functional groups affects the performance of the catalyst. This experiment provides ideas for the design of oxygen-functionalized carbon material-based electrocatalysts.

Authors	Y. Wang, F. Grote, Q. Cao, and S. Eigler
Journal	J. Phys. Chem. Lett. 2021, 12, 41, 10009–10014.
DOI	10.1021/acs.jpcclett.1c02957
Detailed scientific contribution	<p>The concept of this manuscript was elaborated by Y. Wang and Prof. Dr. S. Eigler.</p> <p>OxoG and related materials were prepared and characterized with optical microscopy and atomic force microscopy by Y. Wang. Y. Wang did electrochemical measurements, including electrochemical reduction and oxidation of oxoG, catalyst performance testing. OxoG* was synthesised by F. Grote. Y. Wang did the electrochemical test of oxoG* and related materials. Q. Cao did Raman measurement. X-ray photoelectron spectroscopy was measured by R.T. Qie from Technical University of Denmark. Y. Wang analyzed the data of Raman and X-ray photoelectron spectroscopy.</p> <p>Y. Wang wrote the manuscript. The revision of the manuscript was assisted by Prof. Dr. S. Eigler and F. Grote.</p>
Estimated own contribution	~80 %

Pages 54 - 64 have been removed from the online version for copyright reasons.

5.3 Influence of the coffee-ring effect and size of flakes of GO films on the electrochemical reduction.

In the electrochemical reduction of GO, it is necessary to drop GO onto the substrate or electrode surface to form a thin film.¹¹⁹ Some studies have shown that protons play a vital role in the electrochemical reduction of GO. GO film is considered a potential film for the effective separation of water and ions.⁶⁷⁻⁷¹ Considering the permeability of the electrochemically reduced film, the size of the flakes, the loading, and the macroscopic morphology of the formed film are all not negligible effects.

Here, I use a buffer solution with a pH of 7.4 as the electrolyte. By monitoring the reduction process of the film, it is found that the electrochemical reduction potential and reduction rate are related to the size of the flakes, the loading, and the coffee-ring effect. I speculate that the protons required for electrochemical reduction come from the electrolyte if the film is permeable to the electrolyte. And the protons come from the water between the GO layers if the electrolyte cannot penetrate the film.

Authors	Y. Wang and S. Eigler
Journal	Phys. Chem. Chem. Phys. 2022, 24, 8076-8080.
DOI	10.1039/D1CP05015 https://creativecommons.org/licenses/by/3.0/
Detailed scientific contribution	<p>The concept of this manuscript was elaborated by Y. Wang and Prof. Dr. S. Eigler.</p> <p>OxoG and related materials were prepared and characterized with optical microscopy and atomic force microscopy by Y. Wang. Y. Wang did electrochemical measurements. X-ray photoelectron spectroscopy was measured by R.T. Qie and P. Zhu from Technical University of Denmark. Y. Wang analyzed the data of X-ray photoelectron spectroscopy.</p> <p>Y. Wang wrote the manuscript. Prof. Dr. S. Eigler assisted the revision of the manuscript.</p>
Estimated own contribution	~80 %


 Cite this: *Phys. Chem. Chem. Phys.*, 2022, 24, 8076

 Received 3rd November 2021,
Accepted 8th March 2022

DOI: 10.1039/d1cp05015j

rsc.li/pccp

Influence of the coffee-ring effect and size of flakes of graphene oxide films on their electrochemical reduction†

 Yiqing Wang and Siegfried Eigler *

Electrodes for electrochemical reduction of graphene oxide (GO) are coated with thin films using drop-casting and evaporation-assisted self-assembly. The influence of loading, the size of the flakes of GO, and the macroscopic coffee-ring effect occurring during drying are investigated. The effective transfer of protons and electrons in the electrochemical reduction of GO is decisive.

Electrochemically reduced graphene oxide (ERGO) can be generated facilely and be widely used for various electrochemical sensors.¹ ERGO-modified electrodes are primarily prepared as thin-film materials on conducting substrates by drop-casting in basic and applied research.^{2–4} Thus, ERGO has been studied as an electrochemically active material.^{5–11} Moreover, the electrochemical reduction of GO was studied under acidic and basic pH and in organic media. The C/O ratios determined by XPS were identified to be 3.8, 7.8, and 1.8, respectively. The presence of protons in acidic and alkaline media and water as a proton donor make the reduction more efficient. The role of protons (H⁺) plays an essential role in the reduction mechanism of GO.¹² In another study, the essential role of H⁺ in the electrochemical reduction was identified by recording linear sweep voltammograms by lowering the pH values. Thus, the potentials of the reduction peaks shifted negatively with increasing pH values.¹³ ERGO can generally be obtained by cyclic voltammetry and chronoamperometry.¹⁴ Some reports use cyclic voltammetry and identify the reduction of different kinds of oxygen functional groups at different potentials.¹⁵ However, generally speaking, the surfaces of GO and oxo-functionalized graphene (oxoG: derivative of GO with defined structures), respectively, are decorated mainly with hydroxyl groups that formally need one electron and one proton for reduction and epoxy groups that require two electrons and two

protons for reduction, since they must first be opened for transformation into hydroxyl groups.

These reactions may not only be influenced by the applied voltage but also by the GO itself, such as the degree of oxidation, the size of the flakes, the amount of loading, *etc.* Bonanni *et al.* showed that oxidative debris in GO determined the inherent electrochemical activity.⁶ It was reported that the thickness of GO films influenced the performance of electrodes, as defined by the amount of loading. Thus, with increasing GO loading, the reduction rate decreased. A possible reason reported was that functional oxo-groups blocked the electron pathway between the sp² carbon regions, preventing carrier transport, thus leading to a decrease in reduction rate.⁵ It was shown in recent studies that the size of the flakes of GO and the thickness of the films had a significant effect on the permeability of water, ions, and organic molecules,^{16,17} and it was noted that the mechanism of electrochemical reduction was not fully understood and must be further studied.¹⁸

Here we show that the electrochemical potential and thus the reduction rate needed to reduce oxoG are determined by the interaction with the electrolyte, loading of oxoG, coffee-ring effect, and size of the flakes. We use oxoG in this study, instead of common GO, which is a derivative of GO with defined surface chemistry and density of lattice defects, as described in detail in recent studies.^{19,20} Different sizes of flakes were obtained by ultrasonication. The obtained materials were dropped on the surface of a glassy carbon electrode (GCE) for electrochemical reduction. First, we use different sizes of flakes (from 18.2 to about 0.1 μm) with the same loading; then, we change the loading (from 40 to 6 μg) with the same flake size. From the areas of the reduction peaks and X-ray photoelectron spectroscopy (XPS) spectra, we conclude that the size of the flakes and the loading have significant impacts on the electrochemical reduction.

First, oxoG was synthesized according to our previously described procedures, as described in brief in the ESI.† As shown in Fig. 1A and B, the lateral dimension of the initial flakes of oxoG obtained after centrifugation is 18.2 μm (oxoG₀).

Institute of Chemistry and Biochemistry, Freie Universität Berlin, Takustraße 3, 14195 Berlin, Germany. E-mail: siegfried.eigler@fu-berlin.de

† Electronic supplementary information (ESI) available: General methods, and cyclic voltammetry. See DOI: 10.1039/d1cp05015j



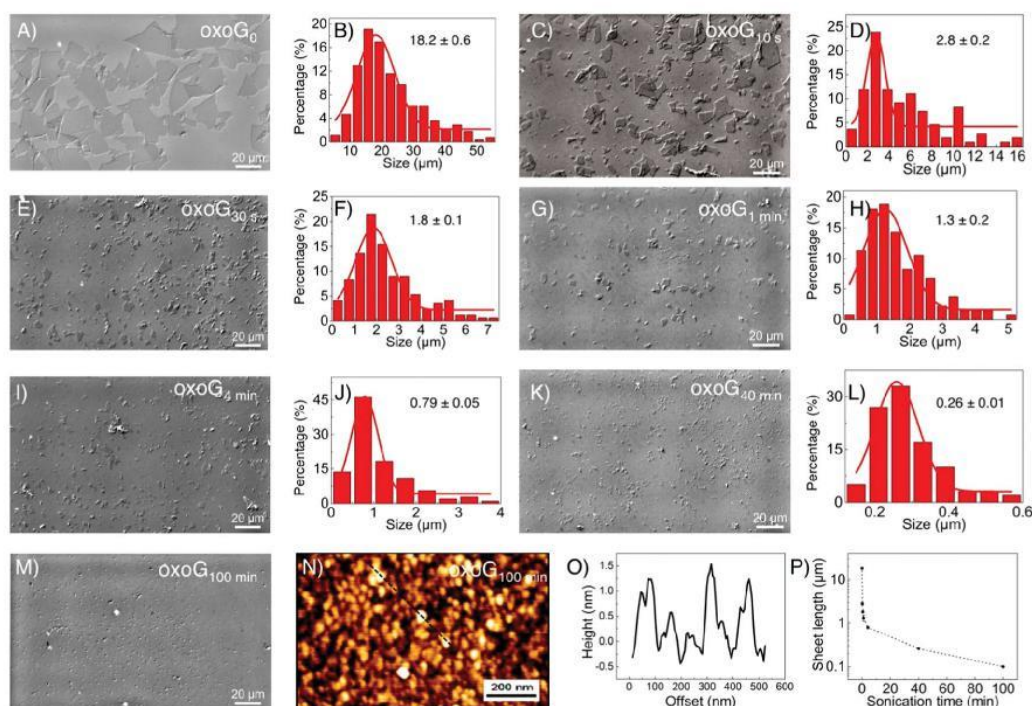


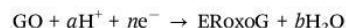
Fig. 1 Optical microscopy images of oxoG on an Si/300 nm SiO₂ wafer and corresponding histograms of the size distributions of oxoG flakes: oxoG₀ (A and B), oxoG_{10 s} (C and D), oxoG_{30 s} (E and F), oxoG_{1 min} (G and H), oxoG_{4 min} (I and J), oxoG_{40 min} (K and L) and oxoG_{100 min} (M). (N) AFM image of oxoG_{100 min} flakes on Si/SiO₂ wafers and (O) corresponding height profile. (P) Sizes of flakes of oxoG for different sonication times.

Different times of sonication were used to produce flakes of oxoG with different sizes of flakes, and the samples are denoted according to the various times of sonication as oxoG_x (index: sonication time, between 10 s and 100 min). Accordingly, electrochemically reduced oxoG with varying times of sonication is termed as ERoxoG_x. In Fig. 1C–L, the optical microscopy images of the oxoG series of flakes and the histograms of the size distributions are presented. Some tiny particles can be observed in the optical microscopy image of oxoG_{100 min}, Fig. 1M. The AFM image in Fig. 1N reveals at least small particles, < 100 nm, including plausibly oxidative debris. The corresponding height profiles are depicted in Fig. 1O. Thus, the sonication process yields flakes with average lateral dimensions of 2.8, 1.8, 1.3, 0.79, 0.26 μm, and less than 0.1 μm, respectively. The different sizes of flakes of oxoG obtained after sonication *versus* time are also shown in Fig. 1P, basically following the rational findings, which we identified before, taking the mechanical force during sonication into account.^{21,22} Only ten seconds of sonication are needed to reduce the mean lateral dimensions of the flakes to 5 μm, and after five minutes of sonication, the sizes of the flakes are below 1 μm. To ensure the reproducibility of the sonication process, we fixed a vial with an aqueous dispersion with a content of 1 mg mL⁻¹ of oxoG₀ in the same position of the sonicator.

For electrochemical reduction, 6 μg of oxoG were deposited on the surface of a GCE. The electrochemical reduction of

oxoG_{100 min} was accomplished under a pH of 7.4 for reference by cyclic voltammetry and the obtained graph is shown in Fig. S1 (ESI[†]). The black line represents the first scan, and the red lines show the remaining 4 scans, indicating the complete reduction after the first cycle. Further cycling of the potential reveals no additional reduction peak, indicating that the removal of oxo-groups of oxoG_{100 min} is complete after the first scan.²³ The cyclic voltammetry (CV) curves of all the samples are depicted in Fig. 2A, and the areas of the reduction peaks are shown in Fig. 2B. We obtained the total charge passed during the reduction process by integration of the areas of the reduction peaks.

The electrochemical reduction process can be expressed as follows:



The moles of transferred electrons are calculated by the equation as follows:^{11,14}

$$n = \frac{Q}{zF}$$

where n is the number of moles of electron transfer, Q is the overall charge, obtained from the reduction peak of Fig. 2A, F is the Faraday constant, and z is the number of exchanged electrons per oxo-group. Therefore, we use the area of the reduction peak to conclude the amount of reduced



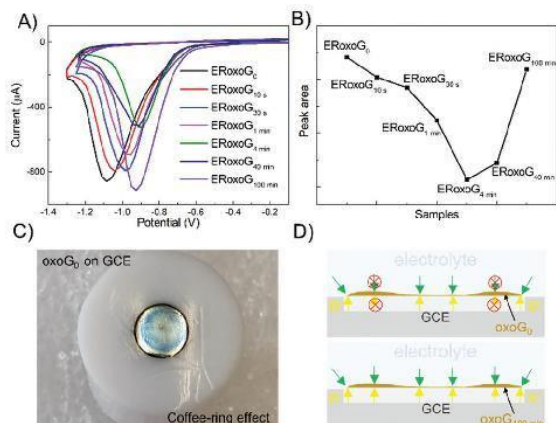


Fig. 2 (A) Cyclic voltammograms obtained from electrochemical reduction of different sizes of oxoG scanned over the full range of 0 V to 1.25 V or 1.3 V. Conditions: supporting electrolyte: an Ar-saturated PB (phosphate buffer) at pH 7.4; scan rate: 100 mV s⁻¹. All starting potentials are relative to the Ag/AgCl reference electrode. (B) Comparison of the reduction peak areas. (C) A noticeable 'coffee ring' appears after oxoG₀ (6 μg) is dried on the GCE. (D) Schematic diagram of the electron and proton transfer during reduction of oxoG₀ (top) and oxoG_{100 min} (bottom).

oxo-groups. It can be seen from Fig. 2A that as the flake size decreases, the reduction peak gradually shifts to less negative potentials (from -1.1 V to -0.9 V), while the area of the reduction peak first decreases and then increases. The gradual shift of the reduction peak to the right means that the reduction rate of small-sized oxoG is increased. However, the reduction peak area of oxoG_{100 min}, which owns the smallest flakes is much larger than that of oxoG_{40 min}, which is almost equivalent to that of oxoG₀. This means that the reducible oxo-groups of the oxoG film increased after sonication with decreasing size of the flakes. It has been reported that ultrasonication can increase the oxidation degree of GO when the GO has a weak oxidation degree.²⁴ However, we found that it is not the sonication process that increases the degree of oxidation of oxoG_{100 min} and it is thus not responsible for the increased reduction peak. We investigated by XPS measurement the effect of functionalization as a result of sonication time for the samples of oxoG₀ and oxoG_{100 min}, which have almost the same reduction peak, and oxoG_{4 min}, which has the smallest reduction peak area.

Fig. 3A illustrates the XPS survey spectra of oxoG₀, oxoG_{4 min}, and oxoG_{100 min}. The C/O ratio of oxoG is 2.1 and changes to 3.1 for oxoG_{4 min} and 3.2 for oxoG_{100 min}. It can be seen that the oxygen content first decreases with sonication. However, as the sonication time is extended, the C/O ratio remains almost the same. High-resolution C 1s XPS spectra of all the samples can be deconvoluted into three peaks (Fig. 3B). The peak at binding energies of 284.8 eV corresponds to C=C sp² bonds. For the rest of the peaks, especially the C-O peak intensity at a binding energy of 286.7 eV decreases obviously with the prolongation of the ultrasonication time, which may be a

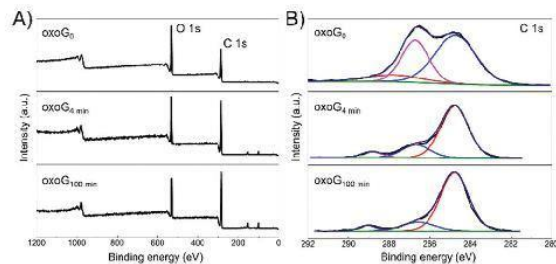


Fig. 3 (A) XPS survey spectra and (B) high-resolution C 1s XPS spectra of oxoG₀, oxoG_{4 min} and oxoG_{100 min} showing the changes of oxygen functional groups after sonication.

consequence of local energy not dissipating using a sonication bath.^{6,23,25} When the size of the flakes and the degree of oxidation is reduced, the corresponding materials (e.g., oxoG_{100 min}) can be further reduced electrochemically. From the reported permeability studies of GO films, we speculate that this is related to the permeability of the oxoG film to water formed by drop casting.^{26,27} GO films produced by evaporation-assisted self-assembly have a random morphology with some ring-shaped patterns (coffee-ring effect) (Fig. 2C) and the films have a very low pervaporation performance.^{3,26,28,29} As shown in Fig. 2D, for the coffee-ring, the ring area is thicker than the edge. However, we hypothesize that for a membrane composed of small flakes (oxoG_{100 min}), the electrolyte permeability is better at the ring than for larger flakes (oxoG₀), and the rate of reduction thus increases.

To confirm the above speculation, we increased the loading of oxoG₀ from 6 μg for recording CVs shown in Fig. 2B to 40 μg, as depicted in Fig. 4A, and 20 μg in Fig. 4D to capture the influence of the film surface during the reduction (insets are taken from Videos S1 and S2, ESI†). In Fig. 4A and C, with 40 μg of oxoG on the surface of the GCE, a thick film is generated (concentration of oxoG solution was around 5 mg mL⁻¹ to reduce the coffee-ring effect). The voltage range is from 0 to 1.5 V, with a scan rate of 50 mV s⁻¹. A progressively larger black ring can be observed from the inset images when the voltage is driven from -1.0 to -1.5 V. Only the edge of the film is directly and simultaneously in contact with the electrolyte and electrode surface at the potential of -1.0 V (bottom of Fig. 4C). It can be observed that the reduction advances slowly from the edge of the film to the center (Fig. 4B). So, we can speculate that the water and H⁺ cannot penetrate the film, and the H⁺ required for the reduction reaction comes from the water adsorbed in the oxoG layer.^{9,30} The curve in Fig. 4D shows the completion of the reduction process at -1.4 V. To facilitate the observation of the whole reduction process, the sweep speed is set to 50 mV s⁻¹. No significant change of the colour of the film's surface is observed before reaching the potential of -0.9 V, as the inset photographs show. In the course of reduction, a black central area and edge area appear at the potential of -1.15 V, indicating that some of the areas had been reduced. When the voltage reaches -1.22 V, the black area on the film's surface expands simultaneously from the center to



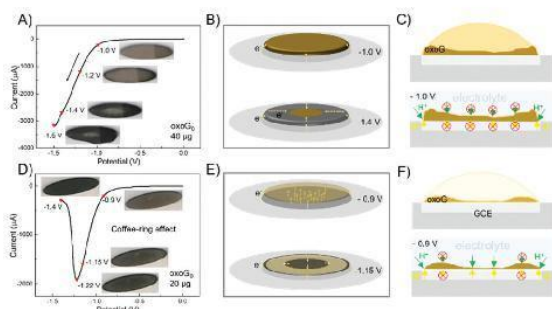


Fig. 4 (A) Cyclic voltammograms obtained from the electrochemical reduction of oxoG₀ scanned over the full range from 0 to -1.5 V. The loading of the GCE is $40 \mu\text{g}$. Scan rate: 50 mV s^{-1} . Insets: Images of the film on the GCE at the potentials of -1.0 , -1.2 , -1.4 , and -1.5 V. (B) Schematics of electron transfer for oxoG₀ reduction at the potentials of -1.0 and -1.4 V (loading: $40 \mu\text{g}$). (C) Top: cross-sectional view of the film formation process on the glassy carbon electrode; bottom: cross-sectional views at -1.0 V in Fig. 4A and B. (D) Cyclic voltammograms obtained by the electrochemical reduction of oxoG₀ scanned over the range from 0 to -1.4 V; the loading of the GCE is $20 \mu\text{g}$. Scan rate: 50 mV s^{-1} . Insets: Images of the film on the GCE at the potentials of -0.9 , -1.15 , -1.22 , and -1.4 V. (E) Schematics of electron transfer for oxoG₀ reduction at the potentials of -0.9 and -1.15 V (loading: $20 \mu\text{g}$). (F) Top: cross-sectional view of the film formation process on the glassy carbon electrode; bottom: cross-sectional views at -0.9 V in (D) and (E). All starting potentials are relative to the Ag/AgCl reference electrode.

the edge and from the edge to the center. This phenomenon is explained in the schematic of Fig. 4E. Fig. 4F shows the cross-sectional view of the film formation process on the glassy carbon electrode and the cross-sectional view at -0.9 V. It is difficult to use the camera to observe the changes in the electrode surface clearly when the loading is $6 \mu\text{g}$. In order to increase the clarity of the video, we use a $20 \mu\text{g}$ loading to detect the coffee-ring effect of Fig. 4D (the concentration of the oxoG solution was 1 mg mL^{-1}). Fig. 4D shows the results with a loading of $20 \mu\text{g}$. The film derived from the coffee-ring effect is not uniform (Fig. 4F, top). The water and H^+ can only penetrate the thinner central area. Therefore, the permeable central area and the edge of the film can be reduced through the electrolyte. Thus, the required H^+ for reduction is delivered from the electrolyte. In contrast, the reduction of other areas requires H^+ from water in the oxoG layer, a highly pH-sensitive process, requiring more negative potentials at the pH of 7.4, as used here. Based on the above findings, we conclude that when the loading is small, the coffee-ring effect is more obvious, and the part of the film near the edge is thicker than that of the center, which makes it impermeable for the H^+ and water, leading to a reduced reduction rate and efficiency of electrochemical reduction.

In Fig. 2A, the reduction efficiency and rate are improved when the flakes are small, especially for oxoG_{100 min}. Thus, the film composed of small-size flakes has a better permeability to electrolytes.

Overall, we investigated the reduction of films of flakes of oxoG on a GCE with lateral dimensions between $18 \mu\text{m}$ and less

than 100 nm . Drop casting a small amount of oxoG solution on a GCE will cause the coffee-ring effect. In this case, the electrochemical reduction is divided into two processes: the electrolyte can directly provide H^+ for the reduction, when the electrolyte can penetrate the film. The process occurs at the central area and edge of the film. When the film is impermeable, the H^+ stems from the water adsorbed on oxoG, at a pH of 7.4. The oxoG film composed of small flakes (oxoG_{100 min}) has good permeability and can weaken the drawback of the coffee-ring effect on the electrochemical reduction. Consequently, the electrochemical reduction of oxoG is affected by both the size of the flakes and the loading. This work provides inspiration for the electrochemical functionalization of two-dimensional (2D) materials and the design of 2D composite materials. It is shown that the reduction of oxoG may occur at very different potentials, although the materials compositions are very similar, however, with varying sizes of flakes. We further conclude that the permeability of the films has a very important effect on the reduction potentials. Thus, if the 2D materials are used as an electrocatalyst or sensing material, the performance will alter with the morphology, as quantified by reducing oxoG in this study. Thus, the results indicate that they appear beneficial for applications, since the composite materials containing GO are permeable to electrolyte molecules to increase electrode performance.

Conflicts of interest

There are no conflicts to declare.

Acknowledgements

This research is supported by the China Scholarship Council (CSC). This research was funded by the Deutsche Forschungsgemeinschaft (DFG, German Research Foundation, project number 392444269). R. T. Qie and P. Zhu from the Technical University of Denmark are acknowledged for conducting XPS measurements.

Notes and references

- 1 A. Ambrosi, C. K. Chua, N. M. Latiff, A. H. Loo, C. H. Wong, A. Y. Eng, A. Bonanni and M. Pumera, *Chem. Soc. Rev.*, 2016, **45**, 2458–2493.
- 2 A. Kaliyaraj Selva Kumar, Y. Zhang, D. Li and R. G. Compton, *Electrochem. Commun.*, 2020, **121**, 106867.
- 3 H. Li, D. Buesen, R. Williams, J. Henig, S. Stapf, K. Mukherjee, E. Freier, W. Lubitz, M. Winkler, T. Happe and N. Plumere, *Chem. Sci.*, 2018, **9**, 7596–7605.
- 4 Y. Wang, F. Yu, M. Zhu, C. Ma, D. Zhao, C. Wang, A. Zhou, B. Dai, J. Ji and X. Guo, *J. Mater. Chem. A*, 2018, **6**, 2011–2017.
- 5 Y. Zhang, H. Hao and L. Wang, *Appl. Surf. Sci.*, 2016, **390**, 385–392.
- 6 A. Bonanni, A. Ambrosi, C. K. Chua and M. Pumera, *ACS Nano*, 2014, **8**, 4197–4204.



- 7 J. Kauppila, P. Kunnas, P. Damlin, A. Viinikanoja and C. Kvarnström, *Electrochim. Acta*, 2013, **89**, 84–89.
- 8 A. Viinikanoja, Z. Wang, J. Kauppila and C. Kvarnstrom, *Phys. Chem. Chem. Phys.*, 2012, **14**, 14003–14009.
- 9 K. W. Silverstein, C. E. Halbig, J. S. Mehta, A. Sharma, S. Eigler and J. M. Matisvetsky, *Nanoscale*, 2019, **11**, 3112–3116.
- 10 X. Feng, W. Chen and L. Yan, *RSC Adv.*, 2016, **6**, 80106–80113.
- 11 A. G. Marrani, R. Zaroni, R. Schrebler and E. A. Dalchiele, *J. Phys. Chem. C*, 2017, **121**, 5675–5683.
- 12 J. A. Quezada-Renteria, C. O. Ania, L. F. Chazaro-Ruiz and J. R. Rangel-Mendez, *Carbon*, 2019, **149**, 722–732.
- 13 M. Zhou, Y. Wang, Y. Zhai, J. Zhai, W. Ren, F. Wang and S. Dong, *Chem. – Eur. J.*, 2009, **15**, 6116–6120.
- 14 A. Y. Eng, A. Ambrosi, C. K. Chua, F. Sanek, Z. Sofer and M. Pumera, *Chem. – Eur. J.*, 2013, **19**, 12673–12683.
- 15 M. Gao, Y. Xu, X. Wang, Y. Sang and S. Wang, *Electroanalysis*, 2016, **28**, 1377–1382.
- 16 K. G. Zhou, K. S. Vasu, C. T. Cherian, M. Neek-Amal, J. C. Zhang, H. Ghorbanfekr-Kalashami, K. Huang, O. P. Marshall, V. G. Kravets, J. Abraham, Y. Su, A. N. Grigorenko, A. Pratt, A. K. Geim, F. M. Peeters, K. S. Novoselov and R. R. Nair, *Nature*, 2018, **559**, 236–240.
- 17 R. Joshi, P. Carbone, F.-C. Wang, V. G. Kravets, Y. Su, I. V. Grigorieva, H. Wu, A. K. Geim and R. R. Nair, *Science*, 2014, **343**, 752–754.
- 18 M. Pumera, *Chem. Soc. Rev.*, 2010, **39**, 4146–4157.
- 19 C. E. Halbig, R. Lasch, J. Krull, A. S. Pirzer, Z. Wang, J. N. Kirchoff, K. I. Bolotin, M. R. Heinrich and S. Eigler, *Angew. Chem., Int. Ed.*, 2019, **58**, 3599–3603.
- 20 Y. Hu, Q. Cao, C. Neumann, T. Lehnert, F. Börmert, Y. Wang, U. Kaiser, A. Turchanin and S. Eigler, *Carbon*, 2021, **185**, 568–577.
- 21 T. J. Nacken, C. E. Halbig, S. E. Wawra, C. Damm, S. Romeis, J. Walter, M. J. Tehrani, Y. Hu, Y. Ishii, S. Eigler and W. Peukert, *Carbon*, 2017, **125**, 360–369.
- 22 C. E. Halbig, T. J. Nacken, J. Walter, C. Damm, S. Eigler and W. Peukert, *Carbon*, 2016, **96**, 897–903.
- 23 Y. Wang, F. Grote, Q. Cao and S. Eigler, *J. Phys. Chem. Lett.*, 2021, **12**, 10009–10014.
- 24 X. Qi, T. Zhou, S. Deng, G. Zong, X. Yao and Q. Fu, *J. Mater. Sci.*, 2013, **49**, 1785–1793.
- 25 Y. Wang, C. Neumann, M. Hufsmann, Q. Cao, Y. Hu, O. Garrity, P. Kusch, A. Turchanin and S. Eigler, *Adv. Mater. Interfaces*, 2021, **8**, 2100783.
- 26 C.-H. Tsou, Q.-F. An, S.-C. Lo, M. De Guzman, W.-S. Hung, C.-C. Hu, K.-R. Lee and J.-Y. Lai, *J. Membr. Sci.*, 2015, **477**, 93–100.
- 27 L. Nie, K. Goh, Y. Wang, J. Lee, Y. Huang, H. E. Karahan, K. Zhou, M. D. Guiver and T.-H. Bae, *Sci. Adv.*, 2020, **6**, eaaz9184.
- 28 D. S. Eom, J. Chang, Y. W. Song, J. A. Lim, J. T. Han, H. Kim and K. Cho, *J. Phys. Chem. C*, 2014, **118**, 27081–27090.
- 29 P. Su, F. Wang, Z. Li, C. Y. Tang and W. Li, *J. Mater. Chem. A*, 2020, **8**, 15319–15340.
- 30 H. Bi, K. Yin, X. Xie, J. Ji, S. Wan, L. Sun, M. Terrones and M. S. Dresselhaus, *Sci. Rep.*, 2013, **3**, 2714.



Supporting Information

Influence of the coffee-ring effect and size of flakes of graphene oxide films on its electrochemical reduction

Yiqing Wang,^a Siegfried Eigler ^{*a}

Institute of Chemistry and Biochemistry, Freie Universität Berlin, Takustraße 3, 14195 Berlin, Germany

Materials and Methods

Graphite (3061) was obtained from Asbury Carbon. A Nikon Eclipse LV150-NL with differential interference contrast was used to visualize materials. Statistical Raman spectroscopy (SRS) was recorded using a Horiba Explora spectrometer with a 532 nm laser for excitation combined with a 100x magnification objective. For the preparation of Langmuir-Blodgett films, we used a Kibron μ Throug system with water as subphase. The surface tension of water = 72.8 mN m⁻¹ was set to zero. The films were formed at a surface tension value of 3 mN m⁻¹. AFM images were recorded on a JPK Nanowizard 4 equipped with NSG10/Au probes, and intermittent contact mode was used with a Tap300-G AFM Probe. We used a USC300T (Supply: 230 V 50Hz 150 VA. Output: HF 45kHz 80W) for sonication. Electrochemical experiments were performed with a Keithley 2460 SourceMeter in phosphate buffered (PB) solution as a supporting electrolyte. The pH is 7.4. The material modified glassy carbon electrode with a diameter of 5mm is used as the working electrode, Ag/AgCl is used as the reference electrode, and platinum wire is used as the counter electrode. The images in this test are taken from video screenshots, using a camera to capture the electrochemical reduction process and control the capture's synchronization with the electrochemical reaction..

Synthesis of Oxo-Functionalized Graphene (oxoG)

OxoG was prepared by low-temperature oxidation of graphite according to our previously developed method.^{1,3} Accordingly, 2 g of graphite (type 3061, Asbury Carbon Mills) were mixed with 50 mL of sulfuric acid (97.5%) in a Teflon reactor under mechanical stirring at a temperature below 10 °C. After that, 4 g of KMnO₄ were slowly added within 4 h and further stirred for 16 h. Then, 40 mL of cold dilute sulfuric acid (20 wt%) and followed by 100 mL of cold double distilled water were slowly continuously added through a programmed pump within 4 h and 16 h, respectively. Then, 40 mL of H₂O₂ (5 wt%) were added into the reaction mixture to solubilize manganese species. Then, the dispersion was washed with cold double distilled water by repeated centrifugation and redispersion in double distilled water six times. The suspension is adjusted to 1 mg/mL.

Formation of films of flakes of oxoG on Si/300 nm SiO₂ wafer.

Flakes of oxoG were deposited on a Si/300 nm SiO₂ wafer by Langmuir Blodgett technique. First, a light yellowish oxoG dispersion was prepared by dilution of water with methanol in equal volume. The dispersion was dropped on the water surface of the Langmuir-Blodgett trough and the barriers were compressed until a surface tension of 3 mN m⁻¹ was reached.

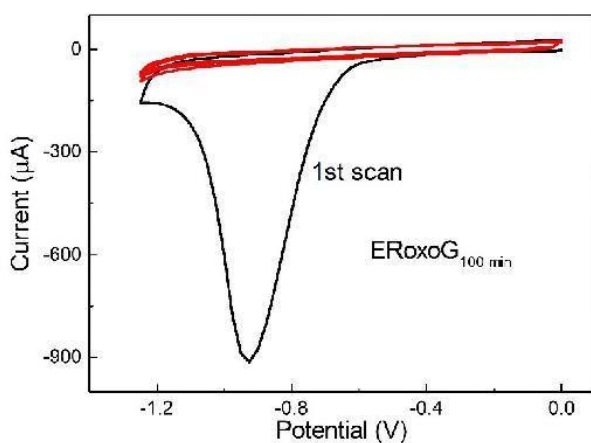


Figure S1. Profiles of cyclic voltammetry were obtained by electrochemical reduction of ERoxoG_{100 min}. The black line is the first scan of electrochemical reduction. The other 4 scans are represented by the red line.

Referents

1. C. E. Halbig, R. Lasch, J. Krull, A. S. Pirzer, Z. Wang, J. N. Kirchhof, K. I. Bolotin, M. R. Heinrich and S. Eigler, *Angew. Chem. Int. Ed.*, 2019, **58**, 3599-3603.
2. S. Eigler, M. Enzelberger-Heim, S. Grimm, P. Hofmann, W. Kroener, A. Geworski, C. Dotzer, M. Rockert, J. Xiao, C. Papp, O. Lytken, H. P. Steinruck, P. Muller and A. Hirsch, *Adv. Mater.*, 2013, **25**, 3583-3587.
3. P. Feicht, J. Biskupek, T. E. Gorelik, J. Renner, C. E. Halbig, M. Maranska, F. Puchtler, U. Kaiser and S. Eigler, *Chem. Eur. J.*, 2019, **25**, 8955-8959.

6. Minor contributions

6.1 Wet-chemical synthesis of solution-processible porous graphene via defect-driven etching.

Authors	Y. Hu, Q. Cao, C. Neumann, T. Lehnert, F. Börrnert, Y. Wang, U. Kaiser, A. Turchanin and S. Eigler
Journal	Carbon, 2021 , 185, 568-577.
DOI	10.1016/j.carbon.2021.09.027
Detailed scientific contribution	Some oxoG was synthesised by Y. Wang. The revision of the manuscript was assisted by Y. Wang.

Pages 74 - 91 have been removed from the online version for copyright reasons.

Reference

1. Geim, A. K.; Novoselov, K. S., The rise of graphene. In *Nanoscience and Technology*, **2010**, 11-19.
2. Novoselov, K. S.; Geim, A. K.; Morozov, S. V.; Jiang, D.; Zhang, Y.; Dubonos, S. V.; Grigorieva, I. V.; Firsov, A. A., Electric Field Effect in Atomically Thin Carbon Films. **2004**, *306* (5696), 666-669.
3. Schafhaeuti, C., Ueber die Verbindungen des Kohlenstoffes mit Silicium, Eisen und anderen Metallen, welche die verschiedenen Gallungen von Roheisen, Stahl und Schmiedeeisen bilden. **1840**, *21* (1), 129-157.
4. Brodie, B. J. A. C. P., Note sur un nouveau procédé pour la purification et la désagrégation du graphite. **1855**, *45*, 351-353.
5. Brodie, B. C., XIII. On the atomic weight of graphite. **1859**, *149*, 249-259.
6. Gottschalk, F., Beiträge zur Kenntniss der Graphitsäure. **1865**, *95* (1), 321-350.
7. Staudenmaier, L. J. B. d. d. c. G., Verfahren zur darstellung der graphitsäure. **1898**, *31* (2), 1481-1487.
8. Charpy, G. J. C. H. S. A. S., Sur la formation de l'oxyde graphitique et la définition du graphite. **1909**, *148* (5), 920-923.
9. Kohlschütter, V.; Haenni, P., Zur Kenntnis des Graphitischen Kohlenstoffes und der Graphitsäure. **1919**, *105* (1), 121-144.
10. Hofmann, U., Über Graphitsäure und die bei ihrer Zersetzung entstehenden Kohlenstoffarten. **1928**, *61* (2), 435-441.
11. Hofmann, U.; Frenzel, A., Quellung von Graphit und die Bildung von Graphitsäure. **1930**, *63* (5), 1248-1262.
12. Hofmann, U.; Frenzel, A.; Csalán, E., Die Konstitution der Graphitsäure und ihre Reaktionen. **1934**, *510* (1), 1-41.
13. Hummers, W. S.; Offeman, R. E., Preparation of Graphitic Oxide. *J. Am. Chem. Soc.* **1958**, *80* (6), 1339-1339.
14. Scholz, W.; Boehm, H. J. Z. a. a. C., Betrachtungen zur struktur des graphitoxids. **1969**, *369* (3-6), 327-40.
15. Mermoux, M.; Chabre, Y., Formation of graphite oxide. *Synth. Met.* **1989**, *34* (1), 157-162.
16. Mermoux, M.; Chabre, Y.; Rousseau, A., FTIR and ¹³C NMR study of graphite oxide. *Carbon* **1991**, *29* (3), 469-474.
17. Lef, A.; He, H.; Forster, M.; Klinowski, J., Structure of Graphite Oxide Revisited. *J. Phys. Chem. B* **1998**, *102* (23), 4477-4482.
18. Erickson, K.; Erni, R.; Lee, Z.; Alem, N.; Gannett, W.; Zettl, A., Determination of the local chemical structure of graphene oxide and reduced graphene oxide. *Adv. Mater.* **2010**, *22* (40), 4467-72.
19. Stobinski, L.; Lesiak, B.; Malolepszy, A.; Mazurkiewicz, M.; Mierzwa, B.; Zemek, J.; Jiricek, P.; Bieloshapka, I., Graphene oxide and reduced graphene oxide studied by the XRD, TEM and electron spectroscopy methods. *J. Electron Spectrosc* **2014**, *195*, 145-154.
20. Hummers, W. J. U., Preparation of graphitic acid. **1957**. (US2798878)
21. Marcano, D. C.; Kosynkin, D. V.; Berlin, J. M.; Sinitskii, A.; Sun, Z.; Slesarev, A.; Alemany, L. B.; Lu, W.; Tour, J. M., Improved Synthesis of Graphene Oxide. *ACS Nano* **2010**, *4* (8), 4806-4814.
22. Eigler, S.; Dotzer, C.; Hirsch, A., Visualization of defect densities in reduced graphene oxide. *Carbon* **2012**, *50* (10), 3666-3673.
23. Eigler, S.; Enzelberger-Heim, M.; Grimm, S.; Hofmann, P.; Kroener, W.; Geworski, A.; Dotzer, C.; Rockert, M.; Xiao, J.; Papp, C.; Lytken, O.; Steinruck, H. P.; Muller, P.; Hirsch, A., Wet chemical synthesis of graphene. *Adv. Mater.* **2013**, *25* (26), 3583-7.

24. Eigler, S.; Hirsch, A., Chemistry with Graphene and Graphene Oxide—Challenges for Synthetic Chemists. *Angew. Chem. Int. Ed.* **2014**, *53* (30), 7720-7738.
25. Halbig, C. E.; Lasch, R.; Krull, J.; Pirzer, A. S.; Wang, Z.; Kirchhof, J. N.; Bolotin, K. I.; Heinrich, M. R.; Eigler, S., Selective Functionalization of Graphene at Defect-Activated Sites by Arylazocarboxylic tert-Butyl Esters. *Angew. Chem. Int. Ed.* **2019**, *58* (11), 3599-3603.
26. Wang, Z.; Yao, Q.; Neumann, C.; Borrnert, F.; Renner, J.; Kaiser, U.; Turchanin, A.; Zandvliet, H. J. W.; Eigler, S., Identification of Semiconductive Patches in Thermally Processed Monolayer Oxo-Functionalized Graphene. *Angew. Chem. Int. Ed.* **2020**, 13657-13662.
27. Grote, F.; Gruber, C.; Börrnert, F.; Kaiser, U.; Eigler, S., Thermal Disproportionation of Oxo-Functionalized Graphene. *Angew. Chem. Int. Ed.* **2017**, *56* (31), 9222-9225.
28. Feicht, P.; Biskupek, J.; Gorelik, T. E.; Renner, J.; Halbig, C. E.; Maranska, M.; Puchtler, F.; Kaiser, U.; Eigler, S., Brodie's or Hummers' Method: Oxidation Conditions Determine the Structure of Graphene Oxide. *Chem. Eur. J.* **2019**, *25* (38), 8955-8959.
29. Brisebois, P. P.; Siaj, M., Harvesting graphene oxide – years 1859 to 2019: a review of its structure, synthesis, properties and exfoliation. *J. Mater. Chem. C* **2020**, *8* (5), 1517-1547.
30. Nishina, Y.; Eigler, S., Chemical and electrochemical synthesis of graphene oxide - a generalized view. *Nanoscale* **2020**, *12* (24), 12731-12740.
31. Cai, W.; Piner, R. D.; Stadermann, F. J.; Park, S.; Shaibat, M. A.; Ishii, Y.; Yang, D.; Velamakanni, A.; An, S. J.; Stoller, M.; An, J.; Chen, D.; Ruoff, R. S., Synthesis and Solid-State NMR Structural Characterization of ¹³C-Labeled Graphite Oxide. *Science* **2008**, *321* (5897), 1815-1817.
32. Szabó, T.; Berkesi, O.; Forgó, P.; Josepovits, K.; Sanakis, Y.; Petridis, D.; Dékány, I., Evolution of Surface Functional Groups in a Series of Progressively Oxidized Graphite Oxides. *Chem. Mater.* **2006**, *18* (11), 2740-2749.
33. Szabó, T.; Berkesi, O.; Dékány, I., DRIFT study of deuterium-exchanged graphite oxide. *Carbon* **2005**, *43* (15), 3186-3189.
34. Gao, W.; Alemany, L. B.; Ci, L.; Ajayan, P. M., New insights into the structure and reduction of graphite oxide. *Nat. Chem.* **2009**, *1* (5), 403-408.
35. Dimiev, A.; Kosynkin, D. V.; Alemany, L. B.; Chaguine, P.; Tour, J. M., Pristine graphite oxide. *J. Am. Chem. Soc.* **2012**, *134* (5), 2815-22.
36. Eigler, S.; Dotzer, C.; Hof, F.; Bauer, W.; Hirsch, A., Sulfur Species in Graphene Oxide. *Chem. Eur. J.* **2013**, *19* (29), 9490-9496.
37. Ruess, G.; Vogt, F., Höchstlamellarer Kohlenstoff aus Graphitoxhydroxyd. *Monatshefte für Chemie und verwandte Teile anderer Wissenschaften* **1948**, *78* (3), 222-242.
38. Brisebois, P. P.; Kuss, C.; Schougaard, S. B.; Izquierdo, R.; Siaj, M., New Insights into the Diels-Alder Reaction of Graphene Oxide. *Chem. Eur. J.* **2016**, *22* (17), 5849-52.
39. Collins, W. R.; Lewandowski, W.; Schmois, E.; Walsh, J.; Swager, T. M., Claisen Rearrangement of Graphite Oxide: A Route to Covalently Functionalized Graphenes. *Angew. Chem. Int. Ed.* **2011**, *2011*, *50* (38), 8848-8852.
40. Park, S.; Ruoff, R. S., Chemical methods for the production of graphenes. *Nat. Nanotechnol.* **2009**, *4* (4), 217-24.
41. Chen, D.; Feng, H.; Li, J., Graphene Oxide: Preparation, Functionalization, and Electrochemical Applications. *Chem. Rev.* **2012**, *112* (11), 6027-6053.
42. Dreyer, D. R.; Todd, A. D.; Bielawski, C. W., Harnessing the chemistry of graphene oxide. *Chem. Soc. Rev.* **2014**, *43* (15), 5288-301.
43. Yang, L.; Zhang, R.; Liu, B.; Wang, J.; Wang, S.; Han, M. Y.; Zhang, Z., pi-conjugated carbon radicals at graphene oxide to initiate ultrastrong chemiluminescence. *Angew. Chem. Int. Ed.* **2014**, *53* (38), 10109-13.

44. Eigler, S.; Grimm, S.; Hirsch, A., Investigation of the thermal stability of the carbon framework of graphene oxide. **2018**, arXiv preprint arXiv:1805.02654.
45. Pieper, H.; Chercheja, S.; Eigler, S.; Halbig, C. E.; Filipovic, M. R.; Mokhir, A., Endoperoxides Revealed as Origin of the Toxicity of Graphene Oxide. *Angew. Chem. Int. Ed.* **2016**, *55* (1), 405-407.
46. Dimiev, A. M.; Alemany, L. B.; Tour, J. M., Graphene Oxide. Origin of Acidity, Its Instability in Water, and a New Dynamic Structural Model. *ACS Nano* **2013**, *7* (1), 576-588.
47. Halbig, C. E.; Nacken, T. J.; Walter, J.; Damm, C.; Eigler, S.; Peukert, W., Quantitative investigation of the fragmentation process and defect density evolution of oxo-functionalized graphene due to ultrasonication and milling. *Carbon* **2016**, *96*, 897-903.
48. Cancado, L. G.; Jorio, A.; Ferreira, E. H.; Stavale, F.; Achete, C. A.; Capaz, R. B.; Moutinho, M. V.; Lombardo, A.; Kulmala, T. S.; Ferrari, A. C., Quantifying defects in graphene via Raman spectroscopy at different excitation energies. *Nano Lett.* **2011**, *11* (8), 3190-6.
49. Ferrari, A. C.; Basko, D. M., Raman spectroscopy as a versatile tool for studying the properties of graphene. *Nat. Nanotechnol.* **2013**, *8* (4), 235-46.
50. Vecera, P.; Eigler, S.; Kolesnik-Gray, M.; Krstic, V.; Vierck, A.; Maultzsch, J.; Schafer, R. A.; Hauke, F.; Hirsch, A., Degree of functionalisation dependence of individual Raman intensities in covalent graphene derivatives. *Sci. Rep.* **2017**, *7*, 45165.
51. Lucchese, M. M.; Stavale, F.; Ferreira, E. H. M.; Vilani, C.; Moutinho, M. V. O.; Capaz, R. B.; Achete, C. A.; Jorio, A., Quantifying ion-induced defects and Raman relaxation length in graphene. *Carbon* **2010**, *48* (5), 1592-1597.
52. Zhou, M.; Wang, Y.; Zhai, Y.; Zhai, J.; Ren, W.; Wang, F.; Dong, S., Controlled synthesis of large-area and patterned electrochemically reduced graphene oxide films. *Chem. Eur. J.* **2009**, *15* (25), 6116-20.
53. Ambrosi, A.; Chua, C. K.; Latiff, N. M.; Loo, A. H.; Wong, C. H.; Eng, A. Y.; Bonanni, A.; Pumera, M., Graphene and its electrochemistry - an update. *Chem. Soc. Rev.* **2016**, *45* (9), 2458-93.
54. Eng, A. Y.; Ambrosi, A.; Chua, C. K.; Sanek, F.; Sofer, Z.; Pumera, M., Unusual inherent electrochemistry of graphene oxides prepared using permanganate oxidants. *Chem. Eur. J.* **2013**, *19* (38), 12673-83.
55. Bonanni, A.; Ambrosi, A.; Chua, C. K.; Pumera, M., Oxidation Debris in Graphene Oxide Is Responsible for Its Inherent Electroactivity. *ACS Nano* **2014**, *8* (5), 4197-4204.
56. Feng, X.; Chen, W.; Yan, L., Electrochemical reduction of bulk graphene oxide materials. *RSC Adv.* **2016**, *6* (83), 80106-80113.
57. Viinikanoja, A.; Wang, Z.; Kauppila, J.; Kvarnstrom, C., Electrochemical reduction of graphene oxide and its in situ spectroelectrochemical characterization. *Phys. Chem. Chem. Phys.* **2012**, *14* (40), 14003-9.
58. Kauppila, J.; Kunnas, P.; Damlin, P.; Viinikanoja, A.; Kvarnström, C., Electrochemical reduction of graphene oxide films in aqueous and organic solutions. *Electrochim. Acta* **2013**, *89*, 84-89.
59. Gao, M.; Xu, Y.; Wang, X.; Sang, Y.; Wang, S., Analysis of Electrochemical Reduction Process of Graphene Oxide and its Electrochemical Behavior. *Electroanalysis* **2016**, *28* (6), 1377-1382.
60. Chng, E. L.; Pumera, M., Solid-state electrochemistry of graphene oxides: absolute quantification of reducible groups using voltammetry. *Chem Asian J* **2011**, *6* (11), 2899-901.
61. Quezada-Renteria, J. A.; Ania, C. O.; Chazaro-Ruiz, L. F.; Rangel-Mendez, J. R., Influence of protons on reduction degree and defect formation in electrochemically reduced graphene oxide. *Carbon* **2019**, *149*, 722-732.

62. Li, B.; Pan, G.; Avent, N. D.; Lowry, R. B.; Madgett, T. E.; Waines, P. L., Graphene electrode modified with electrochemically reduced graphene oxide for label-free DNA detection. *Biosens. Bioelectron.* **2015**, *72*, 313-9.
63. Zhang, Y.; Hao, H.; Wang, L., Effect of morphology and defect density on electron transfer of electrochemically reduced graphene oxide. *Appl. Surf. Sci.* **2016**, *390*, 385-392.
64. Wang, Q.; Zhang, J.; Xu, Y.; Wang, Y.; Wu, L.; Weng, X.; You, C.; Feng, J., A one-step electrochemically reduced graphene oxide based sensor for sensitive voltammetric determination of furfural in milk products. *Anal. Methods* **2020**.
65. Haque, A. M.; Park, H.; Sung, D.; Jon, S.; Choi, S. Y.; Kim, K., An electrochemically reduced graphene oxide-based electrochemical immunosensing platform for ultrasensitive antigen detection. *Anal. Chem.* **2012**, *84* (4), 1871-8.
66. Marrani, A. G.; Zanoni, R.; Schrebler, R.; Dalchiele, E. A., Toward Graphene/Silicon Interface via Controlled Electrochemical Reduction of Graphene Oxide. *J. Phys. Chem. C* **2017**, *121* (10), 5675-5683.
67. Zhou, K. G.; Vasu, K. S.; Cherian, C. T.; Neek-Amal, M.; Zhang, J. C.; Ghorbanfekr-Kalashami, H.; Huang, K.; Marshall, O. P.; Kravets, V. G.; Abraham, J.; Su, Y.; Grigorenko, A. N.; Pratt, A.; Geim, A. K.; Peeters, F. M.; Novoselov, K. S.; Nair, R. R., Electrically controlled water permeation through graphene oxide membranes. *Nature* **2018**, *559* (7713), 236-240.
68. Tsou, C.-H.; An, Q.-F.; Lo, S.-C.; De Guzman, M.; Hung, W.-S.; Hu, C.-C.; Lee, K.-R.; Lai, J.-Y., Effect of microstructure of graphene oxide fabricated through different self-assembly techniques on 1-butanol dehydration. *J. Membr. Sci.* **2015**, *477*, 93-100.
69. Su, P.; Wang, F.; Li, Z.; Tang, C. Y.; Li, W., Graphene oxide membranes: controlling their transport pathways. *J. Mater. Chem. A* **2020**, *8* (31), 15319-15340.
70. Joshi, R.; Carbone, P.; Wang, F.-C.; Kravets, V. G.; Su, Y.; Grigorieva, I. V.; Wu, H.; Geim, A. K.; Nair, R. R. J. s., Precise and ultrafast molecular sieving through graphene oxide membranes. *Science* **2014**, *343* (6172), 752-754.
71. Zhao, J.; Pei, S.; Ren, W.; Gao, L.; Cheng, H.-M., Efficient Preparation of Large-Area Graphene Oxide Sheets for Transparent Conductive Films. *ACS Nano* **2010**, *4* (9), 5245-5252.
72. Pumera, M., Graphene-based nanomaterials and their electrochemistry. *Chem. Soc. Rev.* **2010**, *39* (11), 4146-57.
73. Pumera, M., Electrochemistry of graphene: new horizons for sensing and energy storage. *Chem Rec* **2009**, *9* (4), 211-23.
74. Wang, Y.; Yu, F.; Zhu, M.; Ma, C.; Zhao, D.; Wang, C.; Zhou, A.; Dai, B.; Ji, J.; Guo, X., N-Doping of plasma exfoliated graphene oxide via dielectric barrier discharge plasma treatment for the oxygen reduction reaction. *J. Mater. Chem. A* **2018**, *6* (5), 2011-2017.
75. Hsu, S.-Y.; Lee, C.-L.; Kuo, C.-H.; Kuo, W.-C., Defective graphene nanosheets with heteroatom doping as hydrogen peroxide reduction catalysts and sensors. *Sens. Actuators B Chem.* **2021**, *328*, 129015.
76. Komeily-Nia, Z.; Qu, L.-T.; Li, J.-L., Progress in the Understanding and Applications of the Intrinsic Reactivity of Graphene-Based Materials. *Small Science* **2020**, *1* (2), 2000026.
77. Kim, H. W.; Ross, M. B.; Kornienko, N.; Zhang, L.; Guo, J.; Yang, P.; McCloskey, B. D., Efficient hydrogen peroxide generation using reduced graphene oxide-based oxygen reduction electrocatalysts. *Nat. Catal.* **2018**, *1* (4), 282-290.
78. Down, M. P.; Rowley-Neale, S. J.; Smith, G. C.; Banks, C. E., Fabrication of Graphene Oxide Supercapacitor Devices. *ACS Appl. Energy Mater.* **2018**, *1* (2), 707-714.
79. Han, L.; Sun, Y.; Li, S.; Cheng, C.; Halbig, C. E.; Feicht, P.; Hübner, J. L.; Strasser, P.; Eigler, S., In-Plane Carbon Lattice-Defect Regulating Electrochemical Oxygen

- Reduction to Hydrogen Peroxide Production over Nitrogen-Doped Graphene. *ACS Catal.* **2019**, *9* (2), 1283-1288.
80. Mak, K. F.; Lee, C.; Hone, J.; Shan, J.; Heinz, T. F., Atomically Thin MoS₂: A New Direct-Gap Semiconductor. *Phys. Rev. Lett.* **2010**, *105* (13), 136805.
 81. Chhowalla, M.; Shin, H. S.; Eda, G.; Li, L.-J.; Loh, K. P.; Zhang, H., The chemistry of two-dimensional layered transition metal dichalcogenide nanosheets. *Nat. Chem.* **2013**, *5* (4), 263-275.
 82. Splendiani, A.; Sun, L.; Zhang, Y.; Li, T.; Kim, J.; Chim, C.-Y.; Galli, G.; Wang, F., Emerging Photoluminescence in Monolayer MoS₂. *Nano Lett.* **2010**, *10* (4), 1271-1275.
 83. Lin, Y.; Ling, X.; Yu, L.; Huang, S.; Hsu, A. L.; Lee, Y.-H.; Kong, J.; Dresselhaus, M. S.; Palacios, T., Dielectric Screening of Excitons and Trions in Single-Layer MoS₂. *Nano Lett.* **2014**, *14* (10), 5569-5576.
 84. Pei, J.; Yang, J.; Xu, R.; Zeng, Y.-H.; Myint, Y. W.; Zhang, S.; Zheng, J.-C.; Qin, Q.; Wang, X.; Jiang, W.; Lu, Y., Exciton and Trion Dynamics in Bilayer MoS₂. *Small* **2015**, *11* (48), 6384-6390.
 85. Zhang, X.; Wang, S.; Lee, C.-K.; Cheng, C.-M.; Lan, J.-C.; Li, X.; Qiao, J.; Tao, X., Unravelling the effect of sulfur vacancies on the electronic structure of the MoS₂ crystal. *Phys. Chem. Chem. Phys.* **2020**, *22* (38), 21776-21783.
 86. Qiu, H.; Xu, T.; Wang, Z.; Ren, W.; Nan, H.; Ni, Z.; Chen, Q.; Yuan, S.; Miao, F.; Song, F.; Long, G.; Shi, Y.; Sun, L.; Wang, J.; Wang, X., Hopping transport through defect-induced localized states in molybdenum disulphide. *Nat. Commun.* **2013**, *4* (1), 2642.
 87. Mouri, S.; Miyauchi, Y.; Matsuda, K., Tunable Photoluminescence of Monolayer MoS₂ via Chemical Doping. *Nano Lett.* **2013**, *13* (12), 5944-5948.
 88. Buscema, M.; Steele, G. A.; van der Zant, H. S. J.; Castellanos-Gomez, A., The effect of the substrate on the Raman and photoluminescence emission of single-layer MoS₂. *Nano Res.* **2015**, *7* (4), 561-571.
 89. Zhao, M.; Song, P.; Teng, J., Electrically and Optically Tunable Responses in Graphene/Transition-Metal-Dichalcogenide Heterostructures. *ACS Appl. Mater. Interfaces* **2018**, *10* (50), 44102-44108.
 90. Wang, Z.; Cao, Q.; Sotthewes, K.; Hu, Y.; Shin, H. S.; Eigler, S., Interlayer electron modulation in van der Waals heterostructures assembled by stacking monolayer MoS₂ onto monolayer graphene with different electron transfer ability. *Nanoscale* **2021**, *13* (36), 15464-15470.
 91. Cote, L. J.; Kim, F.; Huang, J., Langmuir–Blodgett Assembly of Graphite Oxide Single Layers. *J. Am. Chem. Soc.* **2009**, *131* (3), 1043-1049.
 92. Sun, F.; Castner, D. G.; Mao, G.; Wang, W.; McKeown, P.; Grainger, D. W., Spontaneous Polymer Thin Film Assembly and Organization Using Mutually Immiscible Side Chains. *J. Am. Chem. Soc.* **1996**, *118* (8), 1856-1866.
 93. Whang, D.; Jin, S.; Wu, Y.; Lieber, C. M., Large-Scale Hierarchical Organization of Nanowire Arrays for Integrated Nanosystems. *Nano Lett.* **2003**, *3* (9), 1255-1259.
 94. Dimiev, A. M.; Eigler, S., Graphene oxide: fundamentals and applications. John Wiley & Sons, 2016.
 95. Beams, R.; Gustavo Cancado, L.; Novotny, L., Raman characterization of defects and dopants in graphene. *J. Phys. Condens. Matter* **2015**, *27* (8), 083002.
 96. Malard, L. M.; Pimenta, M. A.; Dresselhaus, G.; Dresselhaus, M. S., Raman spectroscopy in graphene. *Phys. Rep.* **2009**, *473* (5), 51-87.
 97. Eigler, S.; Hof, F.; Enzelberger-Heim, M.; Grimm, S.; Müller, P.; Hirsch, A., Statistical Raman Microscopy and Atomic Force Microscopy on Heterogeneous Graphene Obtained after Reduction of Graphene Oxide. *J. Phys. Chem. C* **2014**, *118* (14), 7698-7704.
 98. Guo, H.-W.; Hu, Z.; Liu, Z.-B.; Tian, J.-G., Stacking of 2D Materials. *Adv. Funct. Mater.* **2021**, *31* (4), 2007810.

99. Castellanos-Gomez, A.; Buscema, M.; Molenaar, R.; Singh, V.; Janssen, L.; van der Zant, H. S. J.; Steele, G. A., Deterministic transfer of two-dimensional materials by all-dry viscoelastic stamping. *2D Mater.* **2014**, *1* (1), 011002.
100. Gao, Y.; Liu, Z.; Sun, D.-M.; Huang, L.; Ma, L.-P.; Yin, L.-C.; Ma, T.; Zhang, Z.; Ma, X.-L.; Peng, L.-M.; Cheng, H.-M.; Ren, W., Large-area synthesis of high-quality and uniform monolayer WS₂ on reusable Au foils. *Nat. Commun.* **2015**, *6* (1), 8569.
101. Gurarslan, A.; Yu, Y.; Su, L.; Yu, Y.; Suarez, F.; Yao, S.; Zhu, Y.; Ozturk, M.; Zhang, Y.; Cao, L., Surface-Energy-Assisted Perfect Transfer of Centimeter-Scale Monolayer and Few-Layer MoS₂ Films onto Arbitrary Substrates. *ACS Nano* **2014**, *8* (11), 11522-11528.
102. Rusling, J. F.; Suib, S. L., Characterizing Materials with Cyclic Voltammetry. *Adv. Mater.* **1994**, *6* (12), 922-930.
103. Murray, R.; Bard, i. A. J. b. A. B., Marcel Dekker, New York, Electroanalytical chemistry. **1984**, *13*, 191.
104. Sun, Y.; Han, L.; Strasser, P., A comparative perspective of electrochemical and photochemical approaches for catalytic H₂O₂ production. *Chem. Soc. Rev.* **2020**, *49* (18), 6605-6631.
105. Wang, Z.; James, D. K.; Tour, J. M., Metal-Free Electrocatalysts for Oxygen Reduction to Hydrogen Peroxide. *Advanced Energy and Sustainability Research* **2021**, *2* (7), 2100021.
106. Noffke, B. W.; Li, Q.; Raghavachari, K.; Li, L.-s., A Model for the pH-Dependent Selectivity of the Oxygen Reduction Reaction Electrocatalyzed by N-Doped Graphitic Carbon. *J. Am. Chem. Soc.* **2016**, *138* (42), 13923-13929.
107. Criado, A.; Melchionna, M.; Marchesan, S.; Prato, M., The Covalent Functionalization of Graphene on Substrates. *Angew. Chem. Int. Ed.* **2015**, *54* (37), 10734-10750.
108. Xie, J.; Chen, Q.; Shen, H.; Li, G., Review—Wearable Graphene Devices for Sensing. *J. Electrochem. Soc.* **2020**, *167* (3), 037541.
109. Guirguis, A.; Maina, J. W.; Kong, L.; Henderson, L. C.; Rana, A.; Li, L. H.; Majumder, M.; Dumée, L. F., Perforation routes towards practical nano-porous graphene and analogous materials engineering. *Carbon* **2019**, *155*, 660-673.
110. Guirguis, A.; Maina, J. W.; Zhang, X.; Henderson, L. C.; Kong, L.; Shon, H.; Dumée, L. F., Applications of nano-porous graphene materials – critical review on performance and challenges. *Mater. Horizons* **2020**, *7* (5), 1218-1245.
111. Kato, N. I., Reducing focused ion beam damage to transmission electron microscopy samples. *J. Electron Microsc.* **2004**, *53* (5), 451-458.
112. Wang, X.; Jiao, L.; Sheng, K.; Li, C.; Dai, L.; Shi, G., Solution-processable graphene nanomeshes with controlled pore structures. *Sci. Rep.* **2013**, *3* (1), 1996.
113. Dimiev, A. M.; Polson, T. A., Contesting the two-component structural model of graphene oxide and reexamining the chemistry of graphene oxide in basic media. *Carbon* **2015**, *93*, 544-554.
114. Pei, S.; Cheng, H.-M., The reduction of graphene oxide. *Carbon* **2012**, *50* (9), 3210-3228.
115. Zhu, Y.; Murali, S.; Cai, W.; Li, X.; Suk, J. W.; Potts, J. R.; Ruoff, R. S., Graphene and Graphene Oxide: Synthesis, Properties, and Applications. *Adv. Mater.* **2010**, *22* (35), 3906-3924.
116. Baghayeri, M.; Alinezhad, H.; Tarahomi, M.; Fayazi, M.; Ghanei-Motlagh, M.; Maleki, B., A non-enzymatic hydrogen peroxide sensor based on dendrimer functionalized magnetic graphene oxide decorated with palladium nanoparticles. *Appl. Surf. Sci.* **2019**, *478*, 87-93.
117. Sa, Y. J.; Kim, J. H.; Joo, S. H., Active Edge-Site-Rich Carbon Nanocatalysts with Enhanced Electron Transfer for Efficient Electrochemical Hydrogen Peroxide Production. *Angew. Chem. Int. Ed.* **2019**, *58* (4), 1100-1105.

118. Komeily-Nia, Z.; Qu, L.-T.; Li, J.-L., Progress in the Understanding and Applications of the Intrinsic Reactivity of Graphene-Based Materials. *Small Science* **2021**, *1* (2), 2000026.
119. Kaliyaraj Selva Kumar, A.; Zhang, Y.; Li, D.; Compton, R. G., A mini-review: How reliable is the drop casting technique? *Electrochem Commun* **2020**, *121*, 106867.

List of publications

1) Y. Wang, C. Neumann, M. Hußmann, Q. Cao, Y. Hu, O. Garrity, P. Kusch, A. Turchanin and S. Eigler

Synthesis of wet-chemically prepared porous-graphene single layers on Si/SiO₂ substrate increasing the photoluminescence of MoS₂ in heterostructures.

Adv. Mater. Int., **2021**, *8*, 2100783.

2) Y. Wang, F. Grote, Q. Cao and S. Eigler

Regiochemically oxo-functionalized graphene, guided by defect sites, as catalyst for oxygen reduction to hydrogen peroxide.

J. Phys. Chem. Lett. **2021**, *12*, 10009–10014.

3) Y. Wang, S. Eigler*

Influence of the coffee-ring effect and size of flakes of GO films on the electrochemical reduction. Submitted

4) Y. Hu, Q. Cao, C. Neumann, T. Lehnert, F. Börrnert, **Y. Wang**, U. Kaiser, A. Turchanin and S. Eigler*

Wet-chemical synthesis of solution-processible porous graphene via defect-driven etching.

Carbon, **2021**, *185*, 568-577.

List of Abbreviations

2D	Two-dimensional
ϕ	Work function
<i>A</i>	Electrode area
A^0	Neutral excitons
Ag	Silver
AFM	Atomic force microscopy
CV	Cyclic Voltammetry
CE	Counter electrode
C_0	Concentration of oxide
<i>D</i>	Diffusion coefficient
DSM	Dynamic structure model
DR	Double resonance
D_{ct}	Charge transport diffusion coefficient
<i>D</i>	Film thickness
E_{binding}	Binding energy
E_{photon}	X-ray photons' energy
E_{kinetic}	Kinetic energy
eV	Electron volt
F	Faraday constant
H ₂ O ₂	Hydrogen peroxide
HRTEM	High-resolution transmission electron microscopy
<i>I</i>	Intensity
I_D/I_G	Intensity ratio of D peak and G peak
I_R	Ring current
I_D	Disk current

i_p	Peak current
GO	Graphene oxide
GIC	Graphite intercalation compounds
GCE	Glassy carbon electrode
KCl	Potassium chloride
LO	Longitudinal optical
LB	Langmuir-Blodgett
L_D	Distance of defects
MoS ₂	Molybdenum disulfide
N	Collection efficiency (0.37)
NMR	Nuclear magnetic resonance
nm	Nanometre
n	Number of electron transfer
μm	Micrometre
oxoG	Graphene oxide with defined surface structure
OD	Oxidative debris
PDMS	Polydimethylsiloxane
PBS	Phosphate buffered saline
PL	Photoluminescence
Q	Passed charge
Γ	Full-width at half-maximum

R	Gas constant
RE	Reference electrode
RRDE	Rotating ring-disk electrode
r-oxo-G	Reduced oxoG
r_A	Length of active region
r_S	Length of structural disorder region
s	Second
Si/SiO ₂	Silicon/silicon dioxide
T	Temperature
TO	Transverse optical
V	Volt
v	Scan rate
WE	Working electrode
XRD	X-ray diffraction
XPS	X-ray photoelectrode spectroscopy